5-8-2015

Thin Film Based Biocompatible Sensors for Physiological Monitoring

Yihao Zhu
University of South Carolina - Columbia

Recommended Citation
Zhu, Y.(2015). *Thin Film Based Biocompatible Sensors for Physiological Monitoring.* (Doctoral dissertation). Retrieved from http://scholarcommons.sc.edu/etd/3072

THIN FILM BASED BIOCOMPATIBLE SENSORS FOR PHYSIOLOGICAL MONITORING

by

Yihao Zhu

Bachelor of Science
Shanghai Jiao Tong University, 2008

Master of Science
University of California, Irvine, 2010

Submitted in Partial Fulfillment of the Requirements

For the Degree of Doctor of Philosophy in

Electrical Engineering

College of Engineering and Computing

University of South Carolina

2015

Accepted by:

Goutam Koley, Major Professor

Kenneth B. Walsh, Committee Member

MVS Chandrashekhar, Committee Member

Guoan Wang, Committee Member

Lacy Ford, Vice Provost and Dean of Graduate Studies

ACKNOWLEDGEMENTS

Graduate study as a PhD student is an interesting and invaluable learning experience for me. First of all, I would like to acknowledge my academic advisor, Dr. Goutam Koley, for offering me this opportunity to study in the interdisciplinary research area of biosensors and bioelectronics. In the past 5 years of my graduate study, Dr. Koley has been providing me endless help and guidance. In addition to his countless effort in many hours of discussion with me on daily research work, I especially appreciate his help for training me to have an open mind towards initially unexpected experiment results and further enhance my ability of critical thinking when facing “real world” issues involved in hands-on experiment. Under his influence, I have a better understanding in opportunities and associated responsibilities as a future engineering professional in this information and technology era.

Here, I would like to also acknowledge my PhD committee members, Dr. Walsh, Dr. Chandrashekhar and Dr. Wang. I would like to thank Dr. Walsh, also as our research collaborator from School of Medicine at USC, for providing me the very interesting research topic of biocompatible ion sensor development for cell ion channel drug discovery and his support, guidance and encouragement in everyday research work. I would like to also thank Dr. Chandrasekhar and Dr. Wang for providing me their valuable suggestions and insightful questions for my research work.

I would like to express my gratitude to many other people, who helped and supported me a lot in my academic career. I would like to thank Dr. Xiaodong Yin and Dr. Chuanbing Tang from Department of Chemistry and Biochemistry, for their support in the preparation of ion selective membrane for the biocompatible ion sensor development. I would also like to acknowledge Prof. Richard A. Webb and Prof. Tangali S. Sudarshan, who generously granted me the access to their clean room facility for device fabrication and characterization. I am also grateful to Prof. Christopher T. Williams for allowing me to use his Raman spectroscopy for graphene study.

I would like to thank all the colleagues at NESL lab at different times. It is my honor to have the opportunity to work and study together with them and I got countless help and also inspiration from them in everyday research work. My special thanks to Dr. Xinchuan Liu, who gave me valuable suggestions and guidance at my early stage of the PhD study and Rina Patel, who helped me with the device fabrication in the graphene ISFET development.

Last but not the least, I would like to thank all my loved ones, my parents, my relatives and Ms. Chen Li for everything they have done for me to succeed throughout my life. Thank and appreciate all their love and support whenever I am up or down in life.

ABSTRACT

The development and evolution of physiological sensors, from wearable to implantable, has enabled long term continuous physiological monitoring, making possible for the out-of-clinic treatment and management of many chronic illnesses, mental health issues and post-surgery recovery. This technology advance is gradually changing the definition of health care and the way it is delivered, from clinic/emergency room to patient's own environment. In this dissertation, three general types of sensors have been proposed for physiological monitoring of blood pressure, oxygen content and electrolyte ion concentration level in human body, respectively. The study proved the device concepts and shows promising results with the prototype sensors for possibilities of various biomedical applications.

In the pressure sensor development, we have designed, fabricated and characterized a biocompatible, flexible pressure sensor using Au thin film patterned polydimethylsiloxane (PDMS) membrane for bio-implant application. Strain induced changes in Au film resistance was used to perform quantitative measurement of absolute pressure. The sensor was extensively modeled through COMSOL-based finite element simulations for design and performance predication. Three prototype sensors fabricated with different membrane thickness of 50, 100 and 200 μm were studied. Very high constant sensitivities of 0.1 /Kpa, 0.056 /Kpa and 0.012 /Kpa, respectively, were observed over their effective measurement ranges. The high sensitivities are attributed to the formation of microcracks in Au film resistor when the sensors are subjected to

pressure. Interestingly, the formation of microcracks seemed to be quite reversible within certain pressure range. In addition, the correlation of sensitivity and effective sensing range with membrane thickness was studied for the three sensors. It was found that the device sensitivity increased with the decrease in membrane thickness but at the expense of its effective sensing range. This observation corresponds well to the simulation results. Response times of all the three sensors were found to be in millisecond range, and the best rms noise limited resolution was 0.07 mmHg (9 Pa).

In the oxygen sensor development, oxygen sensing characteristics of In_2O_3 thin film at room temperature have been investigated through conductivity measurements using interdigitated metal finger patterned devices. We observed that the O_2 sensitivity gets affected very significantly in presence of moisture, as well as with applied dc bias. The O_2 sensitivity was found to increase several times in moist ambient compared to dry ambient condition. Higher dc bias also dramatically improved the sensitivity, which varied more than two orders of magnitude as the dc bias was increased from 0.5 to 10 V. We propose that the observed increase in sensitivity in presence of moisture is caused by enhanced surface electron density on In_2O_3 thin film resulting from the donation of electrons by the chemisorbed water molecules. The adsorption of O_2 molecules, which subsequently formed O^{2-} ions, leads to chemical gating of the sensor devices, which under larger dc bias produced a higher fractional change in current leading to higher sensitivity.

In the development of biocompatible ion sensor, a novel ion sensitive field effect transistor (ISFET), fabricated using chemical vapor deposition (CVD) derived graphene, has been proposed and demonstrated for real-time K^+ efflux measurement from living cells. Ion concentration change in electrolyte solution is transduced into an electrical (current) signal due to surface potential change in graphene (the material constructing the electrical conducting channel of the ISFET). Graphene, a two-dimensional carbon allotrope recently discovered in 2004, has a number of exceptional material properties which is much superior to silicon with respect to developing sensors for bio-detection applications, such as its ultra-high carrier mobility, excellent biocompatibility and very good chemical stability. In this work, we have extensively studied the I-V and C-V characteristics of the graphene ISFET in both electrolyte and physical buffer solutions with different K^+ concentration. Valinomycin coating of the graphene ISFETs has been utilized to enhance ionic detection sensitivity and impart selectivity. With the ionophore modified graphene ISFET, we have successfully demonstrated real-time detection of K^+ concentration change in both electrolyte and physiological buffer solutions.

Moreover, we have conducted cell based real-time K^+ efflux measurement utilizing commercial Si based ISFETs, proving the concept of ISFET based ion channel screening assay for drug discovery. On the other hand, the prototype graphene based ISFET has also been evaluated for K^+ efflux detection using a salt bridge configuration, showing promising sensing results for future study.

In the fabrication of graphene ISFET, we found the epoxy glue used for the sensor encapsulation had significant effect on the electric transport properties of graphene including conductivity, carrier concentration and field effect mobility. N-type doping effect of the epoxy on graphene has been carefully identified and confirmed by systematic experiments, which is promising for new alternative approach to dope graphene.

TABLE OF CONTENTS

LIST OF TABLES

LIST OF FIGURES

CHAPTER 1

INTRODUCTION

1.1 Background and Significance

In recent years, a variety of wearable and implantable devices have been developed to real time monitor different human physiological parameters from blood pressure [1], oxygen content [2], body temperature [3] to electrolyte concentration level [4] (Na^+, K^+ and Cl^- etc.). Among them, blood pressure, oxygen content and electrolyte concentration level are the three vital parameters, indicating the health condition of human being.

In particular, during and after cardiac surgery of infant/child, physiologic parameters such as blood pressure, oxygen tension, pH and temperature can change rapidly requiring immediate medical intervention. Continuous physiological monitoring of these parameters is critically needed in clinical practice. Presently, intracardiac pressures are monitored by fluid-filled catheters that are placed during surgery within the heart and tunneled out through the heart wall and skin to connect to an external transducer, as shown in Figure 1.1. Despite their clinical importance and benefits, bleeding, infection and malfunction associated with the maintenance and removal of these intracardiac catheters provide specific risks to the patient. Meanwhile, oxygen measurements require removing significant volume of blood from the patient for blood gas analysis. This not only wastes blood volume in sometimes very small patients, blood gas analysis does not allow for continuous oxygenation monitoring in critically ill patients. There is an ever growing demand for novel sensing solutions that offer direct intracardiac pressure and oxygen monitoring with little or no bleeding and infection risks. Considering the size constraints in infants and small children, the dimensions of the proposed sensor devices should be scalable, allowing for sufficient miniaturization.

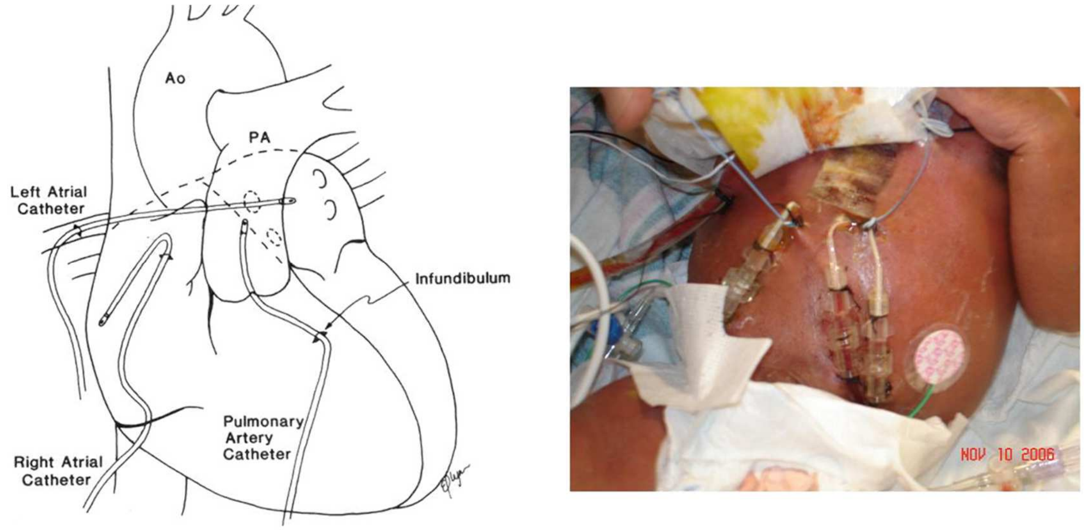

Figure 1.1: (a): Schematic drawing of intracardiac catheters probing various physiologic parameters (intracardiac pressures, oxygen tension etc.) at different locations within the human heart. (b): Typical transthoracic intra-cardiac catheters placed in a neonate following cardiac surgery.

On the other hand, sensing solution, which offers the capability of real-time monitoring electrolyte ion concentration level in physiological solution, also has its practical biomedical importance. In specific, high throughput, cell-based screening assays are now widely used for identifying compounds that serve as ion channel modulators in ion channel drug discovery. Various screening technologies have been developed in recent years including fluorescence, automated electrophysiology and ion flux assays. However, instrumentation for automated analysis of ion channels in primary and stem cells is lacking. A non-invasive, biocompatible electrolyte ion sensor with characteristics of low cost, miniaturized size, rapid sensing response and large-scale integrative electronic capacity is highly desired for designing next generation automated screening assay (as illustrated in Figure 1.2) adaptable for drug discovery of ion channels especially in primary and stem cells .

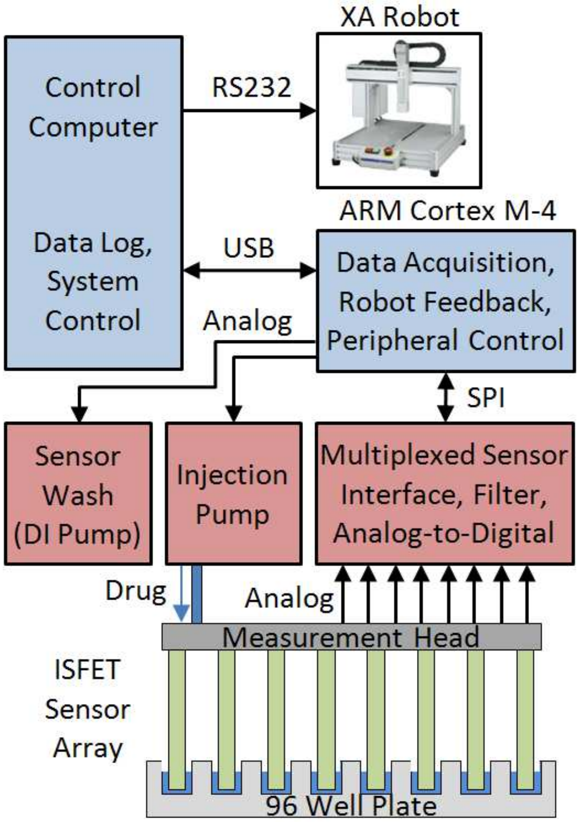

Figure 1.2: Schematic diagram of a prototype 96-well plate automated screening assay [5]. System consists of a 1) recording head containing 8 ISFETs (ion sensitive field effect transistor as the biocompatible ion sensor proposed in this report) with incorporated on chip Ag/AgCl reference electrodes and capillaries for drug perfusion, 2) xyz robotic stage for automatically moving the measurement head and plate, 3) peristaltic pump for solution perfusion, and 4) wash trough for cleaning the ISFETs.

To meet the practical needs in the clinical/biomedical applications above, we proposed and demonstrated three general types of thin film based sensors for pressure, oxygen and ion detection, respectively. Detail of each sensor development is discussed in the following chapters of the dissertation.

1.2 Outline of the dissertation

In chapter 2, we presented the development of a PDMS thin film based biocompatible/bio-implantable pressure sensor. For sensor design and performance prediction, COMSOL based finite element simulation was performed and the simulation results are presented. Three prototype pressure sensors with different PDMS membrane thicknesses were fabricated and characterized. The fabrication and electrical characterization of the pressure sensors are discussed in detail in the chapter. Based on the electrical measurement results, correlation of sensor sensitivity and effective sensing range with PDMS membrane thickness is also discussed. A simple physical model was proposed to explain the sensing mechanism of the pressure sensor. The RMS noise, noise limited resolution and response times of the pressure sensor are discussed at the end of the chapter.

Chapter 3 mainly discussed our recent investigation on oxygen sensing characteristics of In_2O_3 thin film under the effects of moisture and dc bias. After a brief literature review on oxygen detection using metal oxide films, fabrication of the In_2O_3 thin film based oxygen sensor and the experimental setup for amperometric detection are discussed. From the amperometric measurement, we found that the O_2 sensitivity gets affected very significantly in presence of moisture, as well as with applied dc bias. A simple model is introduced correlating the oxygen sensitivity with humidity and electrical bias in the *Results and Discussion* section of the chapter.

Chapter 4 is basically dedicated to the design and fabrication of a novel grapheme based ion sensitive field effect transistor for K^+ detection in electrolyte solution. Sensor fabrication, starting from a fresh CVD derived graphene on Cu foil to a well packaged graphene ISFET was discussed here. Evaluation on the epoxy encapsulated graphene ISFET, in terms of electrical insulation, chemical stability and biocompatibility, is presented. Effect of epoxy on the electric transport properties of graphene was experimentally observed and is also presented here. For better sensor performance, optimization of the sensor packaging using biocompatible photoresist is proposed at the end of the chapter.

We present all the experimental measurements performed on our fabricated graphene ISFETs and commercial Si based ISFETs in Chapter 5. In the first half the chapter, I-V and C-V characterization of the fabricated graphene ISFET in both electrolyte and physiological buffer solutions are discussed. Valinomycin coating of the graphene ISFETs has been utilized to enhance ionic detection sensitivity and impart selectivity. In the second half of the chapter, time dependent K^+ detection using valinomycin/polymer modified graphene ISFET is presented and discussed. Real-time cell based K^+ efflux measurement using both commercial Si based ISFET and the graphene ISFET is discussed at the end of the chapter.

Chapter 6 summarized all the major contributions of this work to the research community. Also we propose future research plan for each of the three sensors here.

CHAPTER 2

BIOCOMPATIBLE PRESSURE SENSOR

2.1 Thin film/membrane based pressure sensor: A brief review

Thin film/membrane based pressure sensors have wide applications in several different fields including bio-implantable devices and electronic artificial skin. A variety of pressure transduction schemes exist based on optical [6], capacitive [2], piezoelectric [7], and piezoresistive transduction mechanism.[8] Among them, membrane based pressure sensors most commonly utilize either capacitive or piezoresistive methods to transduce the pressure induced membrane deflection into an electrical signal. Capacitive pressure sensor normally consists of a parallel plate capacitor with a conductive floating electrode and another stationary electrode placed in close proximity. As shown in Figure 2.1, the pressure induced deflection of the flexible membrane causes changes in the capacitance

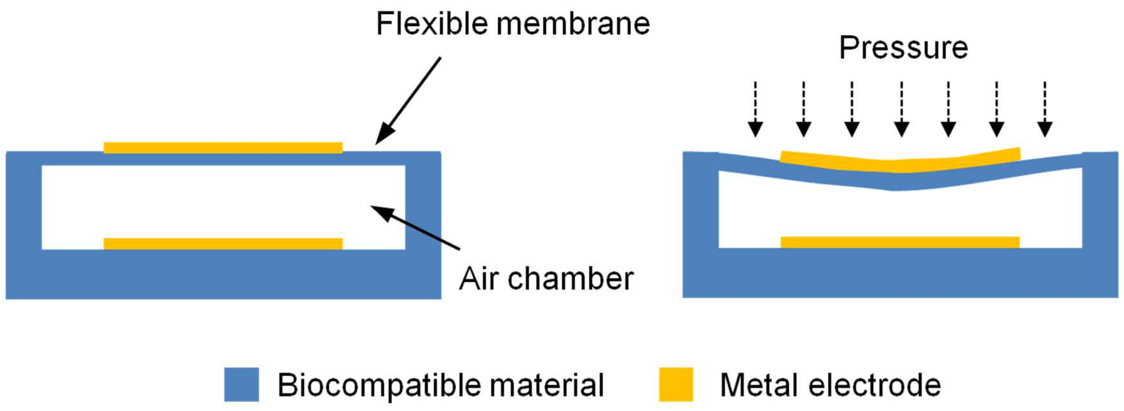

Figure 2.1 Schematic illustrating general structure of a capacitive-based membrane pressure sensor and its operation when subjected to pressure.

between the electrode pair. The capacitance change can be determined from the change in ac current flowing between the two plates of the capacitor upon application of an externally applied ac voltage. [2] Various designs of capacitive pressure sensors utilizing either silicon or flexible membranes have been reported in the past research efforts. Leineweber *et al.* [9] reported a capacitive tactile sensor chip to measure the distribution of forces that act on its surface. The transducer element is a dynamic capacitor, which consists of a polysilicon membrane as a floating electrode and bottom electrode implanted in the silicon substrate. With similar design concept, the development of implantable bio-MEMs sensor based on a flexible silicon dielectric membrane has been presented by Simons *et al.*.[10] Zhou *et al.* [11] designed and fabricated a highly sensitive capacitor pressure sensor with a sandwich structure, drastically reducing the processing complexity associated with fabricating these sensors.

In addition to the silicon-based thin film pressure sensors discussed above, pressure sensor and strain gauges based on flexible biocompatible materials, such as polydimethylsiloxane (PDMS), parylene, or polyethylene terephthalate (PET) etc, are also extensively investigated in recent years due to biosensing applications. Cheng *et al.* [12] presented a capacitive tactile sensor with a floating counter electrode on PDMS thin membrane with top sensitivity of 0.02/KPa within 420 mm Hg. More recently, Mannsfeld *et al.* [13] reported a capacitive pressure sensor utilizing three-dimensional micromachined PDMS microstructure. The pressure sensor demonstrated a maximum linear sensitivity of 0.55 /Kpa under 15 mmHg, which compares very favorably with the sensitivity values achieved in previous reports. [14-17]

On the other hand, piezoresistive pressure sensors transduce the pressure/strain induced mechanical deformation of a material to the change in its electrical resistance. Lee and Choi [18] demonstrated a novel resistive pressure sensor by incorporating a carbon fiber (CF) on a flexible PDMS diaphragm. When subjected to pressure, the PDMS membrane deformed and results in a bend of the CF, which induces a detectable change in the electrical resistance of the fiber. Lim *et al.*[19] reported a flexible pressure sensor using piezoresistive amorphous silicon thin film patterned polyimide membrane for low-pressure (0 – 2 psi) sensing applications. More recently, integration of graphene films on PDMS has also been performed to develop stretchable and biocompatible strain gauges. [20] The gauge factor of the strain gauge was 6.1, which is better than that of conventional strain gauges based on metal alloys of ~2. [21]

The selection of one pressure transduction scheme over the other is dictated by the collective combination of advantages and disadvantages. Table 1 summaries the relative merits and demerits of membrane based piezoresistive and capacitive pressure sensors along with their potential applications. As can be seen from the table, both the transduction schemes have their own advantages and constraints. There is no ideal pressure sensor, which can be fit into all application scenarios. Beyond the initial selection of a pressure transduction scheme, the sensor design is also guided by a number of specific requirements set by individual application case. Moreover, nowadays a wide variety of material and fabrication processes have been adopted for pressure sensor development. There is always a tradeoff between sensor performance and manufacturing cost in actual sensor design.

Table 2.1: Relative merits and weaknesses of membrane based capacitive and piezoresistive pressure sensors.

Type of Sensor	Merits	Weakness	Potential applications
Piezoresistive	Good sensitivity Fast response time Low noise Low cost Easy read-out mechanism Planar device structure and easy for integration	Temperature sensitive Hysteresis High power consumption	• Low-pressure sensing in harsh natural environment [19] • Flexible and wearable strain sensors for human motion detection [22] • Implantable biosensor for cardiovascular pressure monitoring
Capacitive	High sensitivity and pressure resolution Low power consumption Good frequency response Low noise Low cost	3-D device structure and difficult for integration On-site detection/amplification circuitry needed due to small active capacitance Hysteresis	• Ultra sensitive e-skin [13] • Implantable biosensors for intraocular [23] and cardiovascular [2] pressure monitoring.

2.2 PDMS based biocompatible pressure sensor

Of the biocompatible materials, PDMS has emerged as the material of choice for biosensor development due to its well-known biocompatibility [24], chemical inertness [25], ease of molding[26] and high flexibility[27]. Due to its lower Young's modulus, PDMS thin film based pressure sensor has much higher sensitivity, especially in a low pressure region, which has prompted its usage in a variety of biocompatible pressure sensors [2, 10, 28] and artificial skin applications. [8, 13, 29, 30] K. F. Lei *et al.* [31] developed a flexible PDMS capacitive pressure sensor for plantar pressure measurement in biomechanical applications. The sensor was fabricated using a 30 μm PDMS thin film as the dielectric layer (also the compressive layer) of the capacitor. By tuning the elasticity of the PDMS, optimal sensor sensitivity and linearity was experimentally achieved. Le Cai *et al.* [32] designed a stretchable capacitive strain sensor/gauge based on carbon nanotube (CNT) /PDMS composite film for human motion detection. The device was demonstrated to be capable of detect uniaxial strain up to 300% with reliable sensor performance due to superior strechability of the composite film. Jongchan Kim *et al.* [33] demonstrated an implantable pressure sensor utilizing a commercial thin-film strain gauge embedded in a PDMS diaphragm. The sensor was verified for biomedical applications by performing in-vivo test monitoring the rabbit bladder pressure.

In this dissertation, a miniaturized, low cost and fully biocompatible pressure sensor with high sensitivity in low pressure region (<10 Kpa) has been proposed and demonstrated. The pressure sensor is based on resistance changes of an Au thin film resistor patterned on a flexible polydimethylsiloxane (PDMS) membrane. PDMS is utilized to construct the main body and the flexible component (membrane) of the prototype pressure sensor. Au is chosen to be the material of the thin film resistor because of its high conductivity, inertness to most of chemicals (acids and solvent), well known biocompatibility and proven high ductility. [34] The following sections in this chapter discussed in detail the sensor design, fabrication and its electrical characterization.

2.3 Pressure sensor deign, modeling and device fabrication

2.3.1 Sensing mechanism

The operation of our PDMS based pressure sensor is based on the change in resistance of an Au thin film resistor patterned on a flexible PDMS membrane with change in applied pressure. Figure 2.2 schematically illustrates its sensing mechanism. When uniform differential pressure is applied at the bottom of the PDMS thin membrane, it deforms and induces strain on the Au thin film resistor patterned on the membrane which in turn results in an electrical resistance change of the resistor. The change in resistance can be determined from the change in DC current flowing through the resistor upon application of an externally applied DC bias, thus transducing an analog signal (pressure) into an electrical signal (current/resistance).

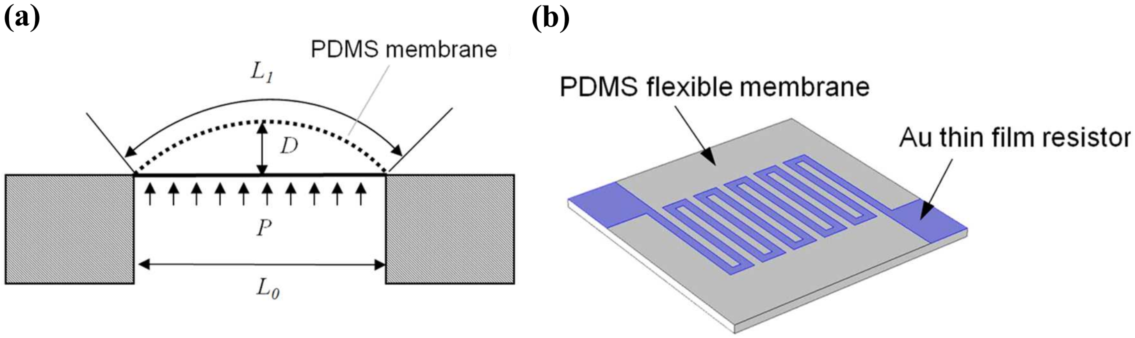

Figure 2.2 (a) Schematic drawing illustrating PDMS based resistive pressure sensing. (b) PDMS flexible membrane patterned with Au thin film serpentine resistor is fixed at its four edges. Upon applied pressure, it deforms and results in a pressure induced resistance change of the thin film resistor.

The sensitivity of the pressure sensor can be modeled using the strain induced resistance change of a metal thin film resistor. According to Ohm's law, the resistance of a thin film resistor (as shown in Figure 2.3 (a)) is given by Equation 1.1, [35]

$$R = \frac{\rho L}{A} = \frac{\rho L}{WT} \quad (1.1)$$

where ρ is the resistivity of the metal material, L the length, A the cross section area, W and T the width and the thickness of the cross section. Differential Eq. (1.1), we have

$$\frac{dR}{R} = \frac{dL}{L} - \frac{dW}{W} - \frac{dT}{T} + \frac{d\rho}{\rho} \quad (1.2)$$

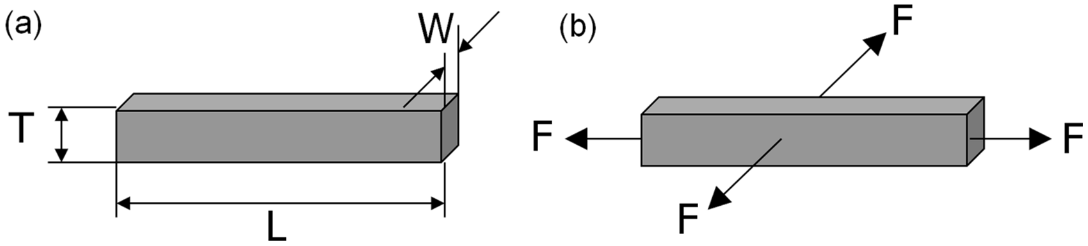

Figure 2.3 Simplified model of a metal thin film resistor with **(a)** and without **(b)** being subjected to symmetric biaxial tensions.

When the thin film resistor is subjected to symmetric biaxial tensions (as illustrated in Fig. 2.3 (b)), the induced strains along the length, width and thickness directions are given by,

$$\varepsilon_L = \varepsilon_W = \varepsilon$$

$$\varepsilon_T = -\frac{2\mu}{1-\mu}\varepsilon \quad (1.3)$$

where μ is Poisson's ratio and lies in the range of 0.3 to 0.45 for most metals. Substituting Eq. 1.3 into Eq. 1.2 and according to the definition of strain, we have,

$$\frac{dR}{R} = \left(\frac{2\mu}{1-\mu}\right)\varepsilon + \frac{d\rho}{\rho} \quad (1.4)$$

where dR represents the strain induced resistance change of the resistor and dρ resistivity change due to the deformation of the crystal lattice of the material. Thus, the gauge factor of the thin film resistor (the sensitivity of the PDMS based pressure sensor here) can be determined as,

$$G = \frac{\frac{dR}{R}}{\varepsilon} = \left(\frac{2\mu}{1-\mu}\right) + \frac{\frac{d\rho}{\rho}}{\varepsilon} \quad (1.5)$$

2.3.2 *Sensor design and modeling*

The device structure of our PDMS based pressure sensor is schematically illustrated in Figure 2.4. For the sensor to be implantable in neonatal heart, its dimensions are restricted to be ~5 x 5 mm^2 or less. The effective sensing area of our prototype pressure sensor (which was defined by the black square frame in the figure) is kept at 3 x 3 mm^2. Three sensors with different PDMS membrane thickness of 50, 100 and 200 were fabricated and characterized respectively in this study. For ease of handling, the peripheral dimensions of the entire device are kept at 10 mm x 10 mm x 5 mm (length x width x thickness), which can be further miniaturized later as needed. The PDMS frame walls and the thin membrane enclose an air chamber with dimensions 3 x 3 x 2 mm^3, which was used to put desired pressure on the PDMS thin membrane. A polyvinyl chloride (PVC) tube with an outer diameter of 3/32 inch was attached to the sidewall of the cavity through a hole on the PDMS wall (Fig.1 (a)). A serpentine Au thin film resistor was patterned on the top surface of the PDMS membrane using a laser patterned shadow mask. The width, length and thickness of the Au film stripe were 100 μm, 17.5 mm and

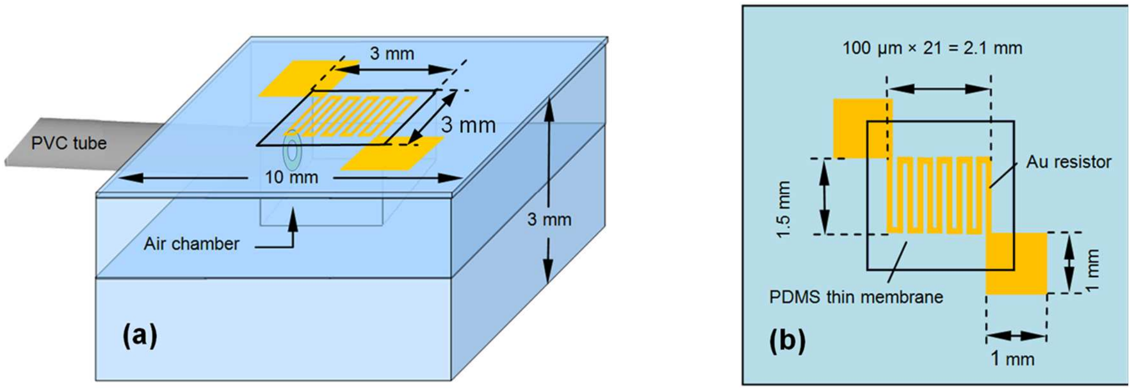

Figure 2.4 (a) Three-dimensional schematic diagram of the PDMS thin membrane-based pressure sensor. (b) The top view of the sensor with the dimensions.

200 nm, respectively. Two 1 mm x 1 mm contact pads were deposited at the two ends of the resistor to establish external electrical contacts.

Since PDMS as a rubber-elastic material has a non-linear stress-strain relationship, the complex 3-D deformation of the PDMS membrane under applied pressure causes the difficulty in calculating membrane deflection, strain and stress at Au film stripe. For sensor design and performance prediction, we used the finite element simulation tool, COMSOL Multiphysics® 4.0 (a software platform for physics-based modeling and simulation), to determine the pressure induced membrane deflection, strain distribution, maximum and average strain on the PDMS thin membrane and Au film strip. To characterize the PDMS membrane deflection, a nonlinear Moony-Rivlin stress strain relationship was used, which is uniquely suited for rubber-elastic deformations. [36, 37] The Young's modulus of PDMS has measured values reported as from 150 K to 3.5 MPa, which largely depends on the material processing parameters (e.g. curing temperature [38] and base/agent mixing ratio [39]) and measurement conditions. In our simulation, we set the Young's modulus to be 3.0 MPa because its corresponding pressure induced membrane deflection obtained from the simulation is close to the value experimentally observed. Figure 2.5 shows the strain distribution on the top surface of a PDMS membrane of 150 um and of the Au thin film serpentine pattern (strip) under 50 mmHg (~6.7 Kpa) pressure. Non-uniform strain distribution both on the membrane and the Au thin film strip was observed, with maximum strain occurring at the center and in the vicinity of the four fixed edges of the membrane (Fig. 2.5 (a)) and at the junctions between the serpentine resistor and contact pads of the Au film strip (indicated by the red arrows Fig. 2.5 (b)). Figure 2.6 (a) shows the pressure induced membrane deflection for

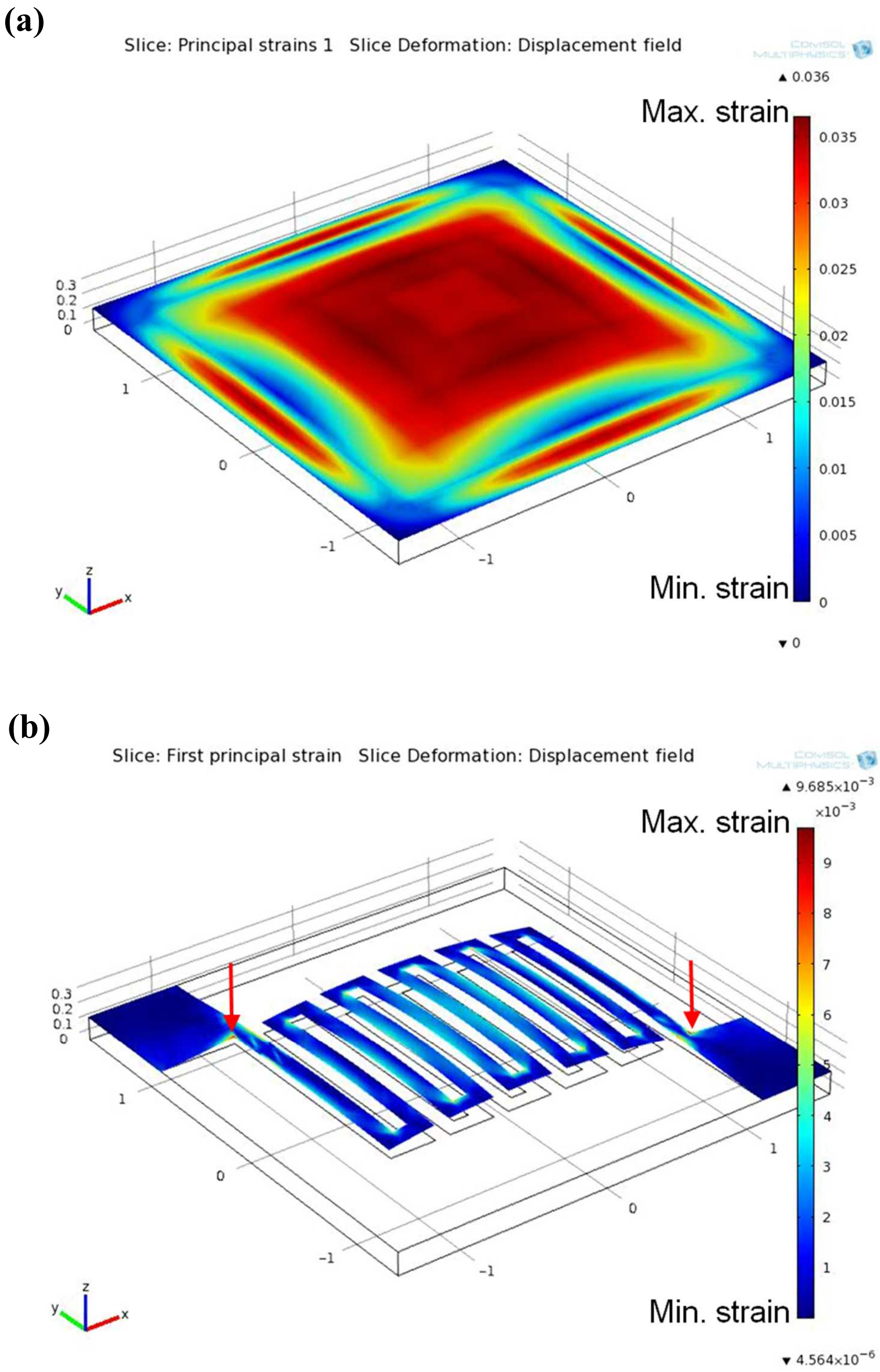

Figure 2.5 Pressure induced strain distribution on the top surface of **(a)** a 150 um PDMS membrane solely and of **(b)** an Au thin film resistor patterned on the PDMS membrane of the sensor under 50 mmHg pressure. Red arrows indicate the locations on the Au film strip where maximum strain was.

different membrane thickness of 50, 100 and 200 µm, respectively. As we expected, thinner membrane is subjected to larger deformation under same applied pressure, thus larger strain at the Au film strip. Fig. 2.6 (b) and (c) shows the variation of the maximum and the average strain at the Au film strip with the applied pressure from 0 – 50 mmHg.

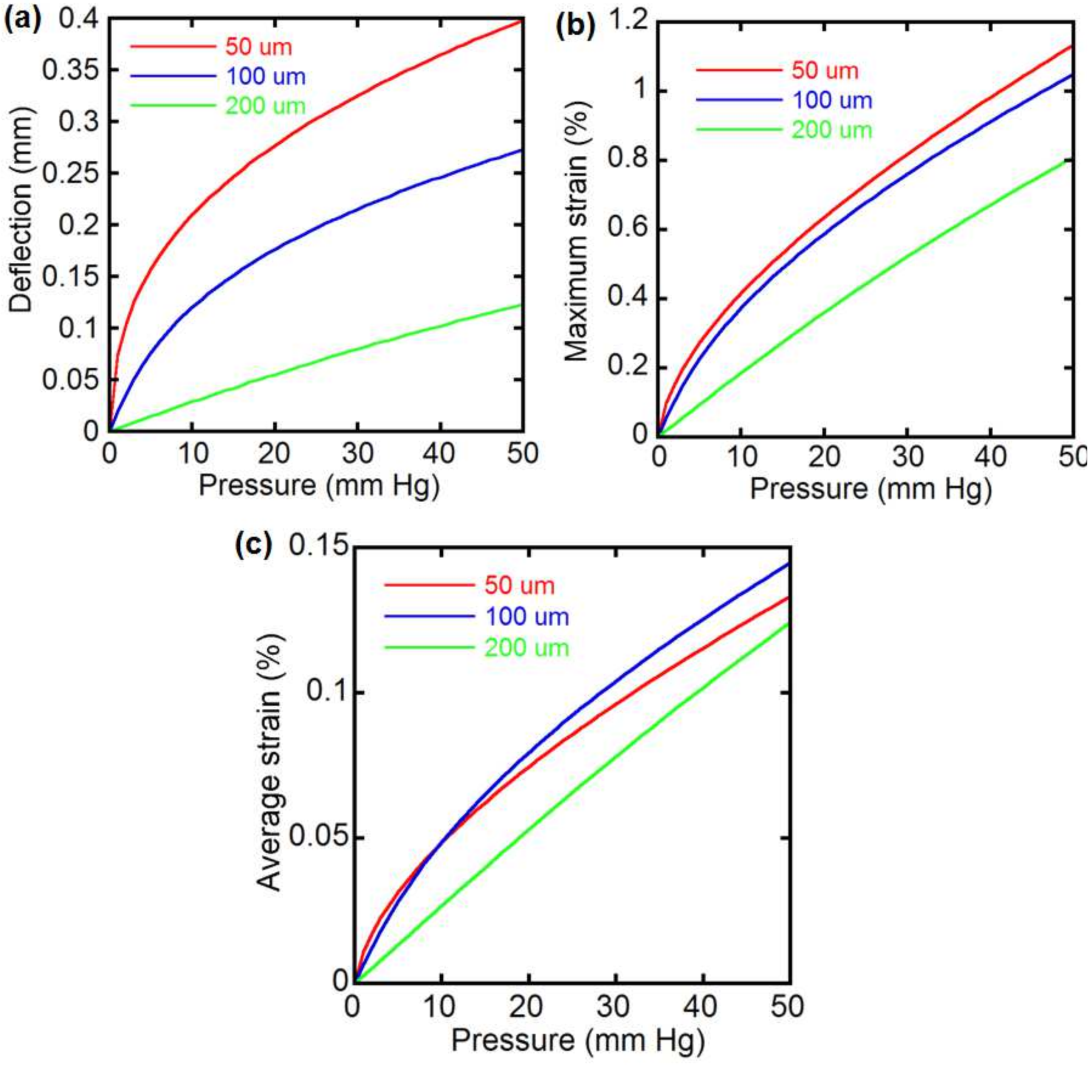

Figure 2.6 (a) Change in the membrane deflection with applied pressure for membrane thickness of 50, 100 and 200 µm, respectively. (b) and (c) Variation of the maximum and the average strain with pressure.

2.3.3 *Device fabrication*

Three PDMS based pressure sensors with membrane thickness of 50 μm, 100 μm and 200 μm were fabricated respectively. The pressure sensor was realized by bonding a PDMS thin membrane to an air chamber made of PDMS thick walls. Figure 2.7 (a) gives the detailed device fabrication process.[40] PDMS was prepared by mixing the elastomer base and curing agent as the weight ratio 10:1 using Sylgard 184 silicone elastomer kit

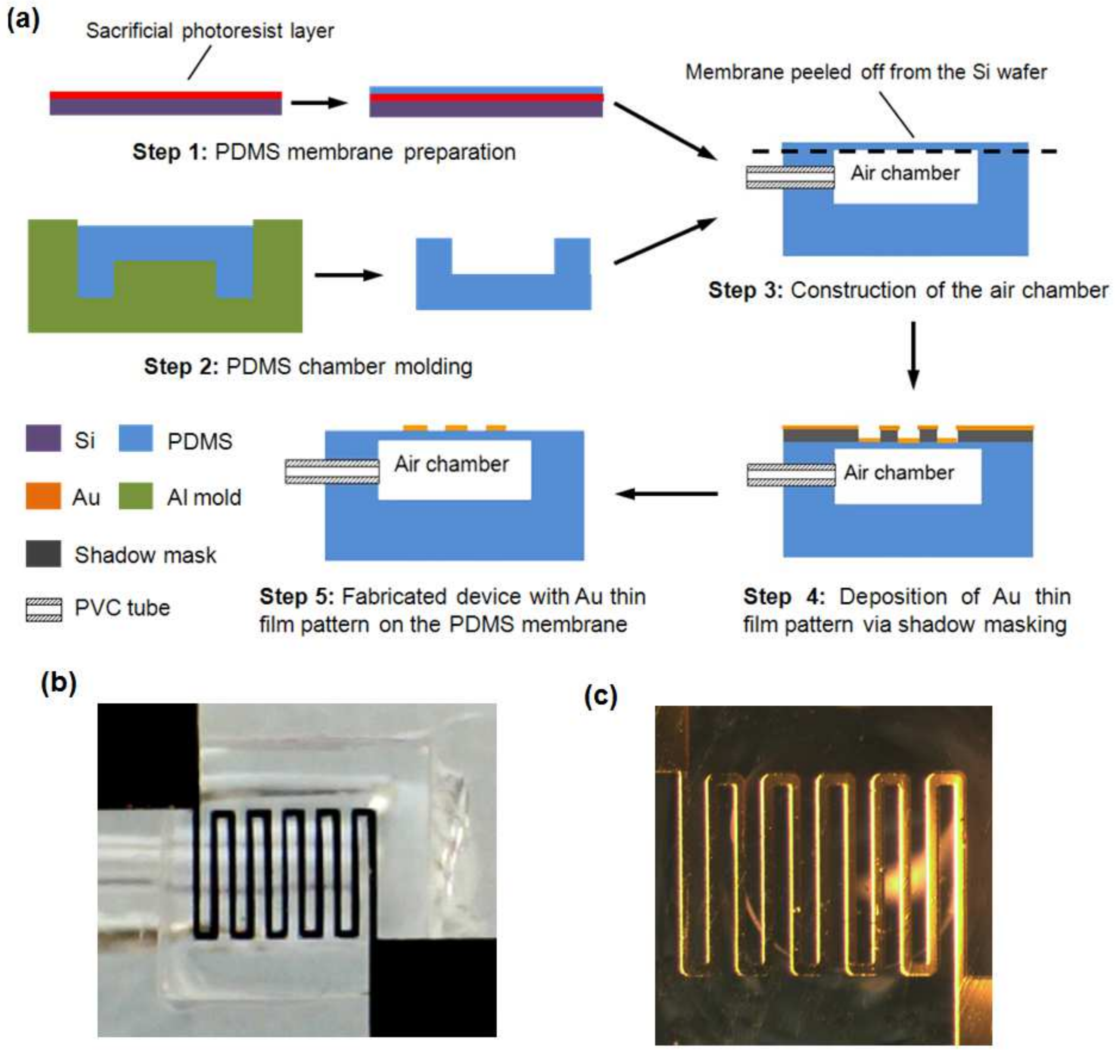

Figure 2.7 (a) Fabrication process flow diagram of the pressure sensor. (b) Optical image of a representative pressure sensor with a 200 nm thick Au serpentine pattern (c) Magnified image of the Au pattern.

(Dow Corning Co.). The base/agent mixture was then degassed in a desiccator for ~30 mins. PDMS membranes of 50, 100 and 200 µm thick were spin coated on Si wafers with a pre-coated sacrificial layer of photoresist (PR) 1811 and then air-dried by baking the supporting wafers at 95 °C for 5 hours (Step 1). The membrane thickness was controlled by choosing the rotational speed of a spin coater. Acetone was applied to solve the sacrificial PR layer when the PDMS thin membrane was being peeled off. The chamber with thick PDMS wall was built using molding method in an aluminum mold (Step 2). A Polyvinyl chloride (PVC) tube (Tygon®) was mounted on the wall for air inlet and outlet and the PDMS thin membrane was then bonded onto the chamber (Step 3). Au thin film pattern (200 nm in thickness) was deposited onto the membrane using electron beam evaporation (DV-502A, Denton Co.) and a laser-cut polyimide film (Kapton®, DuPont Co.) as shadow mask with 300 µm in thickness (Steps 4 and 5). Fig. 3 (b) and (c) shows a well-defined Au serpentine resistor on a 200 µm thick PDMS thin membrane of a representative pressure sensor.

2.4 Sensor electrical characterization

2.4.1 Experimental setup

The sensor electrical characterization was performed on a probe station. The schematic diagram of the experiment set-up is shown in Figure 2.8. The air pressure was applied to the device under test via a PVC tube using a commercial pressure pump (3D instruments, LLC.). To accurately monitor the differential pressure applied on the PDMS membrane (taking into account the ambient atmospheric pressure), a commercial pressure gauge (Omega, DPG5600B-05G) was mounted on the pump. A steady DC bias of 0.5 V was supplied to the measurement system and time-dependent resistance change of the sensor in response to applied pressure was logged using a data acquisition unit (Agilent 34972A). The acquired data was transmitted to a computer through a LAN connection for processing.

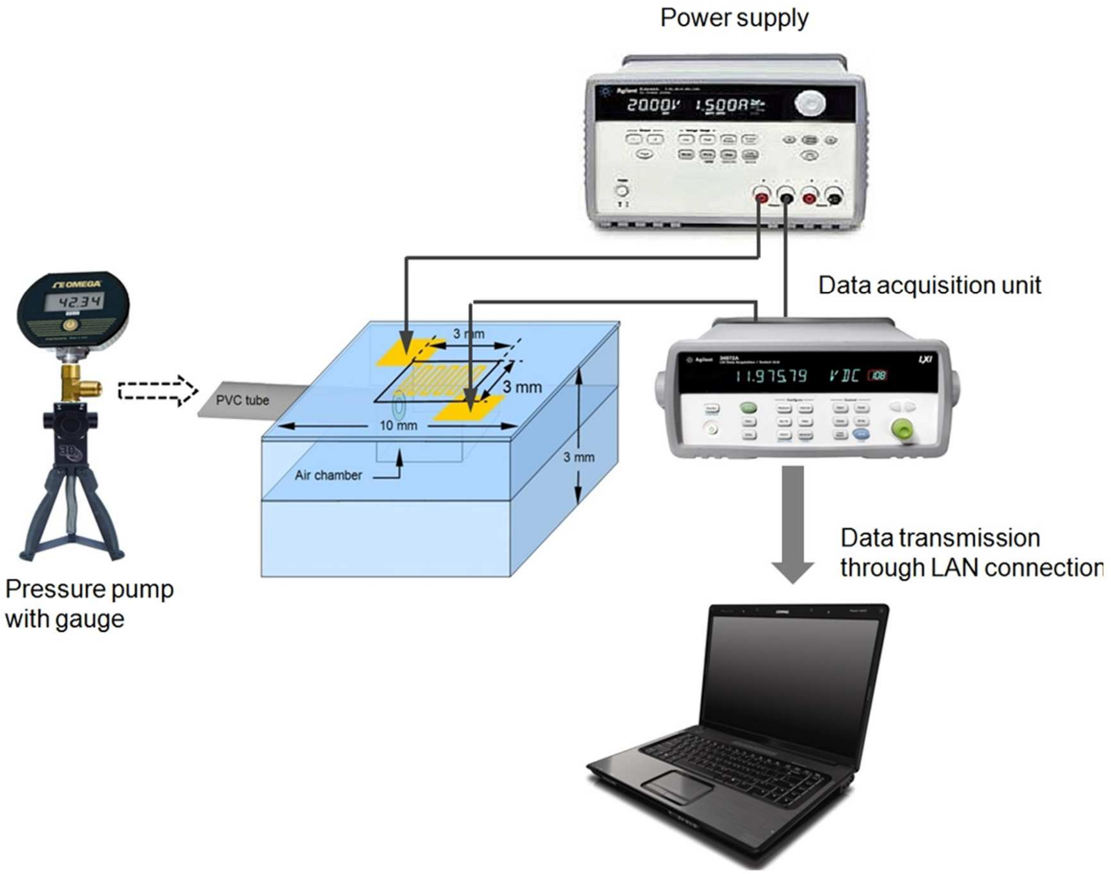

Figure 2.8 Schematic diagram of the experimental set-up for sensor electrical characterization.

2.4.2 Sensing results and discussion

A. Sensitivity dependence on the PDMS membrane thickness

The sensitivity of our PDMS flexible pressure sensor is defined as Sensitivity (S) = $(\Delta R/R_0) / \Delta P$, where ΔP is the pressure changes, R_0 initial resistance of the metal thin film and ΔR pressure induced resistance change. Figure 2.9 (a) shows the relative resistance change ΔR/R0 vs. the applied pressure curves for the sensors with three different PDMS membrane thickness of 50 µm, 100 µm and 200 µm respectively. It was observed that, in general, the device sensitivity (given by the slopes of the curves) increases with the decrease of the membrane thickness. Sensors with thinner membrane have higher sensitivity because under the same applied pressure, thinner membrane is subjected to larger deformation (Fig. 2.6 (a)) thus larger strain (Fig. 2.6 (b)) will be induced on the Au thin film resistor resulting in larger resistance change. Therefore, it is possible to further enhance the sensitivity of our pressure sensor by scaling down the thickness of the PDMS membrane.

The sensitivities of 50 µm sensor, 100 µm sensor and 200 µm sensor are 0.1/Kpa in 0 – 28 mmHg, 0.056/Kpa in 0 – 35 mmHg, and 0.012/Kpa in 0 – 40 mmHg pressure range respectively (listed in Table 2.2), which compare favorably with results reported earlier in the range of 5×10^{-4} – 5×10^{-2} /Kpa for similar dimensions of sensing area. [14, 15, 17, 29, 41-43] To further compare the performance of these sensors with other pressure sensors developed as strain gauges, it is necessary to calculate their strain gauge factor G. The calculation is, however, not very straightforward since the PDMS based pressure sensor has a non-uniform strain distribution under applied pressure as discussed in Section 2.3.2. Hence, the average strain (ε_{AV}) calculated over the top surface of the Au film strip was used to obtain the gauge factor G. The ε_{AV} of the three sensors with change in applied pressure was obtained from the COMSOL based simulation and plotted in Fig. 2.6 (c). Figure 2.9 (b) shows the relative resistance change $\Delta R/R_0$ with change in the average strain ε_{AV} for the three sensors. The gauge factors G, given by the slope of the

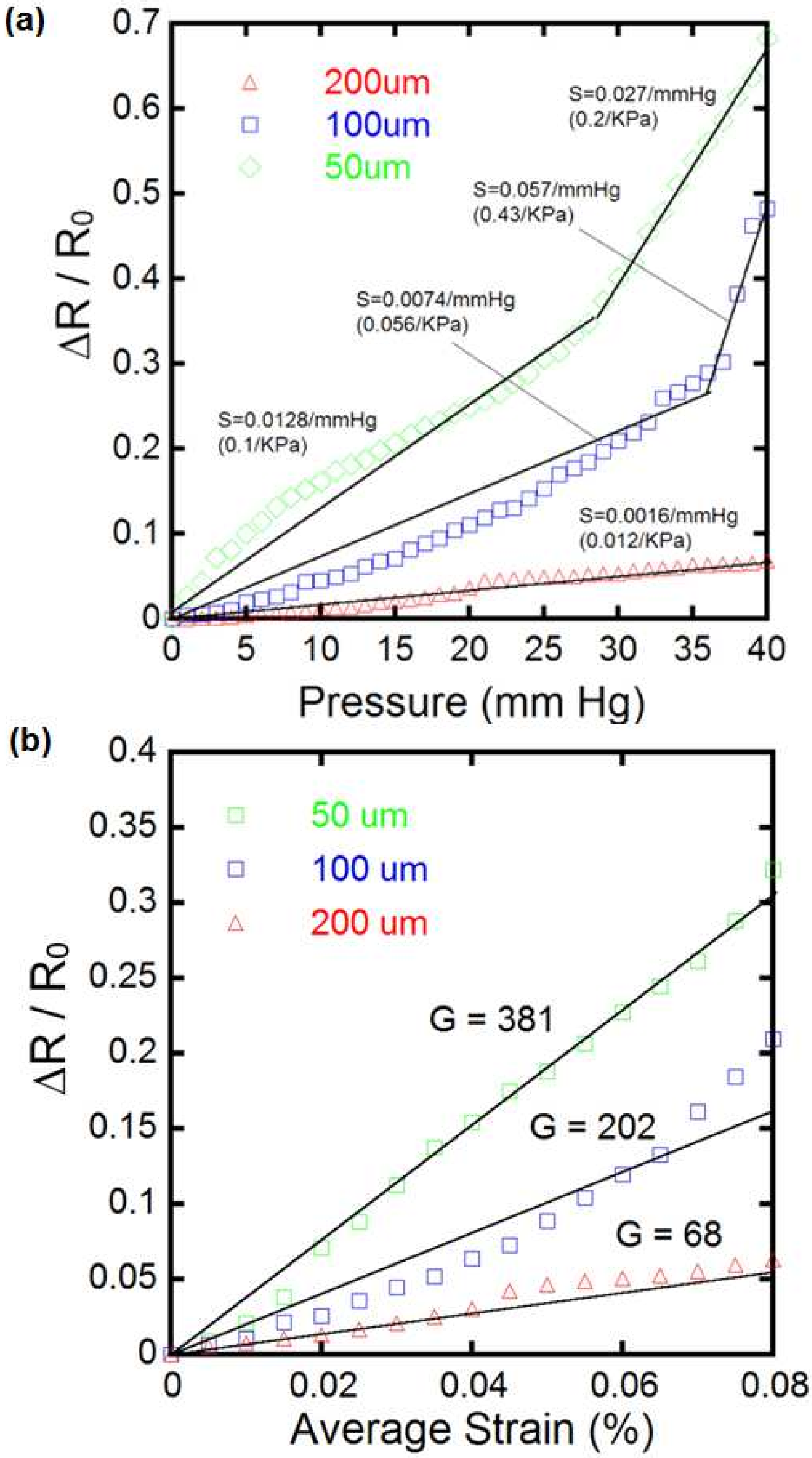

Figure 2.9 (a) Relative resistance changes $\Delta R/R_0$ vs. applied pressure for the 50, 100 and 200 μm sensors, respectively. (b) Relative resistance changes $\Delta R/R_0$ vs. average strain. The slope of the curves defines the strain gauge factor G.

curves, are 381, 202 and 68 for the 50, 100 and 200 μm sensors respectively, which has a much higher value than that of the commercial strain gauge based on metal alloys (G ~ 2) and those of the strain sensors which were reported earlier in the literature. [18, 44, 45]

Table 2.2: Sensor Performance characteristics of the fabricated pressure sensors.

	50 μm sensor	**100 μm sensor**	**200 μm sensor**
Effective sensing range	0 – 28 mm Hg	0 – 35 mm Hg	0 – 40 mm Hg
Sensitivity	0.013/ mmHg (0.1/KPa)	0.0074/ mmHg (0.056 /KPa)	0.0016/ mmHg (0.012 /KPa)
Gauge factor	381	202	68
Response time	216 ms	180 ms	172 ms
Relaxation time	125 ms	178 ms	310 ms
RMS noise	0.057 Ω	0.123 Ω	0.088 Ω
Resolution	0.07 mm Hg	0.15mm Hg	0.07 mm Hg

B. Effective sensing range

It was experimentally observed by Yu-Hsin Wen et al.[44, 45] that the maximum strain, without causing the Au thin film (100 nm – 200 nm) to crack, lay in the range of 0.8 % – 1.09 %. Based on their results, the maximum strain for our sensor was selected as 0.8 % for a reliable operation. Simulation results from our study (Fig. 2.6 (b)) revealed that, to an applied pressure of 40 mmHg, the pressure induced maximum strain on the Au film resistor are 1%, 0.9% and 0.67% for the 50, 100 and 200 μm sensors respectively. Thus the 200 μm sensor is expected to be capable of measuring pressure up to 40 mmHg. While, to the 50 and the 100 μm sensors, they are supposed to have a lower effective measurement (sensing) range. In our experiment, from the $\Delta R/R_0$ vs. Pressure curves

(Fig. 2.9 (a)), we found the 200 µm sensor operated in a linear relationship with the applied pressure over the entire measurement range from 0 to 40 mmHg. While to the 50 and 100 µm sensors, a sharp change in the slope of the curves occurred at 28 and 35 mmHg respectively. This abrupt sensitivity change implies that two different mechanisms were responsible for the sensor resistance change in these two operating regions i.e. 0 – 28 (35) and 28 (35) to 40 mmHg.

For the sensors operating in low pressure region, 0 – 28 (35) mmHg, we proposed that the resistance change was mainly attributed to the pressure induced micro-crack formation in the Au thin film resistor as discussed in our recent publication. [40] It has been reported in the literature [46-53] that the formation of microcracks is the major reason for causing strain-induced resistivity changes in metal thin films on polymer or elastomeric materials. Figure 2.10 (a) schematically illustrates the mechanism. When subjected to strain, the metal film cracks, but does not get completely disconnected, i.e. a very thin (sub-nanometer level) layer of metal at the bottom of the crack still conducts. [46, 49] However, this can give rise to a dramatic change in film conductivity. The mechanism of formation of microcracks has not been understood clearly yet. The cracks possibly arise from the imperfections in the grain boundaries of the deposited metal film. [51, 52] In our experiment, we observed that some initial microcracks are formed spontaneously following the deposition of the Au film, and more created in the Au layer when the PDMS membrane was subjected to pressure, as exemplified by the SEM images of a representative 200 µm sensor in Fig. 2.10 (b) and (c). Interestingly, the strain-induced microcrack formation was experimentally found to be quite reversible within certain pressure range, which is so called effective sensing range here. Within the effective sensing range (e.g. 0 – 40 mmHg for the 200 um sensor), the sensor presents a linear response to applied pressure with reliable performance (Fig. 2.9 (a)). Figure 2.11 shows the sensor response of a representative 200 um sensor in the 14 loading-unloading cycles. Clearly, for the applied pressure range (0 – 5 mmHg), the sensor performance is very consistent over the various cycles.

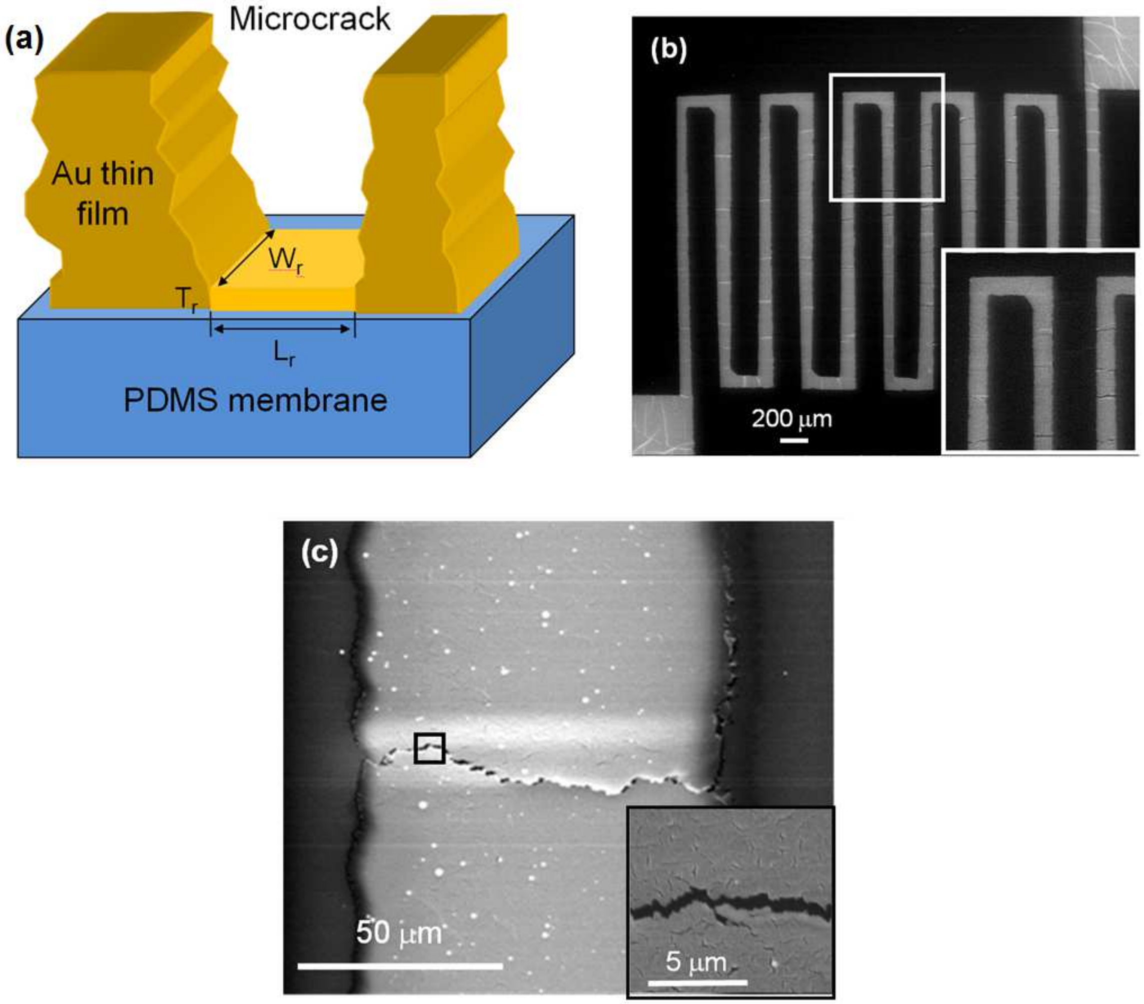

Figure 2.10 (a) Schematic illustration of a strain-induced microcrack in the Au thin film patterned on PDMS membrane. (b) An SEM image of the Au thin film resistor on a representative 200 µm sensor under 24 mmHg pressure. The inset gives a magnified view on one section of the resistor, clearly showing several microcracks. (c) Magnified view of a single microcrack. Inset shows the magnified image of the crack. Its length (L_r) and width (W_r) were estimated to be 0.8 and 104 µm, respectively.

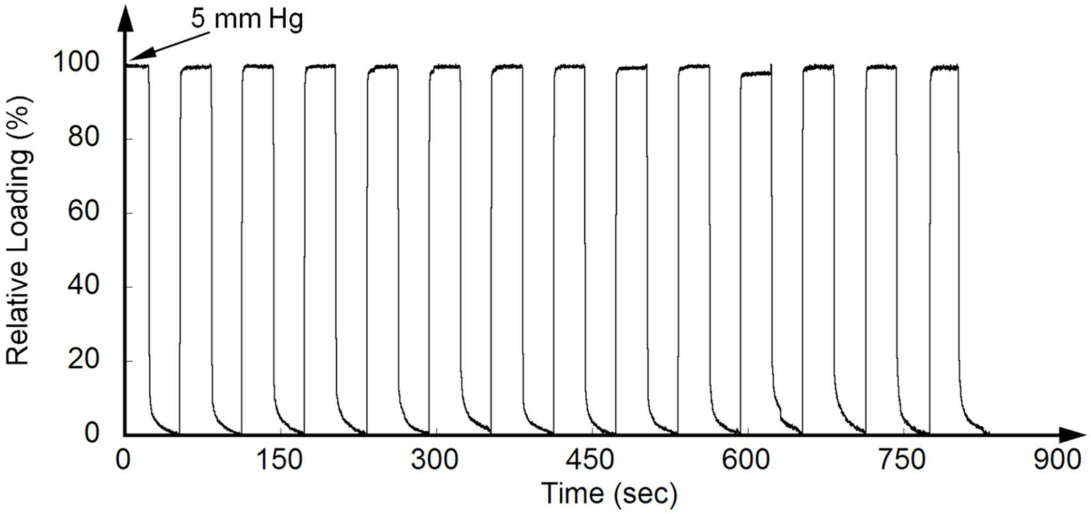

Figure 2.11 Sensor response of 14 consecutive loading and unloading cycles between 0 and 5 mmHg. In the measurement, the pressure was quickly adjusted manually from initial 0 mmHg (0 % relative loading) to 5 mmHg (100 %) relative loading). The pressure was kept at 5 mmHg for 30 seconds and then reduced back to 0 mmHg for another 30 seconds. The relative loading was calculated as $(R-R_0)/(R_{5\ \mathrm{mmHg}}-R_0)\times100\%$, where R is the measured resistance, R_0 and R_5 mm Hg are the resistance at 0 and 5 mmHg respectively.

For sensors operating at pressure region over their effective sensing range (e.g. 28 – 40 mmHg for the 50 um sensor), the sharp change in resistance can be attributed to the partial breaking of the Au resistor. From the maximum strain vs. pressure curves of the 50 and 100 um sensors (Fig. 2.6 (b)), the maximum strain on the Au thin film resistor are 0.78 % and 0.84 % at 28 mmHg and 35 mmHg respectively, which are very close to the strain value of 0.8 % causing possible failure in Au film (open circuit in Au film resistor). Different to the microcrack formation, the breaking induced by the strain lager than ~ 0.8 % is discontinuous and also non-conducting across the Au resistor. There is no Au residual layer existing at the breaking sites as in the micro-crack formation. The breaking first grows from the point with maximum strain and finally extends through the entire feature of the Au pattern over multiple pressure loading-unloading cycles, causing permanent failure of the sensor. Before the Au pattern completely breaks, the resistor is still conducting because the partial feature of the pattern is still continuous. It is so-called partial breaking.

Although for sensor operating at extreme high pressure region (maximum strain at the Au film strip lager than 0.8 %), it has a much higher sensitivity as shown in Fig. 2.9 (a), partially-broken Au pattern might not recover its initial electrical resistance when the pressure is released, which will result in sensing hysteresis. Moreover, the partial breaking might sharply reduce the fatigue life of the Au resistor because the breaking will gradually grow with the increasing number of loading-unloading cycles and eventually cause permanent sensor failure. Thus for stable and reproducible pressure sensing, the effective sensing range of our PDMS based pressure sensors of 50 um, 100 um and 200 um are determined to be 0 – 28 mmHg, 0 – 35 mmHg and 0 – 40 mmHg respectively.

C. Response time and sensing resolution

A faster response time of the pressure sensor is essential to obtain accurate real-time information about pressure. Figure 2.12 shows the response and relaxation times (rise and fall times, respectively) of the three sensors corresponding to the loading and unloading (pressure on and off, respectively). The response and relaxation time (time gap between 10 % and 90% of the steady state value at each pressure) of the 50 μm sensor, 100 μm sensor and 200 μm sensors were calculated and listed in Table 2.2. It should be noted that since the pressure was adjusted manually between 0 and 5 mmHg in the measurement, the response and relaxation times include the response times for the human hand, and thus represent upper limit for the sensor response times. Nonetheless, these response times are still 1 – 3 orders of magnitude better than previous sensors. [15, 17, 54]

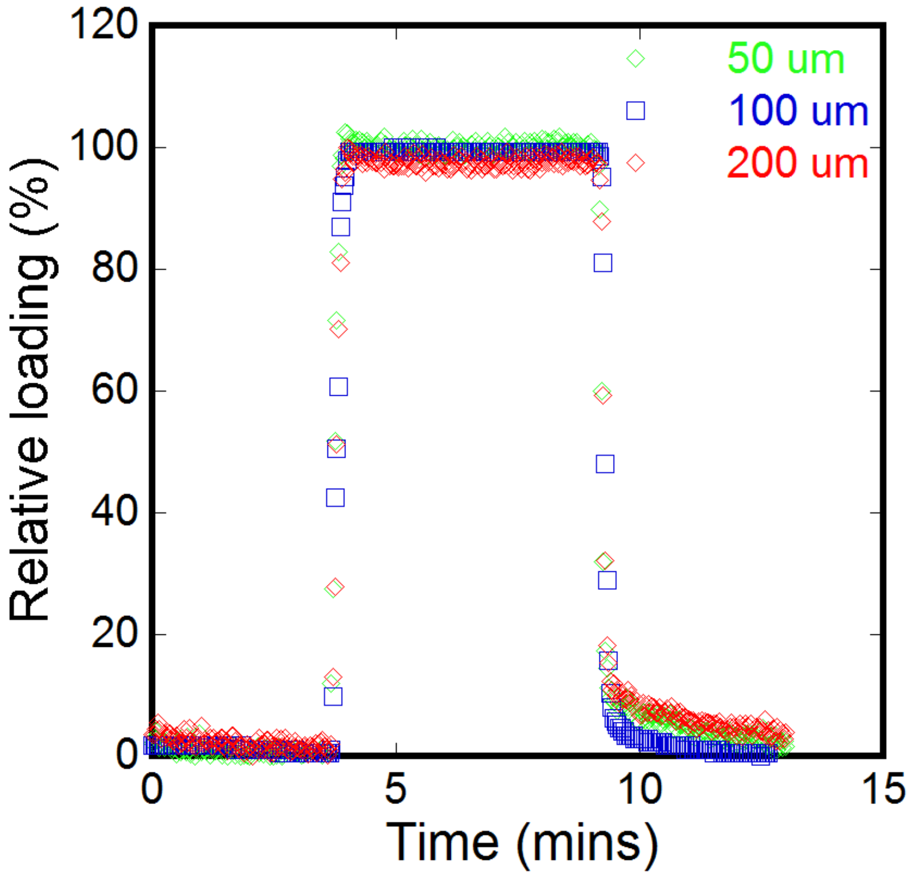

Figure 2.12 Sensor responses of the 50, 100 and 200 um sensors in a single loading and unloading cycle between 0 and 5 mmHg pressures. Relative loading of 0 and 100 % correspond to 0 and 5 mmHg pressures respectively.

In addition, we also measured the overall sensor resistance noise. Figure 2.13 shows the resistance root mean square (RMS) noise of the 200 μm sensor at different applied pressures which can be seen to remain fairly constant with pressure. The RMS noise at 0 mmHg for the three sensors are calculated and presented in Table 2.2. The best RMS noise limited resolution was found to be 0.07 mmHg (~ 9 Pa), which is much better than the desired value, 0.3 mmHg [55] (~ 40 Pa) typically required for blood pressure monitoring and higher than those of the pressure sensing elements reported recently for bio-implantable and artificial skin applications. [12, 41, 55]

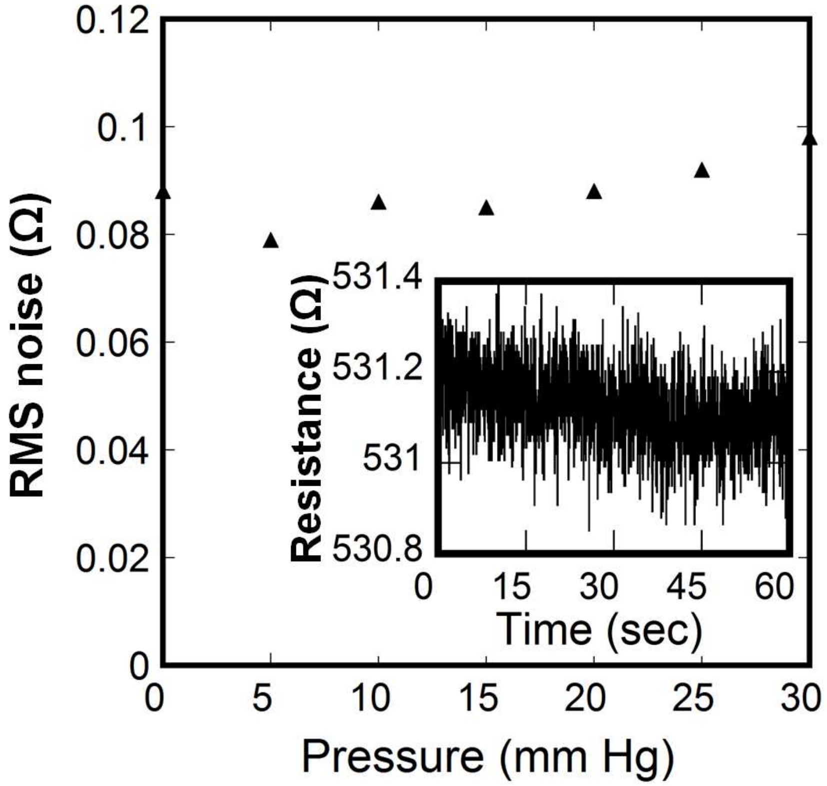

Figure 2.13 Variation of the RMS noise level of the 200 µm sensor with applied pressure. The inset shows the time-dependent resistance fluctuation at 0 mmHg pressure, which was used in the RMS noise calculation.

CHAPTER 3

OXYGEN DETECTION USING INDIUM OXIDE THIN FILMS

3.1 Introduction

Oxygen sensors have found wide applications in diverse fields ranging from automotive industry [56-58], medical [59-61], and scientific explorations [62, 63]. Metal oxides, such as, In_2O_3, ZnO, SnO_2, and TiO_2 have been widely investigated over the past years as materials for developing gas sensors [64-67]. However, high operating temperature is necessary to optimize the performance (i.e. high sensitivity and selectivity) of these metal oxide based sensors, for detecting various gaseous analytes including O_2 [68-70]. In particular, In_2O_3 is a wide bandgap (~3.7 eV) semiconductor exhibiting n-type behavior in its non-stoichiometric form due to oxygen vacancy induced doping [71, 72]. Daniel Laser reported the observation of conductivity modulation in In_2O_3 thin film by oxygen pressure variation [73]. It was experimentally found that the oxygen sensitivity was largely dependent on the operating temperature and film thickness (grain size). High operating temperature, however, implies high power dissipation, which becomes a challenge for further using miniaturized low power gas sensors in practical handheld sensor systems.

Research efforts have been directed toward improving the sensitivity, in an effort to reduce the operating temperature of the metal oxide sensors, by controlling their structural [74-76] and doping properties [76, 77]. Chaabouni *et al.* investigated the oxygen sensing property of ZnO thin film, prepared by RF magnetron sputtering, and found that the microstructure of the as-deposited films, which is dependent on deposition parameters and substrate nature, had a large influence on its oxygen sensitivity [75]. Atkinson *et al.* [77] studied the effect of dopant and firing temperature on the oxygen sensitivity of SnO_2 film based device fabricated by screen printing technique. They reported that using catalyst metal dopant Pt and higher annealing temperature helped to improve the sensor response at room temperature. More recently, oxygen sensor based on platinum doped In_2O_3 nanocrystals was demonstrated to have a very high sensitivity at room temperature [76], producing 95% change in resistance in response to 20% O_2 which compares favorably to the sensitivity values reported elsewhere [75, 77-80]. The high sensitivity was attributed to the large surface to volume ratio of nanosized In_2O_3 particles (synthesized via a non-aqueous sol-gel method), and enhanced O_2 chemisorption using Pt dopant as a catalytic promoter.

Another interesting approach for modulating oxygen sensitivity of both semiconductor thin films and nanowires (NW) has been demonstrated by adjusting the vertical electrical field between two parallel metal plates [81], or underneath a gate terminal [82-84]. Volkenshtein [85] first proposed that chemisorption of gas molecules on semiconductors might be electrically controlled by electric field vertically oriented to semiconductor surface. This idea was later experimentally observed by Stuart *et al.* [81] on ZnO thin film (300~700 nm). By adjusting the strength and orientation of the electric field generated between two parallel field plates, oxygen chemisorption on ZnO surface, and consequently the sensitivity, was controlled. It was proposed that the electric field resulted in the variation of the surface electron density. More recently, Zhang *et al.* [82] reported oxygen sensitivity modulation of a back-gated SnO_2 nanowire (NW) field effect transistor using the gate terminal. They proposed that by adjusting the gate bias, the available electron density at the oxygen vacancy sites inside the NW was varied and thus oxygen adsorption and desorption could be electrically controlled.

In this work, we systematically studied the effect of oxygen sensitivity of In_2O_3 thin film at room temperature under different dc biasing and humidity conditions. A simple model has been proposed correlating the oxygen sensitivity with humidity and electrical bias.

3.2 Experimental details

3.2.1 Device fabrication

The In_2O_3 functionalization layer used for sensing was 1 μm thick film on Al_2O_3 ceramic substrate purchased from Thinfilms Inc., and was RF sputtered at a base pressure of 5×10^{-7} Torr using an In metal target and oxygen as precursors. The conductivity of the as-deposited film at RT was determined with standard transmission line measurement (TLM), which yielded a contact resistivity of 1.762×10^{-2} Ω cm^2 and a film conductivity of 7.58×10^{-2} S/cm [64]. By conventional photolithographic process, interdigitated finger pattern of Ti (5 nm)/Au (50 nm) was deposited on top of the In_2O_3 thin film (both finger width and spacing were 50 μm), as schematically illustrated in Figure 3.1 (a). The finger pattern was used to obtain lower resistance thus higher detection sensitivity to gas analytes.

3.2.2 Measurement setup

Measurements of conductivity changes of In_2O_3 thin films were conducted at room temperature and atmospheric pressure both inside and outside a glass test chamber. The experimental set up is shown schematically in Fig. 3.1 (a). By simply applying a dc

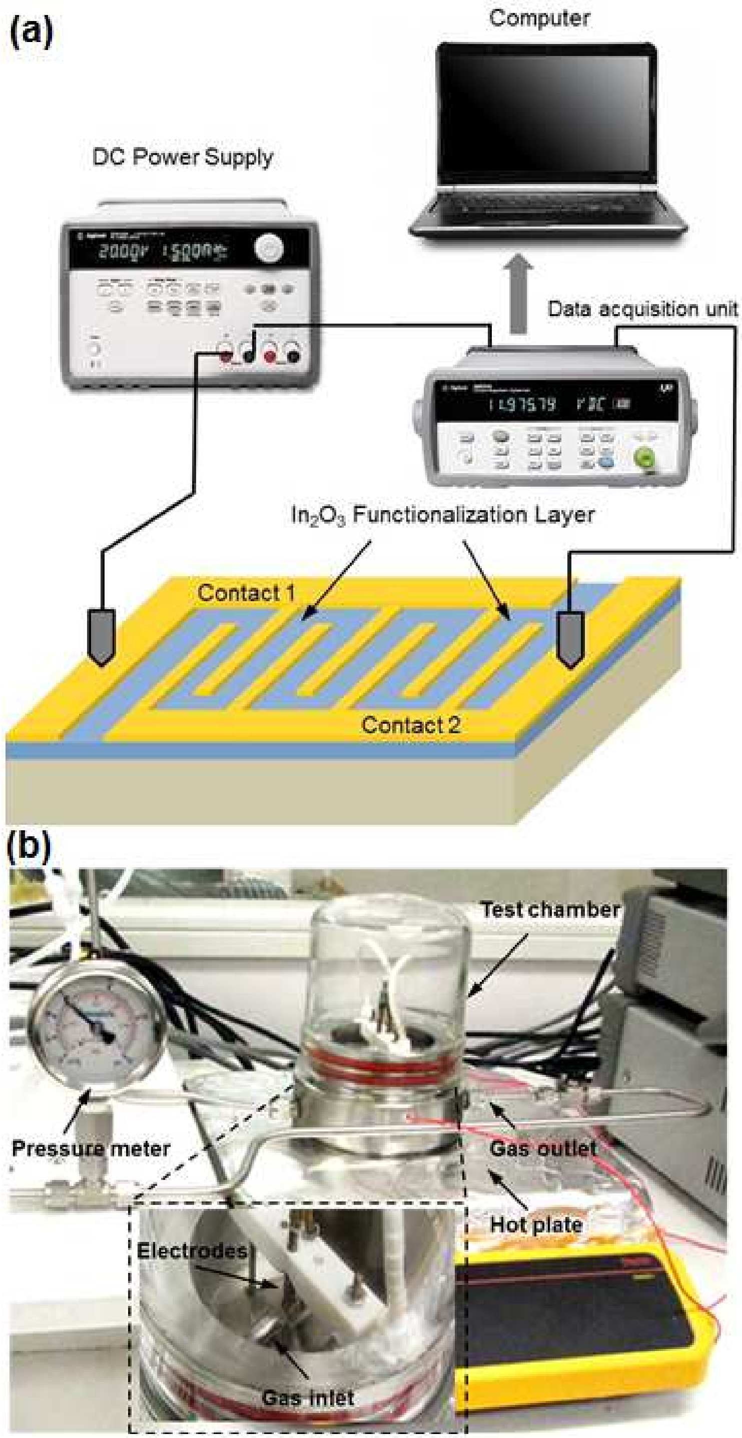

Figure 3.1: (a) Schematic diagram showing the sensor configuration for conductivity measurements. (b) A picture of the experimental set-up showing the test chamber as well as the gas inlet and outlet. The inset shows a magnified view of the test sample holder and the metal electrodes for biasing the sample.

bias across two metal contacts of the fabricated device, temporal current responses upon exposure to different gaseous analytes were recorded by a data acquisition unit (Agilent 34972A). To characterize the device in a well-controlled test environment as desired, it was mounted into a glass chamber of effective volume ~400 cm^3 and placed in close proximity to a gas flow fixture with a cross-section area of 0.5 cm^2, which enables us to quickly set the ambient condition of the sample to a desired O_2 concentration level (Fig. 3.1 (b)). A pair of spring loaded electrodes made the electrical connection between the device and the outside characterization equipment. Gaseous analytes (ultra-high purity O_2 and N_2) were purchased from Airgas, National Welders™. For the sensing experiment conducted inside the chamber, pure N_2 was used as gas carrier to mix with pure O_2 to obtain a desired O_2 concentration level at the gas inlet. Mass flow controllers (500 sccm Type 247, MKS Instruments) were used to control the flow rates and obtain desired composition of the analyte gas (O_2). To provide a moist environment for testing, dry N_2 was bubbled through a flask partially filled with deionized water (to produce N_2 saturated with water vapor at a given flow rate) before being combined with target gas analyte. The sensitivity (S) of the sensor is defined as percentage electrical conductivity change $\Delta\sigma/\sigma$, where σ is the initial conductivity at equilibrium and $\Delta\sigma$ the induced conductivity change due to changes in O_2 concentration.

3.3 Results and Discussion

3.3.1 Modulation of O_2 sensitivity in presence of moisture

We first examined the sensor response to O_2 outside the chamber in air. By flowing pure O_2 (250 sccm) over the sample, we observed ~40 % reduction in sample

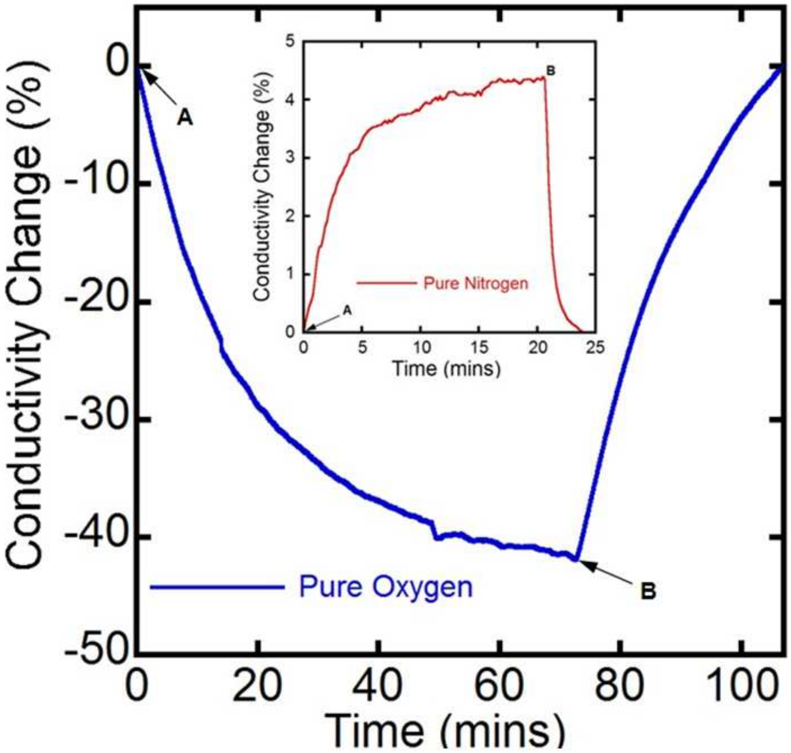

Figure 3.2: Sensor responses to flow of pure O_2 and pure N_2 (inset) in air under 10 V dc bias. The flow rate was 250 sccm for both gases. Points A and B indicate when gas flow was turned on and off, respectively.

conductivity as shown in Figure 3.2. For reference, the sensor response to pure N_2 was also examined and presented as an inset in Fig. 3.2. We find that the change is only ~4 %, and also in opposite direction, i.e. the conductivity increased instead of decreasing, unlike O_2. Both the magnitude and direction of the conductivity change supports the strong response of these films to changes in O_2 concentration, in agreement with earlier reports [73, 76]. Assuming that the ambient O_2 concentration is ~20%, flowing pure O_2 over the sample resulted in an 80% increase in O_2 concentration (led to a decrease in conductivity), while flow of pure N_2 resulted in 20% decrease in O_2 concentration (led to an increase in conductivity). Since the measurements were carried out in ambient conditions, adsorbed molecules e.g. water vapor [86, 87], can likely affect the sensing response. To investigate the possible effects of moisture, systematic sensing measurements were conducted in a closed test chamber, which allowed the test environment to be controlled as desired.

Before conducting the sensing experiments, the test chamber was first evacuated for 30 minutes. Afterwards, a constant 50 sccm flow of dry N_2 was started into the chamber and kept on as the background carrier (and diluting) gas throughout the experiment. To test for oxygen sensitivity, O_2 concentration change of 80% in the test gas (mimicking the change in oxygen concentration in our experiment conducted in air) was produced by starting an additional 200 sccm flow of dry O_2 into the chamber. We observed similar conductivity modulation as in air, with the maximum conductivity change (decrease) of ~40% after switching off the O_2 flow, as shown in Figure 3.3. Thus, we confirmed that our In_2O_3 sample responded similarly to O_2 at RT, both in ambient and in a closed chamber. Previously reported results indicate that the conductivity modulation caused by change in O_2 concentration is mainly due to the chemisorption of O_2 molecules on the In_2O_3 thin film [73, 76]. Due to the polycrystalline and porous nature of the In_2O_3 thin film, as evident from the scanning electron micrograph shown in Figure 3.4, this chemisorption can occur efficiently at various sites of the structure including the surface of individual grains, grain boundaries and metal-semiconductor contact interface [88]. Indium oxide in its non-stoichiometric form is an n-type semiconductor with oxygen vacancies acting as donors. Upon adsorption of O_2, electrons transfer from In_2O_3 to the O_2 molecules reducing the conductivity of the thin film in the subsurface region, and simultaneously increasing the potential barrier for charge transport at grain boundaries [89] and metal-semiconductor interface similar to SnO_2 [90]. All these aspects are responsible for the experimentally observed decrease in electrical conductivity as discussed above (Fig. 3.2 and 3.3). Although the maximum conductivity change (decrease) observed in Fig. 3.2 and 3.3 are approximately the same, i.e. ~40%, the modulation rate are quite different, as evident from the inset of Fig 3.3 where they are compared together. It has been well documented in the literature that humidity has a significant effect on the conductivity of metal oxide films including In_2O_3 [86, 87, 91] and their O_2 sensing property

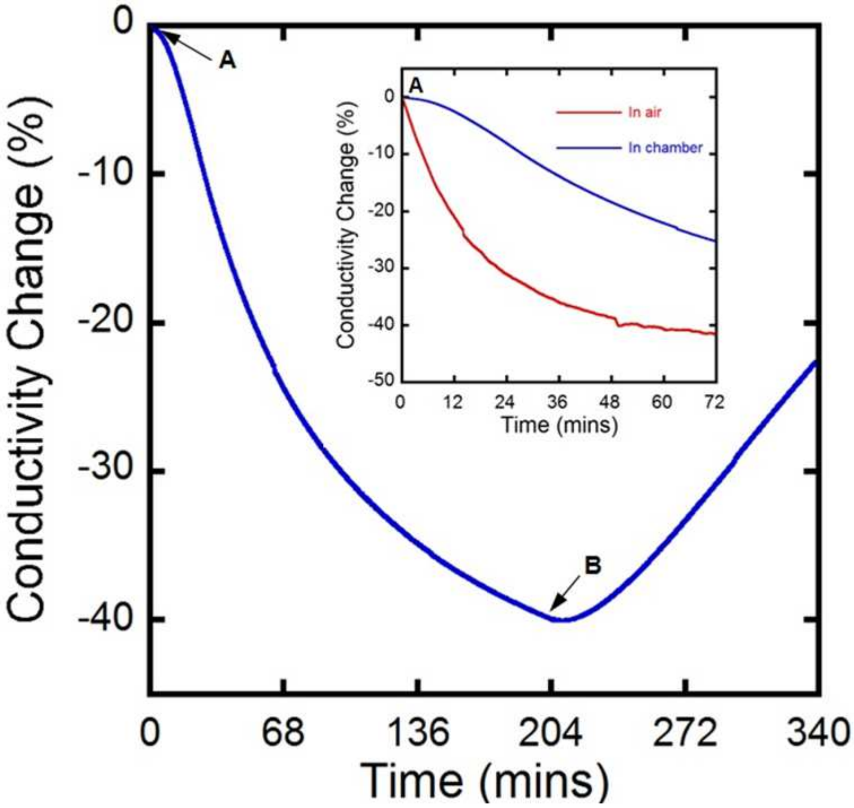

Figure 3.3: Sensor response to 80 % oxygen flow (200 sccm dry O_2 with 50 sccm dry N_2 as carrier) recorded in the test chamber with 10 V applied dc bias. Points A and B indicate when O_2 flow was turned on and off, respectively. The inset compares the sensor responses to the same O_2 concentration change (80%) in air and in chamber.

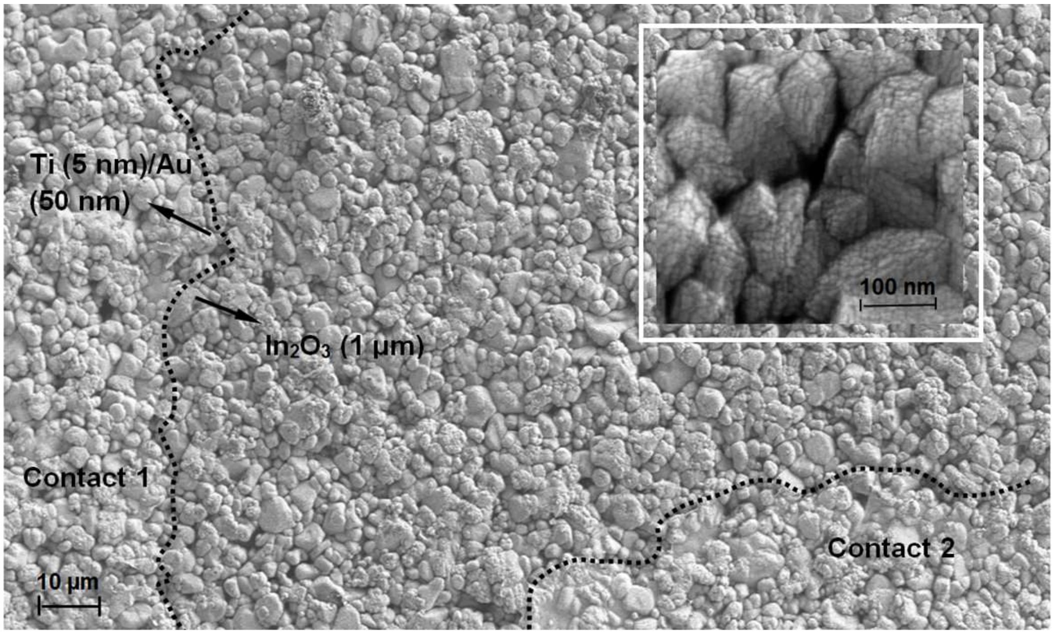

Figure 3.4: Scanning electron micrograph of a representative In_2O_3 thin film with thin metal contacts (Ti/Au) deposited on top. The inset shows a magnified image of the film from which its porous nature is evident.

[77, 92, 93]. Since moisture is present outside the chamber (in ambient), but absent inside, we conclude that moisture plays a significant role in affecting the sensor response to O_2.

To systematically investigate the effect of moisture on the O_2 sensitivity of the sensor, we performed a series of experiments inside the test chamber under a set of well-controlled conditions, with and without the presence of moisture. The sample was first placed in a moist environment with an initial flow of moist N_2 (50 sccm) as the background carrier gas. Then, to simulate a 50% change in O_2 concentration inside the chamber, an additional 50 sccm flow of dry O_2 was started. We observed a decrease in conductivity of the sensor (Figure 3.5), in agreement with our previous results, but at a much faster rate of ~40% within 13 minutes, compared to 210 minutes required to produce the same change, with dry N_2 as the carrier gas. In fact, this is even faster than the rate of conductivity variation in air caused by a change in O_2 concentration of 80%

(Fig. 3.3). Interestingly, the inset of Fig. 3.5 shows the response to flow of 50 sccm dry N_2 instead of O_2, where a decrease in conductivity of ~7% in 32 minutes is observe. The higher conductivity modulation rate with O_2 exposure in moist environment is most likely due to the enhanced oxygen adsorption caused by the additional n-type doping induced by moisture. On the other hand, the small conductivity decrease of the sample in response to N_2 exposure (inset of Fig. 3.5) can be attributed to the reduction in the amount of physisorbed water molecules on the surface of the sample. Both these mechanisms are discussed in detail later. Clearly, the above experimental results substantiate the influence of moisture on the O_2 sensitivity of the sensor. Since H_2O chemisorption would occur on In_2O_3 film surface when stored in ambient condition, and once chemisorbed, the molecules normally do not desorb easily at RT [86]. Even without introducing moisture in the test chamber, significant adsorbed water molecules are still expected to be present on the sample surface which can enable the fast sensor response to O_2 as observed in Fig. 3.3.

To verify that surface adsorbed moisture indeed played a role in oxygen sensitivity, we compared the sensor responses to the same percentage O_2 concentration change (50%) in both dry and moist conditions. The sample was first annealed in vacuum at ~200 °C for 2 hours to thermally desorb the H_2O molecules from the sample surface to a large extent. After vacuum annealing, the sample was exposed to 50 % O_2 concentration change (50 sccm dry O_2 with 50 sccm dry N_2 as the carrier gas). We again observed a decrease in the film conductivity, but with a much lower rate of decrease and extent as shown in Figure 3.6 (~15 % within 37 minutes as compared to ~60 % under

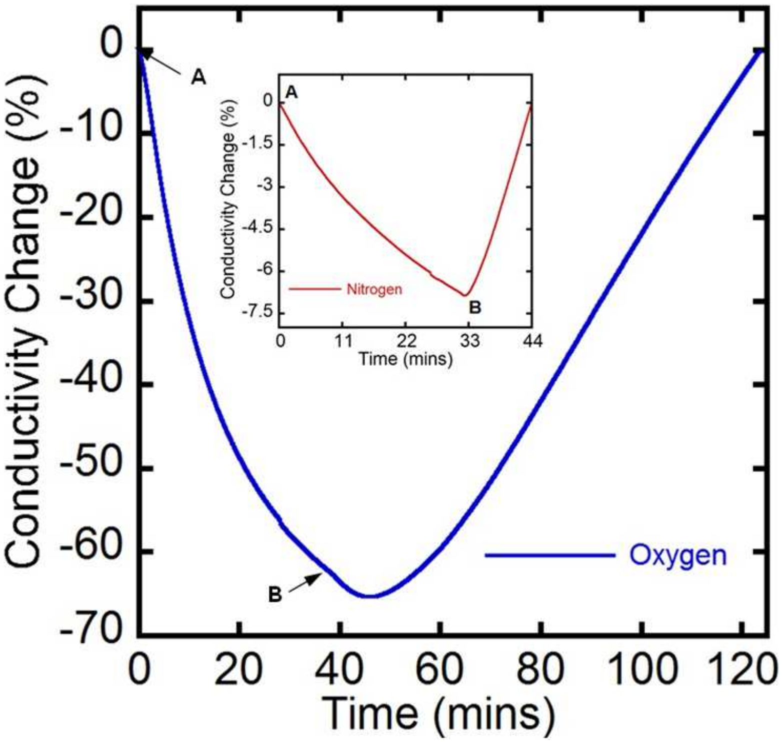

Figure 3.5: Temporal change in conductivity of the sensor upon exposure to 50 % O_2 in moist ambient condition (50 sccm dry O_2 with 50 sccm moist N_2 as carrier), under 10 V dc bias. As reference, the inset shows the sensor response to 50 sccm dry N_2 (moist N_2 was kept on as the background carrier). Points A and B indicate when dry O_2 (N_2) flow was turned on and off, respectively.

moist condition over the same duration). For comparison, we conducted the same experiment with additional 50 sccm dry N_2 flow instead of O_2, which did not result in any significant conductivity modulation (inset of Fig. 3.6). To explain the above observation on the modulation of oxygen sensitivity by the presence of moisture, we consider the chemisorption of the water molecules on the In_2O_3 surface. The chemisorption process is shown schematically in Figure 3.7 (a), where the adsorption of water molecules results in electron donation to the oxide film following a non-dissociative mechanism [92, 94], and causing an electron accumulation layer to form on the surface, which consequently enhances the sensitivity to oxygen. The band diagrams corresponding to initial state without any adsorption (assumed to be flatband condition), following water adsorption, and following oxygen adsorption are shown in Figs. 3.7 (b) – (d). Since electron donation to the In_2O_3 thin film occurs as a consequence of H_2O chemisorption and oxygen molecules accept electrons, the sensitivity to oxygen increases very significantly in presence of moisture, as directly observed in our experiments.

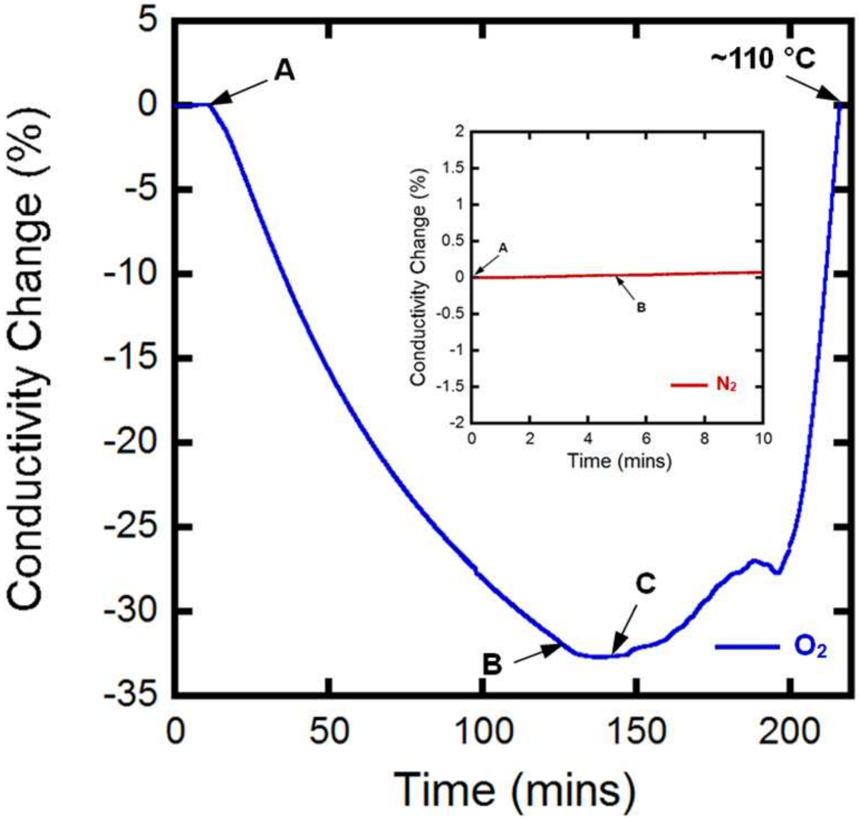

Figure 3.6: Temporal change in conductivity of the sensor upon exposure to 50 % O_2 in dry ambient condition (50 sccm dry O_2 with 50 sccm dry N_2, which was kept on as background carrier), under 10 V dc bias. Points A and B indicate when O_2 (N_2) flow was turned on and off, respectively. Sensor temperature was slowly increased starting from point C and reached ~110 °C when the conductivity of the sensor completely recovered. Inset shows the sensor response to 100 sccm dry N_2 flow (50 sccm additional N_2 flow over the background flow).

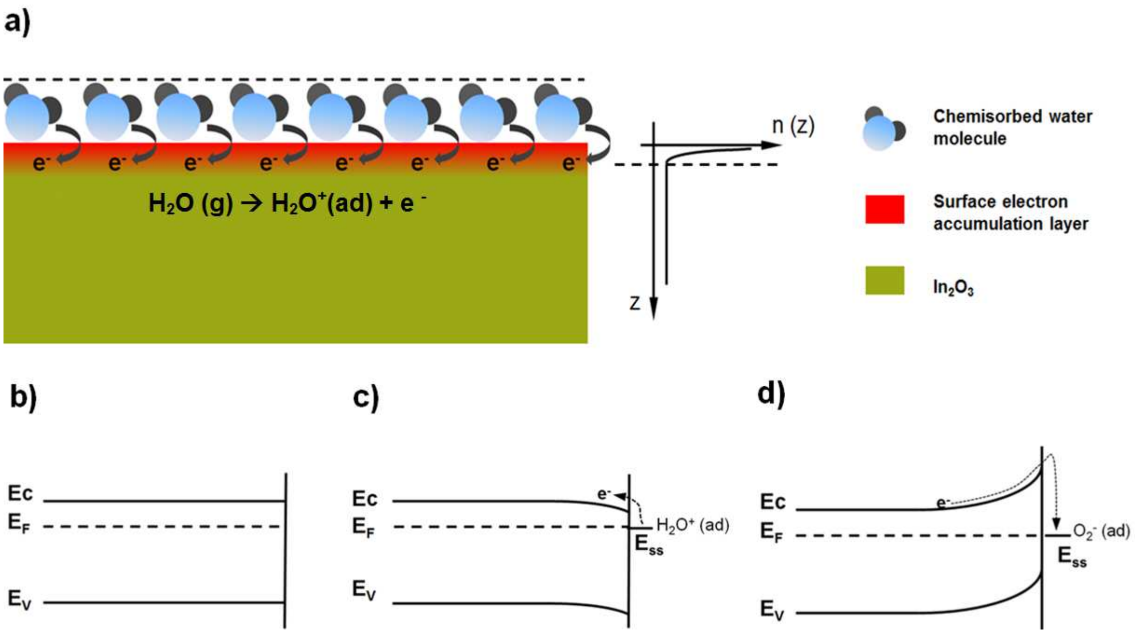

Figure 3.7: (a) Schematic diagram illustrating chemisorption of H_2O molecules on the In_2O_3 surface. (b), (c) and (d) Energy band diagrams before (b) and after chemisorption of charged H_2O (c) and O_2 (d) on the In_2O_3 surface. The charge exchange between the energy levels introduced by the adsorbed molecules, E_{ss}, and the conduction band are also shown.

In addition to chemisorption, physisorption of water molecules can also occur under high RH conditions, where water layers stack on one another and eventually form a liquid-like network [86, 91]. In this process, the film conductivity is increased, but this does not directly affect the oxygen sensitivity. This physisorbed layer also contributes to the increase in electrical conductivity by enhancing (i) the ionic conduction (proton hopping) between physisorbed water molecules on grain surfaces, and (ii) electrolytic conduction due to water condensation within capillary pores of the sensing material [95]. In our experiment, we have examined the influence of water adsorption on In_2O_3 thin film by monitoring the conductivity change when moisture was first introduced into the chamber. The sample was initially placed in a dry environment inside a chamber under a constant dry N_2 flow of 250 sccm, which was followed by exposure to moist N_2 of the same flow rate. Upon exposure to moisture, the sample conductivity rapidly increased ~20 fold and approached saturation within ~25 minutes, as shown in Figure 3.8. This clearly supports the above assertion that chemisorption and physisorption of water molecules on In_2O_3 surface significantly affects the film conductivity.

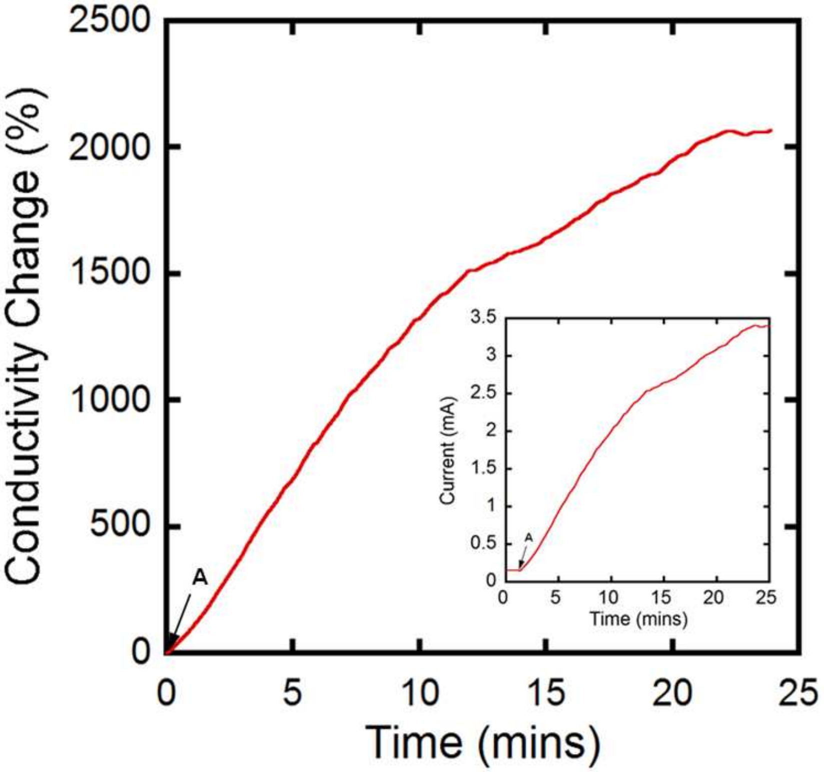

Figure 3.8: Temporal conductivity change of the sample when moisture (250 sccm moist N_2) was first introduced into the chamber. Point A indicates when dry N_2 flow (also 250 sccm) was turned off and moist N_2 turned on. The inset gives the equivalent temporal current change of the sample, originally recorded upon exposure to moisture, under 10 V dc bias.

The physisorbed H_2O can be easily and reversibly removed from the surface by decreasing the RH [86]. In fact, we observed that flow of a dry gas over the sample while its surface is still wet (physisorbed molecules present on the surface), can significantly change (reduce) the conductivity, as illustrated by the sensor response in the inset of Fig. 3.5. On the other hand, flow of dry N_2 did not cause any significant conductivity modulation (reduction), as expected, when the water completely desorbed from the sample surface after the sample was baked at high temperature (see inset of Fig. 3.6).

3.3.2 Oxygen sensitivity dependence on electrical bias

In addition to the presence of moisture, application of an electric field can also lead to an increase in sensor sensitivity [81-83]. To investigate any bias related enhancement in sensitivity for our In_2O_3 films, we conducted systematic O_2 sensing experiments in a dry environment under different applied dc biases. Similar to the moisture related sensing experiments described above, a background flow of dry N_2 at 50 sccm was maintained throughout these experiments. For different dc biases, the device was exposed to 50% dry O_2 (50 sccm pure O_2 flown in addition to the 50 sccm N_2 carrier gas) for ~5 minutes, and the corresponding conductivity modulation was recorded. Afterwards, the O_2 flow was switched off, and the chamber was filled with dry N_2. In between each applied bias, the chamber was kept in evacuated condition for 20 mins to clean up residual gases. Figure 3.9 (a) and (b) show the percentage conductivity variation (for applied biases changing from 0.5 to 10 V) as a function of time as O_2 flow was switched on (the actual concentration of O_2 was 50% due to continuous background flow of 50 sccm dry N_2) and off. From Fig. 3.9 we find that the sensor response to 50% dry O_2 changes from 0.08 to 11.8% as the applied dc bias changes from 0.5 to 10 V (see inset of Fig. 3.10). Clearly, the percentage conductivity change increased at a much higher rate compared to the voltage change (superlinear behavior), indicating that the impact of O_2 exposure on conductivity is much higher at larger voltage biases. Figure 3.10 compares the equilibrium current measured in dry N_2 environment with the current values measured in 50% dry O_2 as a function of applied bias (data from the same experiment as discussed above). We find that the current-voltage relationship for dry N_2 is linear as expected, however, it deviates significantly from the linear behavior in presence of 50% dry O_2, underlining the strong influence of O_2 on conductivity at higher biases.

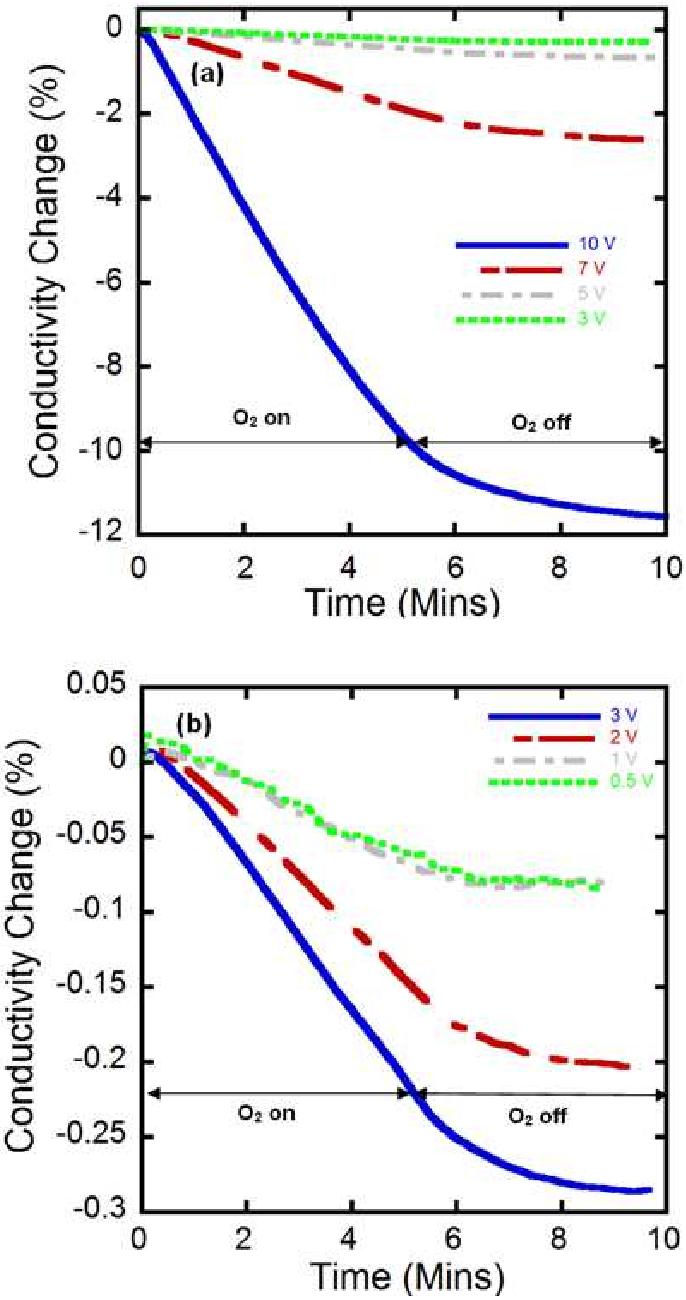

Figure 3.9: Sensor responses to 50 % dry O_2 flow (50 sccm dry O_2 with 50 sccm dry N_2 as carrier) recorded in the test chamber under larger (a) and smaller (b) range of dc bias.

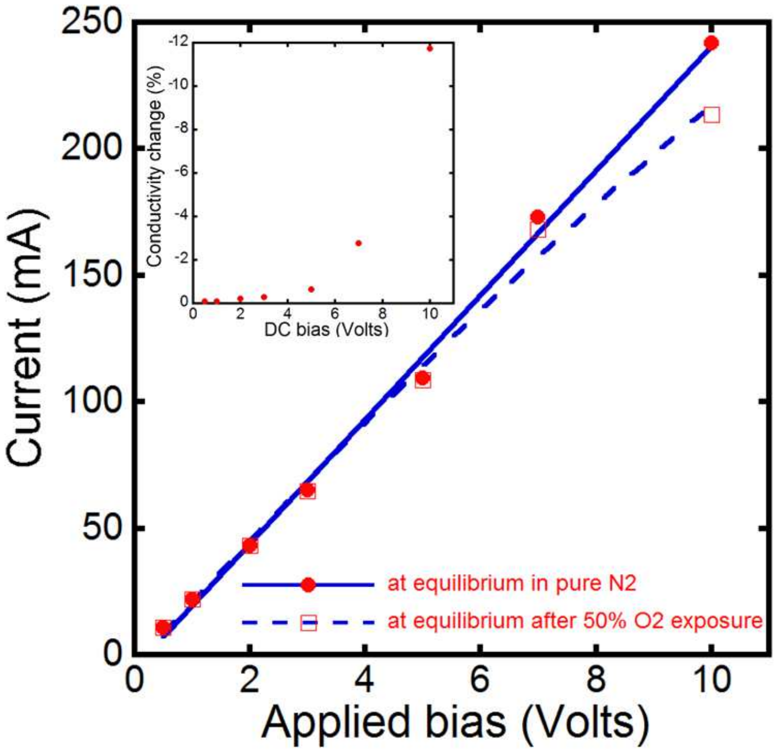

Figure 3.10: Equilibrium sensor **c**urrent versus applied dc bias. The solid line is the least square fit to the current data recoded in pure N_2 under different applied bias. The dashed line is a quadratic polynomial fit to the saturated current values recorded after exposing the device to 50 % O_2 for 5 mins. Inset shows the percentage conductivity change of the sample upon O_2 exposure with applied bias.

To further verify this trend, we directly measured the current-voltage characteristics of the sensor first in pure dry N_2 and then in 100% O_2, over a larger range of voltage, from 0 to 27 V. The results are shown in Figure 3.11(a). We find that the sensor current (in dry N_2) increases linearly with applied bias at lower magnitudes, as also seen in Fig. 3.10, but finally begins to saturate for dc bias >21 V. The sensor current after exposure to dry O_2 also followed a similar trend, although the current started to deviate from linear behavior at a much lower voltage (~7 V), as expected. The percentage conductivity changes with respect to voltage bias shown at the inset, which once again exhibits a superlinear behavior for dc bias <21 V, like that in Fig. 3.10. Overall, the sensor characteristics are similar to that of a field effect transistor (FET) at different gate biases. Typical drain current-drain voltage (I_d-V_d) family of curves at different gate voltages for AlGaN/GaN high electron mobility transistor or HEMT (a depletion mode device that is analogous to our sensor device where charge depletes due to O_2 adsorption) fabricated in our lab is shown in Fig. 3.11 (b), which is very similar to commonly reported I_d-V_d characteristics of depletion mode FETs in the literature [96, 97]. It is easy to see that the I_d-V_d characteristics corresponding to two different gate voltages in Fig. 3.11 (b) is very similar to the characteristic under pure N_2 and that under 100% dry O_2. The later can actually be thought to correspond to the FET characteristics under zero gate voltage and a large negative gate voltage, respectively. Thus, the adsorbed oxygen molecules serve to "electrochemically" gate the sensor device, resulting in its higher sensing response at higher applied biases. The concentration of the oxygen is analogous to the magnitude of the reverse bias for an FET. It should be noted, however, that at very high applied voltages when both the responses saturate (corresponding to N_2 and 100% O_2), the sensitivity will also saturate. Such a saturating trend in percentage conductivity change can be seen in the inset of Fig. 3.11 (a), for larger voltage biases (>21 V). Since, higher applied voltage results in larger power dissipation, the optimized biasing point of these sensors should be chosen somewhere near the onset of saturation behavior, since higher biases would only increase power dissipation without significantly improving sensitivity.

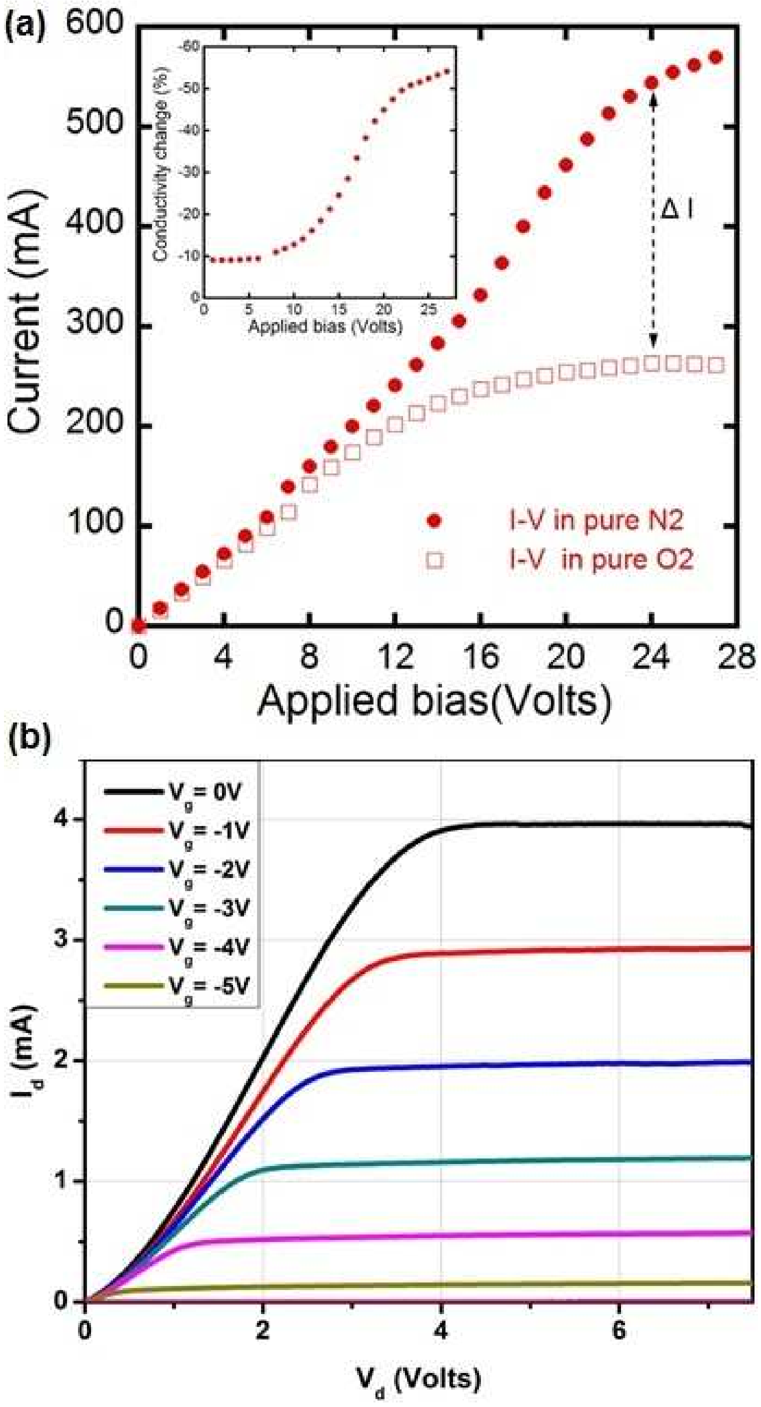

Figure 3.11: (a) Device I-V characteristic recorded in pure N_2 and O_2 ambient. Inset shows the percentage conductivity change of the device as a function of applied bias between pure N_2 and pure O_2 exposure conditions. (b) I_d-V_d characteristics of a representative AlGaN/GaN HEMT device fabricated in our lab.

CHAPTER 4

Design and Fabrication of Graphene based Ion Sensitive Field Effect Transistor

4.1 Introduction

4.1.1. Background and Significance

In a cell membrane (as illustrated in Figure 4.1), there are kinds of special proteins that can act as channels responsible for the electrical ion transportation. These channels are implicated in a wide range of pathological conditions such as epilepsy, cardiac arrhythmia, chronic pain, migraines, and type II diabetes. Thus they have become highly attractive therapeutic targets for drug discovery in pharmaceutical industry. As

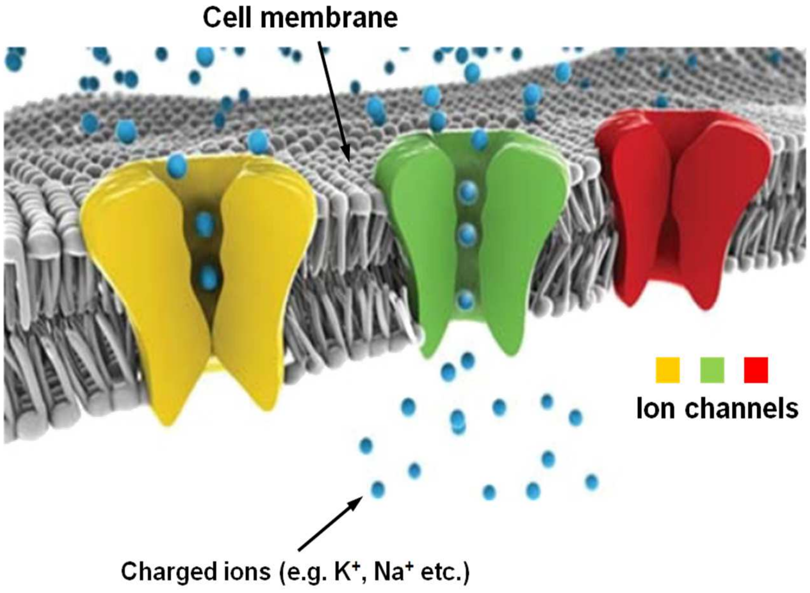

Figure 4.1: Illustration of ion channels in a cell membrane by J.P. Cartailler., Copyright 2007, Symmation LLC.

was reported, approximately 13% of the available drugs have their mechanism of action attributed to activity at various types of cell ion channels [98], representing a market value in excess of 12 billion [99]. The market value is keep climbing in these years and estimated to reach up to 21 billion by the year 2018. The primary force behind which are driving this market is the technological advancement in high throughput, cell based screening assays for efficiently identifying drug compounds serving as channel modulators in drug discovery procedure. Over the years, various ion channel screening assays have been developed including fluorescence, automated patch clamp system, and atomic absorption spectrometry. However, instrumentation for the automated analysis of ion channels in primary cells (cardiac myocytes & neurons) and stem cells is still lacking.

Ion sensitive field effect transistor (ISFET) [100] has a number of characteristics making it suitable for developing a novel ion channel screening assay. Unlike fluorescent indicators, ISFETs provide a label free direct measurement of ion efflux and are not subject to imaging artifacts. Because the detection can be performed without consuming extra reagent for labeling, it also largely increases system’s durability. In contrast to atomic absorption spectrometry (AAS), ISFETs can be fabricated for studying a large variety of ion channels and provide real-time acquisition and analysis capability. Its miniature size and large scale integrative capacity also enable us to integrate an array of ISFET sensors on a single chip for simultaneous ion efflux measurement from different cell ion channels. Moreover, ISFET based instruments could be utilized for screening primary and stem cells which are not compatible with fluorescence and automated patch clamp systems.

In this chapter, we presented the design and fabrication of a novel graphene based ion sensitive field effect transistor for real-time measuring K^+ efflux from living cells.

4.1.2. Ion sensitive field effect transistor: a brief review

ISFET, ion sensitive field effect transistor, was first introduced in 1970 by Dr. P. Bergveld from Spain [101]. It was initially developed and demonstrated for the measurement of ionic fluxes around a nerve [102] and later evolved into various related devices for other biological sensing applications. [103-107] Figure 4.2 (a) schematically illustrates the simplified device structure of a Silicon based ISFET. Similar to conventional field effect transistors (FETs) [108, 109], ISFET consist of three terminals called the “source (s)”, “drain (d)” and “gate (g)”. By controlling the gate voltage (electric field) via a reference electrode, we are able to control the channel conductance that is the current flow from drain to source electrode. For ion detection, the device is normally operated under a fixed electrical bias configuration as illustrated in Fig. 4.2 (b). A target ion concentration change in electrolyte instantaneously induces a surface

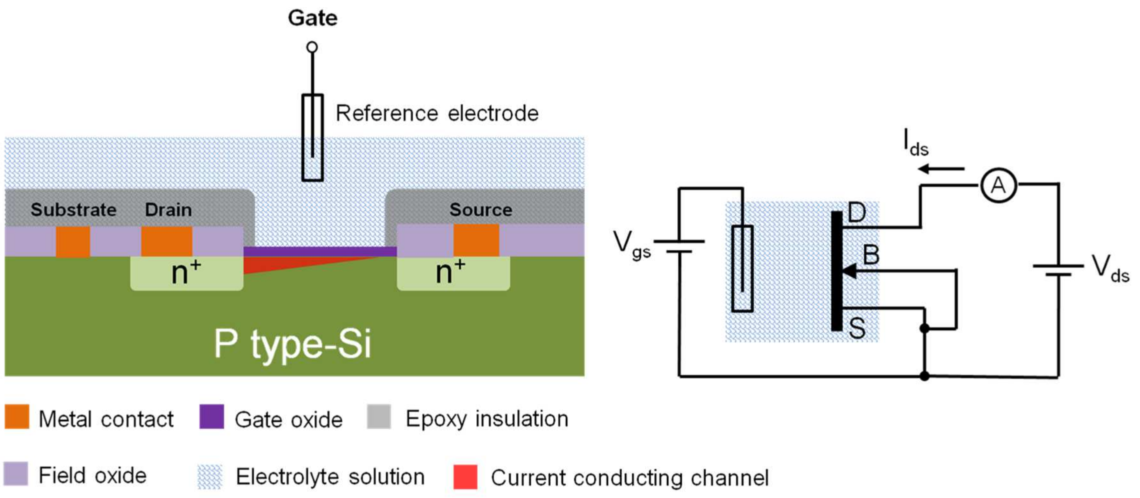

Figure 4.2: (a) General device structure of an n-channel Si based ISFET sensor. (b) Electrical biasing scheme for the sensor operation.

potential change at solution/oxide interface, which is further converted and amplified to an output current signal change, thus achieving the ion detection. The ion selectivity of the sensor device is achieved by incorporating an ion selective membrane (ISM), with either inorganic [110, 111] or organic [112, 113] nature, into the gate of the FET. The membrane can be either an additional oxide layer deposited on top of the gate dielectric or a polymer membrane drop casted/spin coated.

4.1.3. Limitations of state-of-the art Si based ISFET technology

Although Si based ISFETs have been well developed and tested, it has its own performance limitations including 1) the relatively low mobility value of Si (~450 cm^2/Vs) adopted in the state-of-the art ISFET development limits its sensitivity to ion concentration change. Figure 4.3 shows the typical I-V characteristics of a silicon ISFET in response to pH value in electrolyte solution. In practical measurement, the device is biased at the linear region of its transfer characteristic curve with maximum slope. When ion (hydrogen H^+ here) concentration changes in electrolyte solution, the threshold

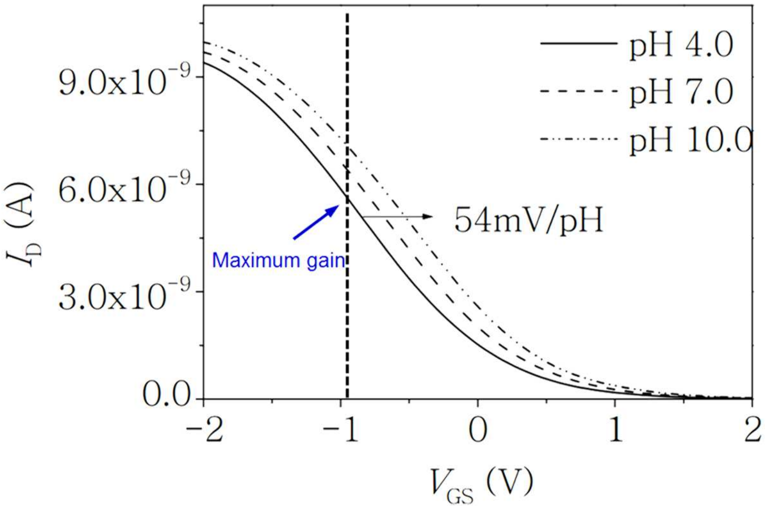

Figure 4.3: Current-voltage characteristics of a p-type Si ISFET in phosphate buffer solution with different pH values [114].

voltage of the FET shifts and in turn induces an instantaneous current response (electrical sensing signal). The slope of the curve, which is the FET transconductance g_m, determines the sensor sensitivity. Thus, the larger is carrier mobility of the selected material constructing the FET electrical conducting channel, the larger sensor response to ion concentration change will be; 2) Because of the poor stability of Si in aqueous solution, ISFET device normally require an additional oxide layer coated on top of the Si. This oxide layer boosts the stability of the device. However, over time this layer will trap ions in electrolyte that produce noisy interface thus degrade the sensing signal quality.

To overcome these limitations, we considered choosing graphene as an alternative material to develop a novel ISFET sensor with better sensor performance.

4.1.4. Graphene: an alternative material for biosensing applications

Graphene, recently discovered in 2004, has exceptional material properties [115] which are much superior compared to Si with respect to developing sensors for bio-detection applications. The ultra high carrier mobility over 10^5 $cm^2/V \cdot s$ demonstrated for graphene at room temperature [116], is orders of magnitude better than that of Si (~450 $cm^2/V \cdot s$), which is commonly used for bio-electronic applications at present [117]. Higher carrier mobility of an ISFET directly translates to higher sensitivity for ionic detection. In addition, the excellent chemical stability of graphene [118] enables us to use it as a sensing material in direct contact with surrounding harsh biological environment without additional oxide layer like in Si case. A much lower sensing degradation from graphene based ISFET can be expected. Moreover, graphene also exhibit very low thermal and 1/f noise, which indicate better sensing resolution [119]. In terms of biocompatibility, we have demonstrated direct cell growth on CVD (chemical vapor deposition) derived graphene

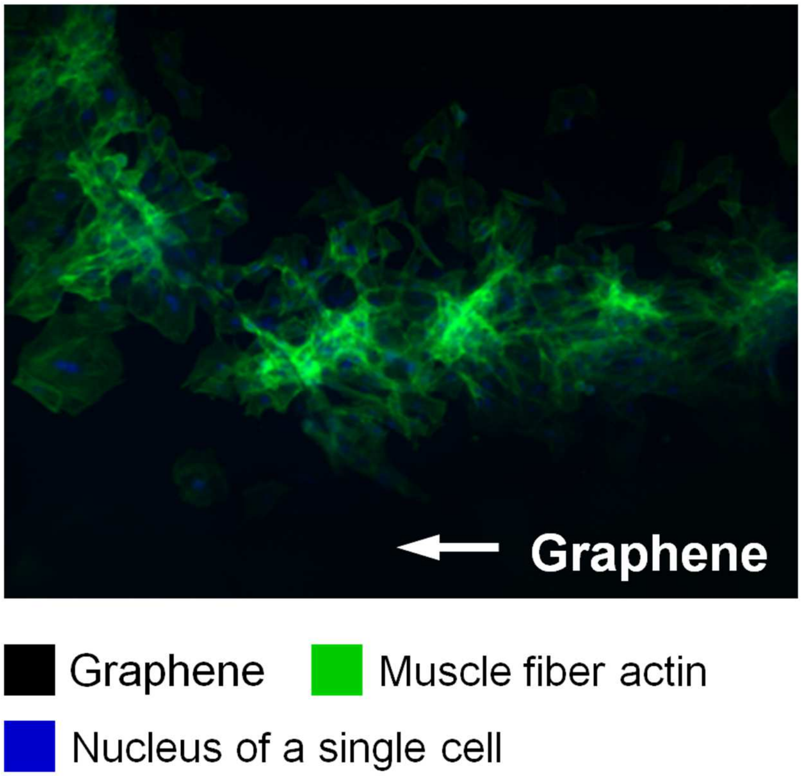

Figure 4.4: Florescent image of H9C1 cardiac muscle cells growing on graphene thin film CVD synthesized in our lab.

Figure 4.5: Optical image of the CVD system to be used for graphene synthesis in our lab.

thin film in our lab. As showed in the florescent image of Figure 4.4, H9C1 cardiac muscle cells were plated and growing well on the thin film, indicating very good biocompatibility of graphene. Finally, large scale graphene synthesis can be done inexpensively through chemical vapor deposition using a basic quartz tube furnace, as shown in Figure 4.5. All these properties are conducive for developing robust, low cost, and highly sensitive biosensors.

4.2 Sensor design and fabrication

4.2.1 Sensing mechanism

Similar to conventional silicon based ISFET, our graphene based ion sensor operates based on the change in electrical conductance of graphene thin film with the change in surrounding ion concentration. Figure 4.6 schematically illustrates the sensor structure and its operation principle. When graphene interacts with electrolyte solution, [120, 121] an electrical double layer will be formed at the graphene/solution interface (Fig. 4.6 (b)), which generates a potential drop between graphene and bulk solution. A change in surrounding ion concentration results in a change in the capacitance of the electrical double layer (C_{EDL}). Under a fixed bias configuration as shown in Fig. 1 (a), the capacitance change causes a subsequent change in the surface potential of graphene thin film, which induces a detectable current change in the conducting channel between drain and source electrodes (Fig. 1 (c)). Thus the transduction from an analog signal (ion concentration change) to an electrical signal (current change) is achieved.

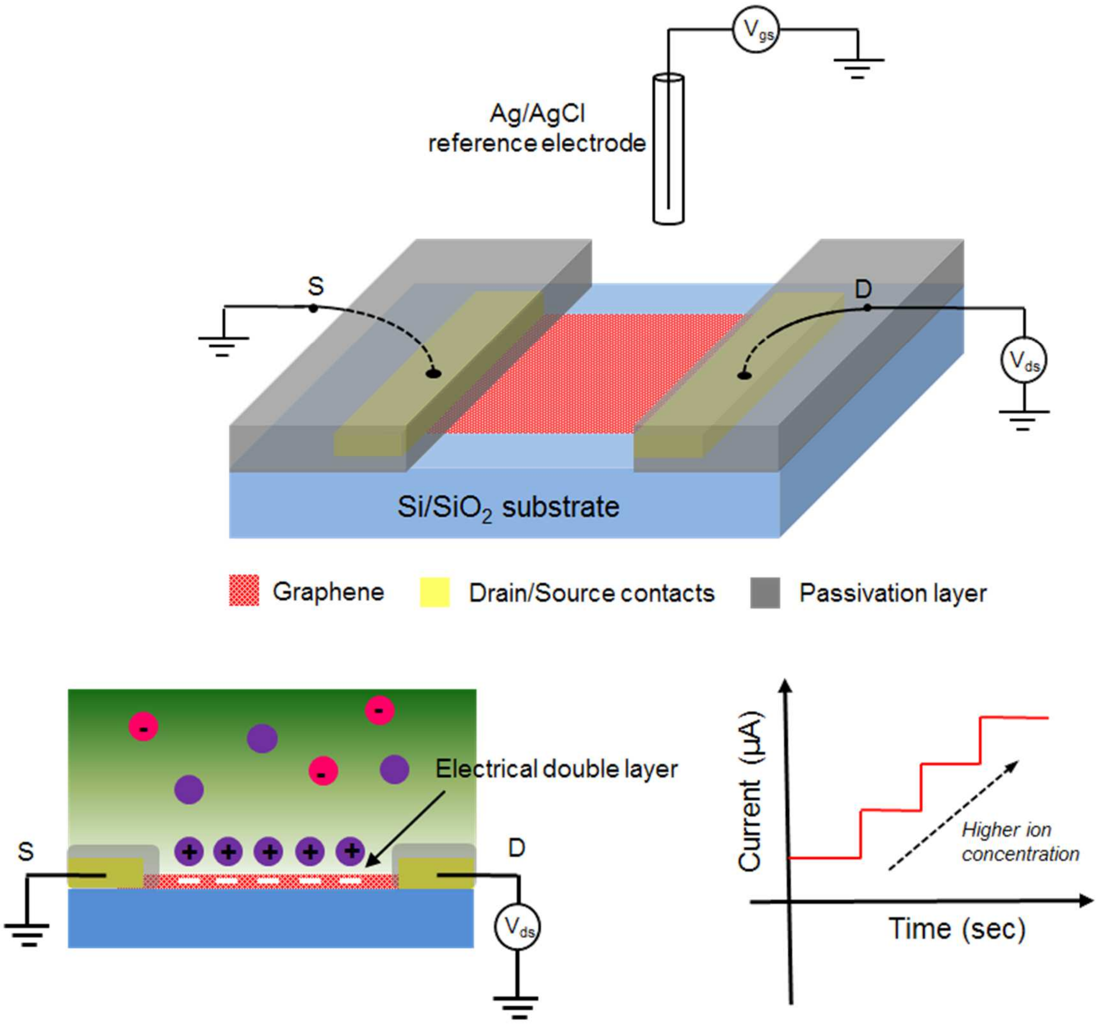

Figure 4.6: (a) Three dimensional schematic diagram of the graphene based ion sensitive field effect transistor (ISFET) including its bias configuration used in the electrical measurements. The ion sensor is inserted in an electrolyte solution (not shown in the figure) when it operates. (b) A schematic cross-section of the ISFET showing an electrical double layer forming at the graphene/solution interface. (c) Schematic illustrating real-time sensor amperometric response to ion concentration change

4.2.2 Device fabrication

In our sensor development, chemical vapor deposition (CVD) synthesized graphene on copper foil samples [122] were used to fabricate the graphene based ISFETs. The fabrication procedure is schematically illustrated in the flow chart of Figure 4.7, which involves three major steps: a) CVD synthesis of graphene; (b) graphene wet transfer; (c) ISFET sensor fabrication. Technical detail of each step is discussed in the following subsections.

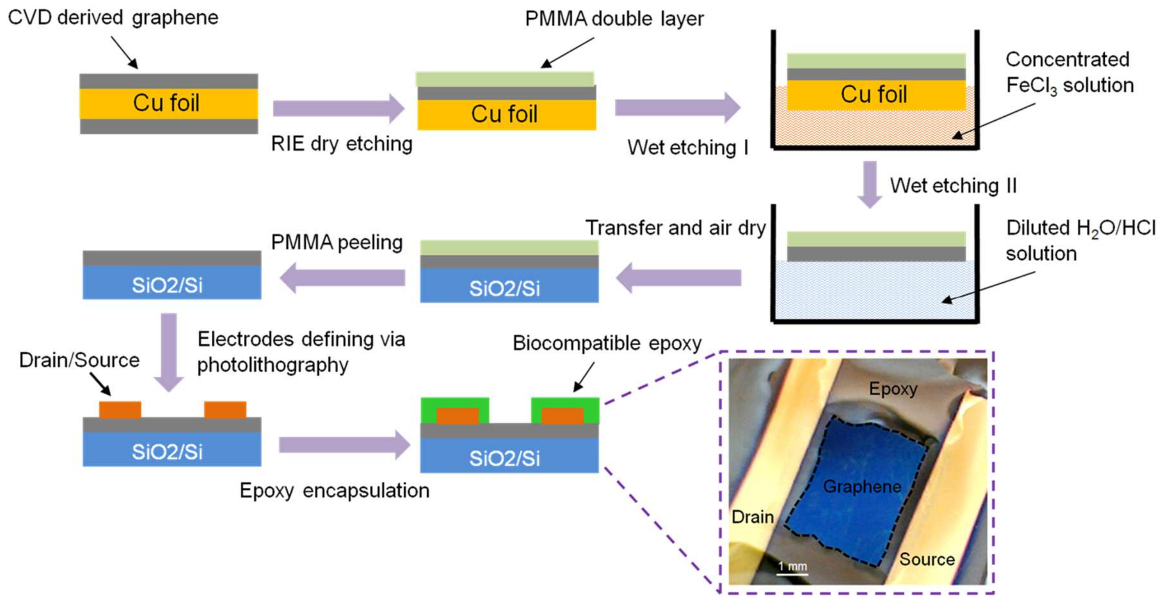

Figure 4.7: Fabrication process flow chart of the graphene based ISFET. Inset of the figure shows the optical image of a representative graphene based ion sensor encapsulated using biocompatible epoxy glue.

A. Chemical vapor deposition (CVD) of graphene on Cu foil

The graphene samples used in this dissertation was prepared (synthesized) via chemical vapor deposition in a home build quartz tube furnace (Fig. 4.5). The syntheses method was adopted from the earlier report [122] by A.K. Singh *et al*.

B. Graphene wet transfer

To start the transfer process, the graphene layer on the back side of the sample was removed by oxygen plasma etching (RIE dry etching) , which is followed by spin coating two layers of polymethyl-methacrylate (PMMA), to protect the graphene film at the front side during the subsequent wet transfer process. Next, a 5 ~ 6 hours Cu wet etching was performed in concentrated FeCl3 solution, leaving only the PMMA/graphene bi-layer floating on the solution surface. After rinsing in deionized water and diluted H_2O/HCl solution multiple times, the bi-layer was scooped out and placed on a SiO2/Si wafer substrate. The transferred sample was left for 24-hour air dry. Finally, acetone was used to dissolve and peel off the PMMA from the graphene surface, completing the transfer process.

C. Fabrication of graphene based ion sensitive field effect transistor

To fabricate ISFET, Cr (55 nm)/Au (70 nm) bi-layer was patterned on the graphene transferred on SiO_2/Si substrate via either shadow mask or standard photolithography technique, defining the drain/source contact electrodes. For the operation in an electrolyte environment, the wafer chip was mounted on a PCB board and wire bonded (not showed in the process flow chart here), after which a passivation layer utilizing either biocompatible epoxy glue or photoresist was deposited over the metal contact, SiO_2/Si chip and bonding wires, leaving an opening window on the graphene as the active sensing area (conducting channel of the ISFET) to be in contact with electrolyte solution. The inset of Figure 4.7 shows the optical image of a fabricated graphene based ISFET encapsulated by epoxy glue.

4.3 Sensor packaging

4.3.1 ISFET encapsulation using epoxy

The epoxy used to encapsulate ISFET sensors in this study was purchased from Epoxy Technology Inc. It is a biocompatible adhesive specially designed for medical electronics including USP Class VI and/or ISO-10993 compliance [123]. In this study, for the in-electrolyte solution chemical/biological sensing application, we evaluated the epoxy encapsulated ISFET sensors by electrical measurements and presented the experiment results in the following subsections.

A. Evaluation of electrical passivation

As an electronic based sensor device intended for operation in electrolyte solution, one of the primary concerns in our ISFET design is the proper electrical passivation. The purpose of using epoxy for sensor encapsulation here is to prevent high leakage current [124] occurring during sensor operation in testing solutions with high dielectric constant k, e.g. DI water ($k \sim 80$) and other common physiological buffer solutions like saline, Tris-Cl etc. Small leakage current (background noise) is essential for stable and reliable field-effect sensing. [125] We examined this point by studying the I-V characteristics of the epoxy coated graphene ISFET in electrolyte/physiological buffer solutions and summarized the characterization results in Figure 4.8. From the plot, we found that the current through the solution from the ISFET to the reference electrode (I_{gs}) was 2 ~ 3 orders of magnitude lower than the drain to source current (I_{ds}) in all the testing solutions. The small gate leakage current I_{gs} indicates negligible background electrochemical reactions between the graphene film/metal contacts and the electrolyte, which ensures the measured current change in I_{ds} mainly results from the conductance change in graphene channel not a spurious current. Based on the experiment results above, we concluded that the epoxy used here served well as a good electrical passivation material for our sensor packaging.

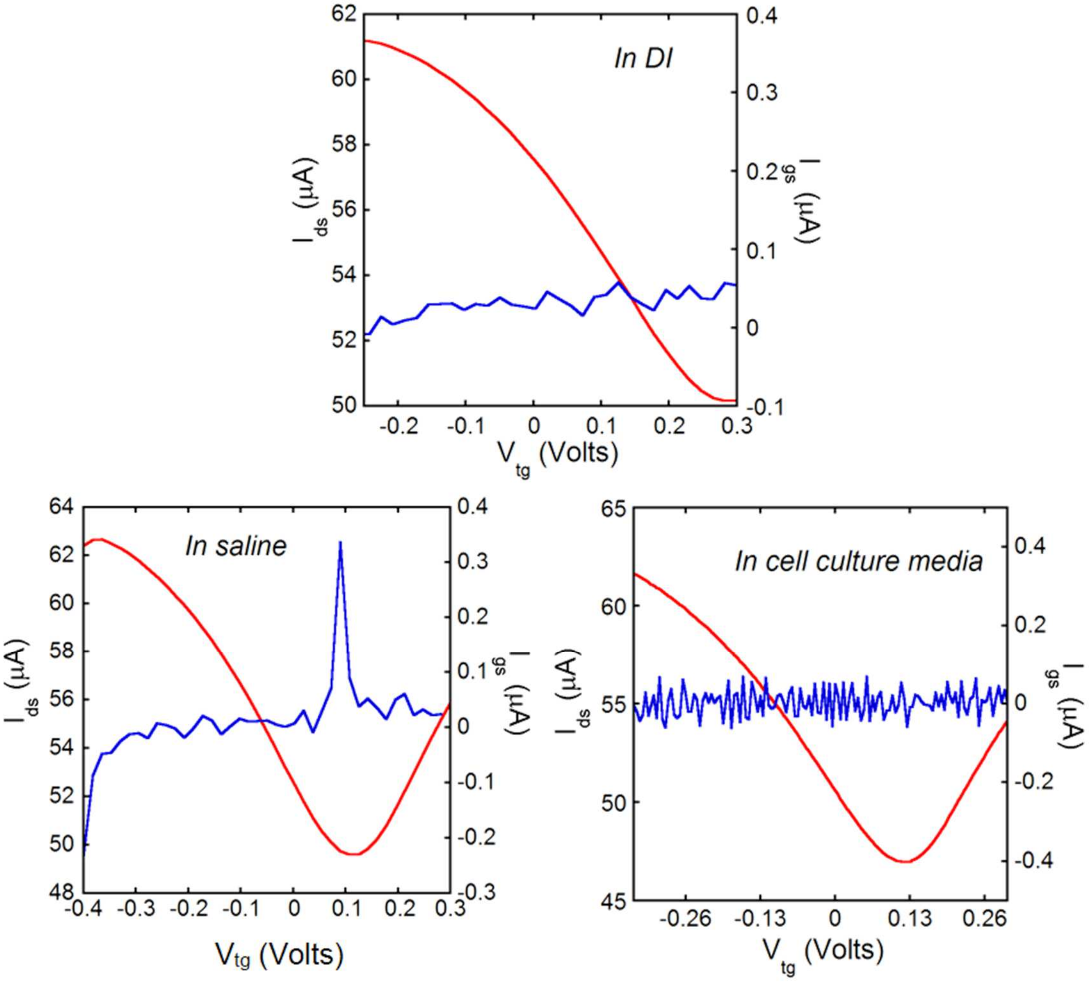

Figure 4.8: I-V characteristics of the epoxy encapsulated graphene ISFET in different testing solution from DI water, physiological buffer saline to cell culture media. Left axis: drain to source current I_{ds} vs. solution-gated voltage V_{tg} Right axis: gate leakage current $I_{gs.}$

B. Chemical stability and Biocompatibility

In addition to electrical insulation, we also examined chemical stability and biocompatible of the epoxy coated ISFET. Recently, graphene as an alternative biosensing material to Silicon has been insensitively investigated for its biocompatible and chemical stability. We studied the sensor degradation of our epoxy coated graphene ISFET by immersing the device in the cell culture media and tracking its I-V characteristics over a 24-hour time period. Figure 4.9 shows the device I-V characteristics in cell culture media taken at different time during the experiment. We found the I-V curves of the epoxy coated ISFET shifted slightly towards negative direction over time but seems to become stable after 16 hours. The shift in Dirac voltage of graphene [116] (electrolyte-solution gated voltage V_{tg} where the current I_{ds} reaches its minimum value) indicates carrier concentration modulation in the graphene conducting channel due to doping effect. This could be result from the adsorption of charged species in the media onto the graphene surface and consequent charge transfer between absorbents and graphene [126, 127]. More importantly, from the slope of the device transfer characteristics, we found the transconductance, i.e. ion sensitivity, of the ISFET remained almost the same over the 24-hour measurement time, which is essential for stable and reliable sensor performance. The results of the sensor degradation test above indicate good chemical stability of both graphene and the epoxy.

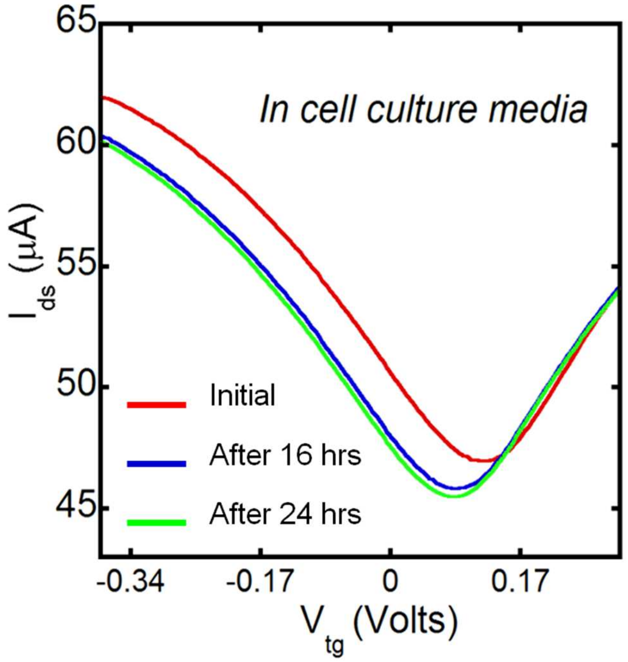

Figure 4.9: Sensor degradation test in cell culture media. Transfer characteristics of the epoxy coated ISFET were measured at different time points within 24 hours.

In addition to chemical stability, we also studied the biocompatible of the epoxy coated ISFET. By plating and culturing living cells (H9C1 cardiac muscle cells) directly on epoxy coated graphene (Figure. 4.10), we found cells are growing well not only on the graphene film (Fig. 4.10 c) but also at graphene/epoxy edges (Fig. 4.10 (a)), indicating excellent biocompatibility of both the CVD derived graphene and the epoxy glue.

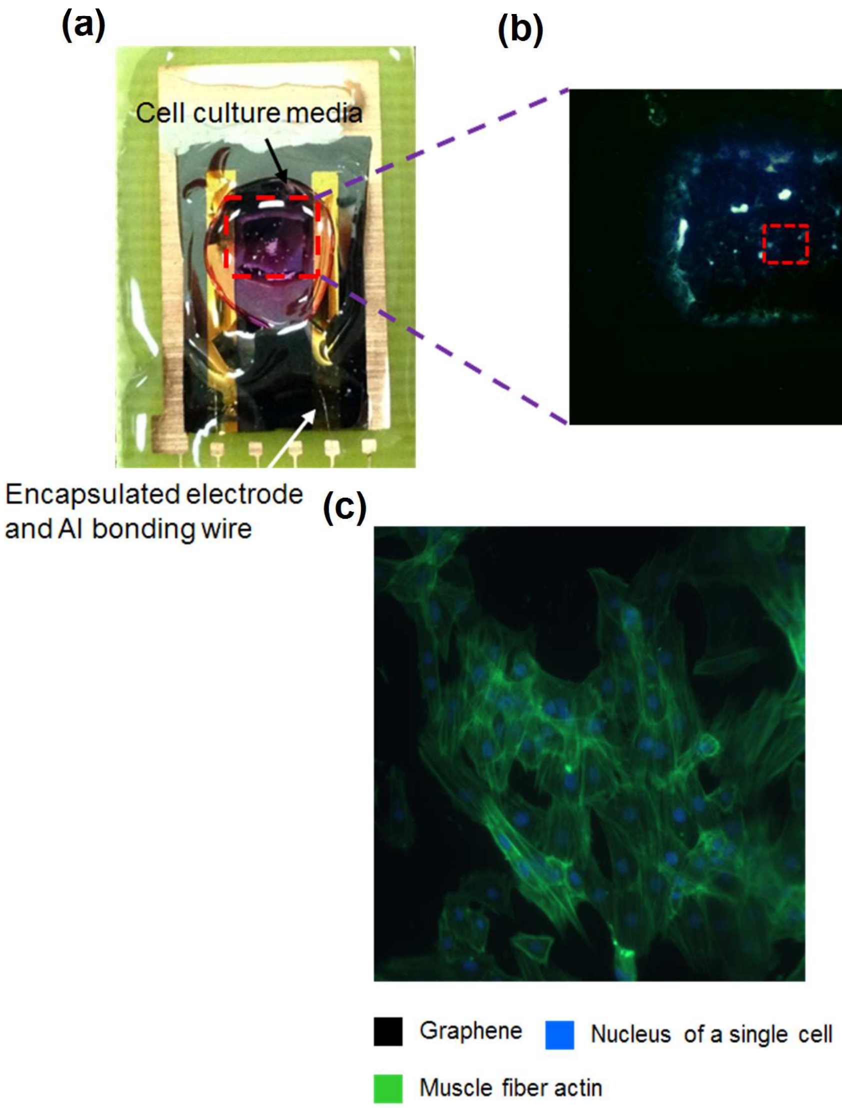

Figure 4.10: (a) Optical image of an epoxy coated graphene ISFET with H9C1 cardiac muscle cells directly plated and cultured on its active sensing area (indicated by the red dash frame in the figure). (b) Zoom-in view of the active sensing area defined by the epoxy. (c) Florescent image of the H9C1 cells growing on the graphene film.

C. Effect of epoxy on the electric transport properties of graphene

Apart from its good electrical insulation, excellent chemical stability and biocompatible, we noticed that the epoxy used for the ISFET sensor packaging seems to have a significant effect on the electrical properties of the sensing material, graphene. We conducted systematic investigation and reported our experimental findings below.

In the preliminary study, we examined the I-V characteristics of a back-gated graphene ISFET before and after epoxy encapsulation in air. Figure 4.11 (a) illustrates the device structure with its DC biasing scheme for electrical measurement. In contrast to top gate configuration discussed in Section 4.2.1, under back gate configuration [122], the channel conductance of graphene ISFET is modulated by the gate bias applied via a heavily doped Si substrate and SiO_2 layer serves as the gate dielectric layer in between graphene film and the substrate. The measured transfer characteristics are given in Fig. 4.11 (b). We observed a significant shift towards negative direction in device I-V curve with Dirac voltage shift of over 20 Volts. The shift in Dirac voltage indicates carrier concentration change in graphene film. Noticing the recent investigations reported on organic molecule doping of graphene [128, 129], we inferred that the carrier concentration change in graphene could be raised from the chemical doping from epoxy vapor to graphene film during epoxy curing process. However, as shown in the inset of Fig. 4.7, the interaction of epoxy with graphene not only occurs in ISFET conducting channel but might also at graphene/metal contact interfaces. To further investigate the effect of epoxy on the modulation of carrier concentration in graphene, we conducted separate experiments on epoxy free graphene FET devices as discussed below.

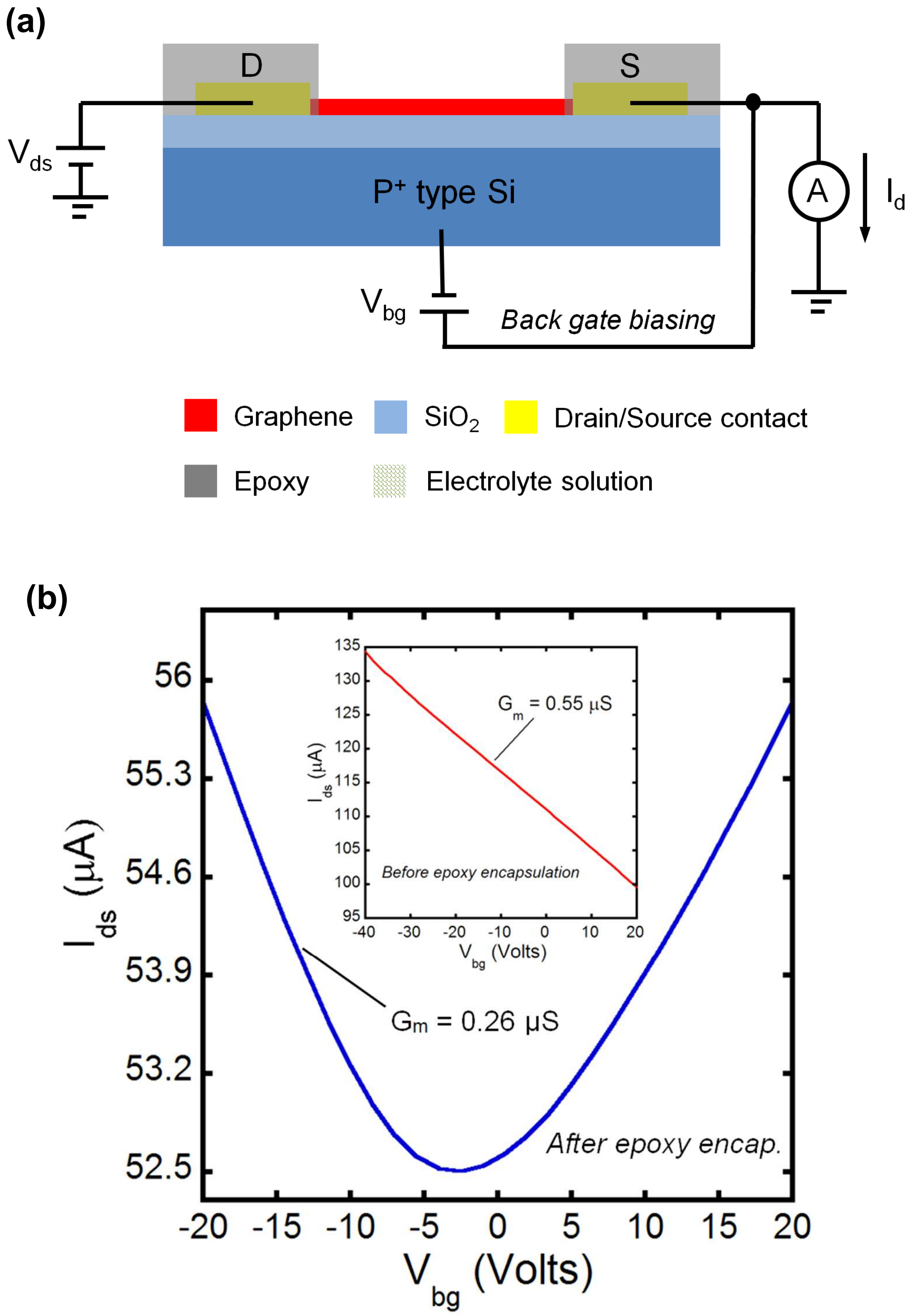

Figure 4.11: (a) Electrical biasing scheme of a back gate configured graphene ISFET. (b) Device transfer characteristics before and after epoxy encapsulation.

Figure 4.12 (a) shows the experiment setup. CVD derived graphene on Cu sample was transferred to a SiO_2/Si wafer chip (300 nm/ 500 μm) by the wet-etching method described before. Standard photolithography method was used to define the drain and source electrodes of the graphene FET. The chip was later mounted on a PCB board and wire bonded for electrical connection. Conductive Silver paste (SPI Supplies, Inc.) was used to make electrical connection between the Si substrate and the Cu pad underneath the chip, which serves as the gate electrode here. To begin with, we grounded both gate and source electrodes and applied a constant DC bias (1 V) across the drain and source electrodes. After a relative stable current level (I_{ds}) was reached, we deposit a small droplet of the epoxy glue on the graphene film but 2 ~ 3 mm away from the conducting channel (L = 1 mm and W = 4.5 mm). Upon the epoxy deposition, we observed a significant time-dependent current decrease as shown in Fig.4.12 (b). In addition, from the device I-V characteristics (inset of the figure) measured at different time points during the experiment, we found that the I-V curves were left shifted over time. Interestingly, the slope of the transfer characteristics of the graphene FET, which indicates the carrier mobility [122], seemed not being affected much by the epoxy deposition. To further understand, the time dependent effect of epoxy on the electric transport properties of graphene. We calculated the channel conductance (G), carrier mobility (μ_{FET}) and concentration (p) based on the measured transfer characteristics (at V_{ds} = 1 V and V_{bg} = 0 V) and listed them in Table 1. We found upon epoxy deposition, the field effect mobility of hole carriers increased, but its concentration decreased over time, which indicates n-type doping occurring in the graphene film. Since both the carrier mobility and concentration enter linearly into the graphene conductance. The current

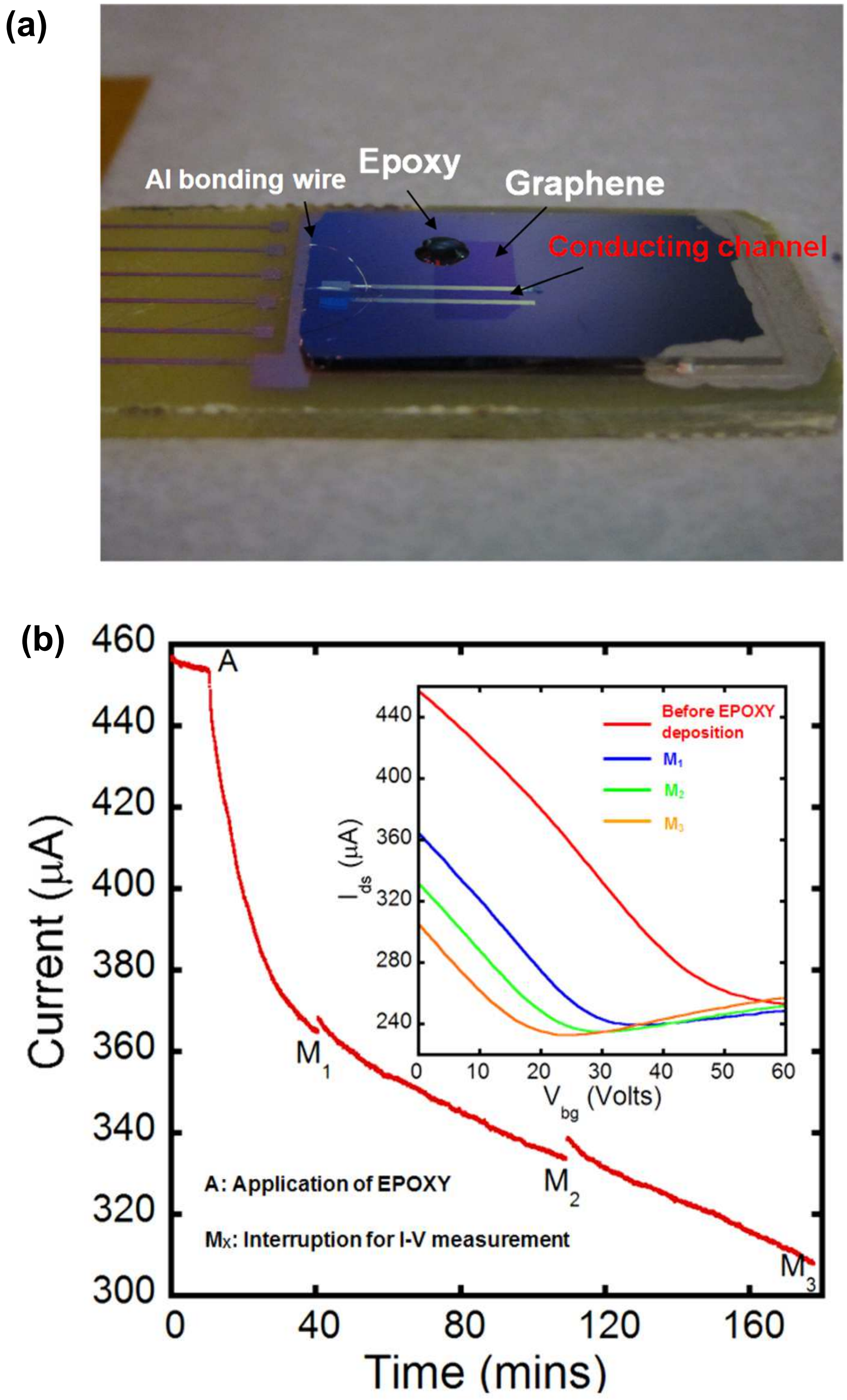

Figure 4.12: (a): Optical image of the experimental setup for the epoxy effect study. A droplet of uncured epoxy was deposited on the graphene 2~3 mm away from the conducting channel of a back gated graphene FET. (b): Time dependent current change upon epoxy deposition. Inset shows the device I-V characteristics taken at different time instants, M_x, during the temporal current measurement.

change observed from the time dependent measurement was dominated by the modulation of carrier concentration under the effect of epoxy.

Table 4.1: Electric transport parameters of graphene under the influence of epoxy.

Time after epoxy deposition (mins)	Current I_{ds} (μA)	Dirac voltage (Volts)	Channel conductance G (μS)	Carrier mobility μ (cm^2/vs)	Carrier concentration n(p) (10^{13} cm^{-2})
0	457	> 60	457	75	1.07
30	365	34	365	111	0.58
100	332	29	332	111	0.53
170	306	24	306	116	0.46

To further understand how the epoxy/graphene interaction affects the carrier concentration in graphene film and prove our hypothesis of epoxy vapor doping of graphene, we studied the effect of epoxy on back gated graphene FETs with smaller dimensions of L x W = 200 μm x 100 μm and L x W = 5 μm x 3 μm, respectively. To begin with, we deposited a droplet of epoxy on top of a microscopy cover glass and positioned the cover glass close to the devices under test in air. After 24-hour epoxy exposure, we measured the I-V characteristics of the graphene devices. We found significant negative shift (> 20 V) in I-V curves of the measured devices (n = 3). Figure 4.13 gives the transfer characteristics of a representative graphene back-gated FET before and after epoxy exposure (the red and the blue curves plotted in the figure, respectively). We found that the Dirac voltage of graphene shifted over 60 Volts. It is also worth to note that under the effect of the epoxy, the doping type of graphene changed from heavily doped P type (V_{dirac} > 60 V before exposure) to slightly doped n type (V_{dirac} ~ -4 V after exposure). The experiment results above further support our argument of possible chemical doping of graphene by epoxy vapor. To eliminate possible long-term influence of environmental factors in air (e.g. temperature, moisture and other gaseous species) on graphene, we positioned the wafer chip close to the liquid surface of bulk epoxy curing agent for 5 mins and measured the I-V characteristic of the same device (as plotted by the blue green curve in Fig. 4.13). As expected, the I-V curve shifted further to the negative direction, but surprisingly with the Dirac point shift of ~ 60 V in just 5 mins exposure time. From the material safety data sheet (MSDS) [130] of the epoxy released by Epoxy technology, Inc., we noticed that the curing agent consists of several organic ingredients including 2,2,4-Trimethyl, 6-hexanediamine ($C_9H_{22}N_2$).

Based on the investigation conducted so far, we concluded that the epoxy used for ISFET encapsulation here has a strong n-type doing effect on graphene, which might be

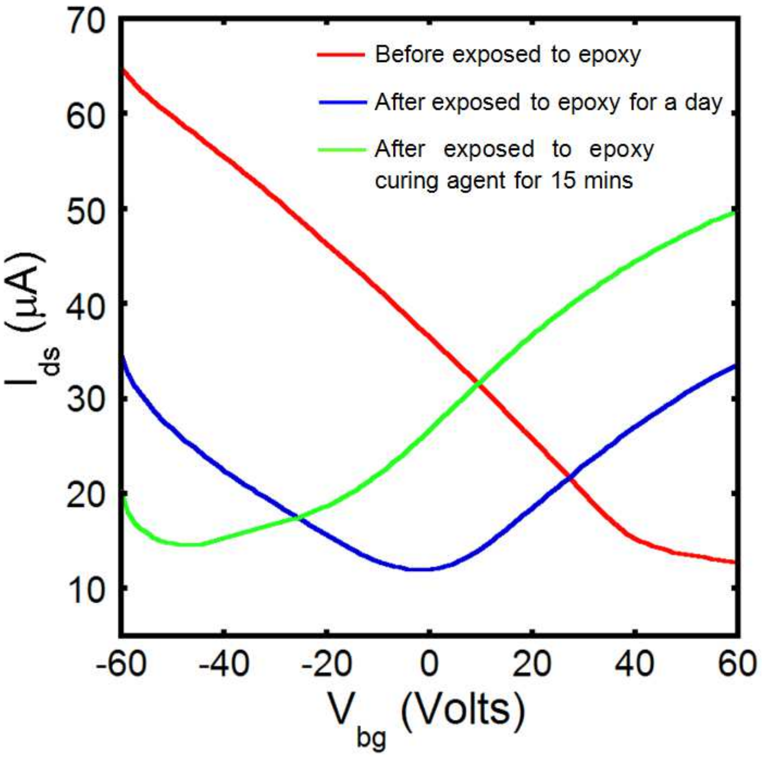

Figure 4.13: I-V characteristics of a back-gated graphene FET (L x W = 200 μm x 100 μm) before and after epoxy/epoxy curing agent exposure.

result from the organic ingredients (e.g. $C_9H_{22}N_2$) in its curing agent. The experiment findings might lead to a new approach of organic molecule doping of graphene. On the other hand, epoxy might also change the contact resistance between graphene and metal electrodes, which results in transconductance degradation of the epoxy coated ISFETs as observed in Fig. 4.11

4.3.2 ISFET encapsulation using photoresist

As the encapsulation material for our ISFET sensor, epoxy has been proved to be a good electrical passivation material with properties of good chemical stability and excellent biocompatibility. However, electrical measurements conducted with epoxy encapsulated graphene ISFET have revealed that epoxy has significant effect on the electrical transport properties of graphene and more importantly the transconductance of the ISFET, which directly determines the sensitivity of the ion sensor, degrades during sensor encapsulation. On the other side, because of scalability issue with graphene [131], further device miniaturization on graphene ISFET is needed for better electronic performance (much higher carrier mobility), thus optimized sensor performance (e.g. ion sensitivity). Smaller device dimension will also allow us to realize high pixel integration of an array of ISFETs on a single wafer chip to detect different ions in biological system or use the ISFET sensor in other biomedical applications including bio-implantable devices. Because of its intrinsic material property, epoxy is not process-compatible with the state-of-art micro/nano-lithography techniques. With the epoxy glue, we are not able to pattern the active area in graphene with well controlled dimensions. Thus we considered to use alternative material for the sensor encapsulation.

Of the biocompatible material for sensor packaging applications, epoxy based photoresist, e.g. SU-8 [132, 133], has emerged as the material of choice for biosensor development due to its well-known biocompatibility, high stability to chemical and radiation damage, easy to process wafer-level capability and low cost. To prove the feasibility of using photoresist for our ISFET packaging, we used positive photoresist (PR), S1811 as an alternative encapsulation material to the commercial epoxy glue in the preliminary study. Figure 4.14 shows the optical image of three parallel ISFETs fabricated on a single graphene film using photoresist for the sensor encapsulation.

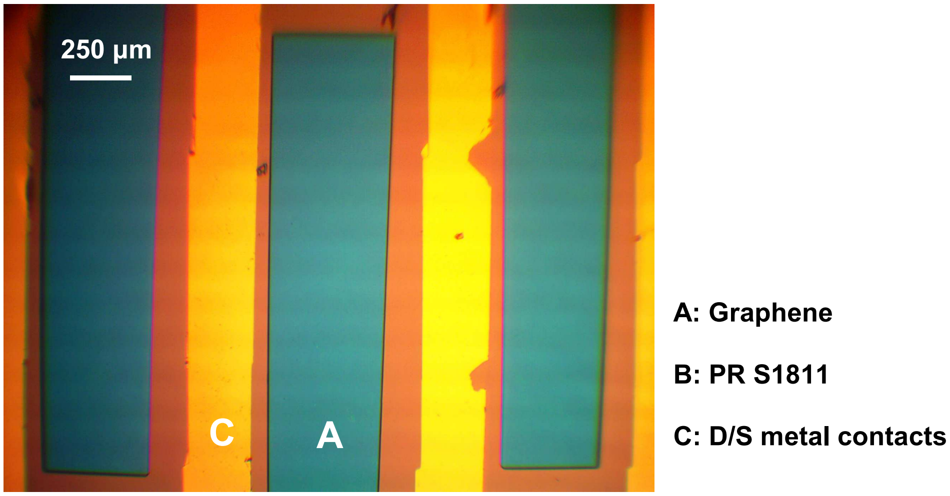

Figure 4.14: Optical image of an array of three ISFETs fabricated on a single graphene film. Photoresist, S1811 was used to passivate the drain/source electrodes. The metal contacts and the active sensing areas on graphene with channel L ~ 0.45 mm and W ~ 2 mm were defined by standard photolithography.

CHAPTER 5

ELECTRICAL CHARACTERIZATION OF ION SENSITIVE FIELD EFFECT TRANSISTOR

5.1 I-V and C-V characterization of graphene ISFET

5.1.1. I-V characteristics in electrolyte solution

With the fabricated prototype devices, we systematically studied their I-V and C-V characteristics respectively in electrolyte solution. The experimental setup is schematically illustrated in Figure 5.1. In I-V measurement, DC bias of V_{ds} and V_{gs} were supplied by a precision source/measurement unit (SMU, Agilent B2900A). I_{ds} and I_{gs} (current flowing from source to drain and from gate to source electrodes) were

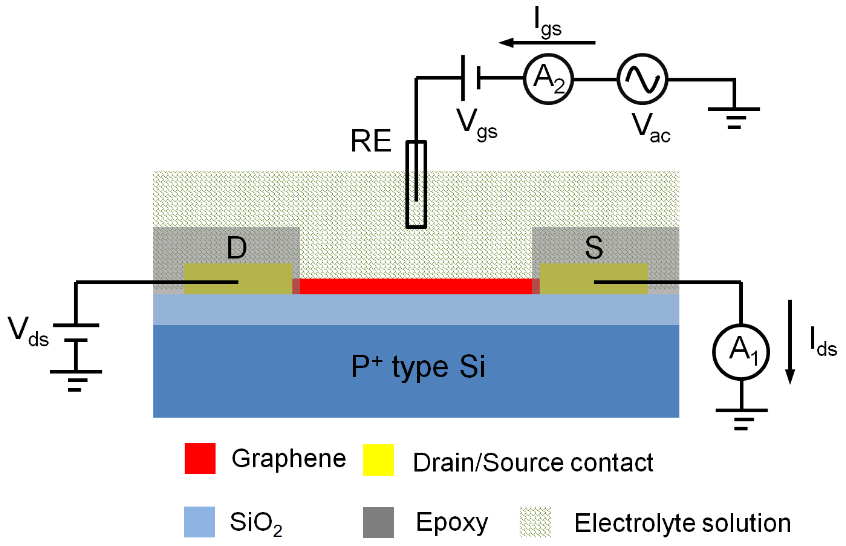

Figure 5.1: Schematic diagram of the experimental setup for sensor electrical (I-V and C-V) characterization.

simultaneously measured. In C-V measurement, an AC signal with excitation amplitude of 50 mV at a frequency of 500 Hz was superimposed to the DC bias V_{tg}. The drain and source electrodes were shorted to ground. The capacitance was measured by the out of phase components of the detected current (I_{gs}) with a LCR meter (Agilent 4284A). By varying the K^+ ion concentration from 0 μM to 1 mM in deionized water (DI), we obtained a series of left-shifted I-V curves from a representative epoxy coated graphene ISFET, as plotted in Figure 4.2 (a). The I_{ds}-V_{tg} curves measured all show a "V" shaped p-to n-type transition and the dip in the "V" corresponds to a minimum conductivity of ~$4e^2/h$ at the Dirac point (ED). [134] By comparing the slope of the transfer characteristics of the ISFET measured in air and electrolyte solution, we found the transconductance of the solution-gated graphene FET (~ 33 μS) is over 100-fold larger than that in air (~0.3 μS). The transconductance enhancement can be mainly attributed to the high mobility of charge carriers in graphene and the large interfacial capacitance at the graphene/solution interface [135], which will be discussed later in the section.

In addition, Figure 5.2 (a) shows a clear K ion concentration dependence of the ISFET transfer characteristics. The transfer curves shifted toward the negative direction of the electrolyte-gate voltage (V_{tg}) with increasing K^+ ion concentration, indicating that the prototype graphene ISFET detected K^+ ion in DI water. By biasing the device at a fixed V_{tg}, we extracted the corresponding I_{ds} with different K^+ ion concentration and plotted in Figure 5.3 (b). As expected, the drain-source current I_{ds} has a linear relationship with the K^+ ion concentration on a semilogarithmic scale. The sensitivity of the sensor was estimated to be 1 μA/decade from the slope of the linear fit.

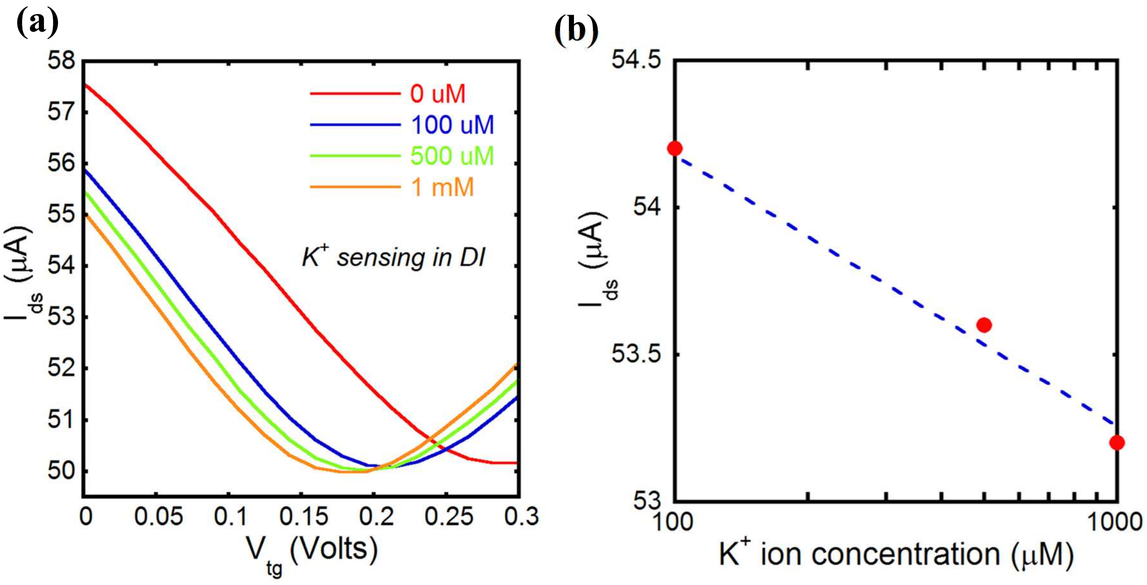

Figure 5.2: (a) I-V characteristics of an epoxy coated graphene ISFET in DI water with different K^+ ion concentration. In the measurement, V_{ds} was set to be constant 0.5 V and V_{tg} (solution-gated voltage) was swept from 0 to 0.3 V via a Ag/AgCl reference electrode (Bioanalytical System, Inc.) immersed in the solution. (b) Drain-source current I_{ds} as a function of K^+ ion concentration, at $V_{tg} = 0.05$ V.

5.1.2. C-V characteristics in electrolyte solution

In addition to I-V characterization, we also performed device C-V characterization in electrolyte solution. In C-V measurement, an ac signal with excitation amplitude of 50 mV at a frequency of 500 Hz was superimposed to the DC bias V_{tg}. The drain and source electrodes was shorted to ground. The capacitance was measured by the out-of-phase components of detected current. By sweeping V_{tg} from -0.8 to +0.8 V, we obtained a series of up shifted C-V curves with different K^+ ion concentration (as showed in Figure 5.3 (a)). Similar to the I-V measurement, by biasing the device at a fixed V_{tg} (e.g. $V_{tg} = 0.6$ V), we obtained the measured capacitance values with different K^+ ion concentration and plotted in Figure 5.3 (b). Interestingly, the measured capacitance of the ISFET shows a linear dependence on K^+ ion concentration like what was observed for the measured current, I_{ds}.

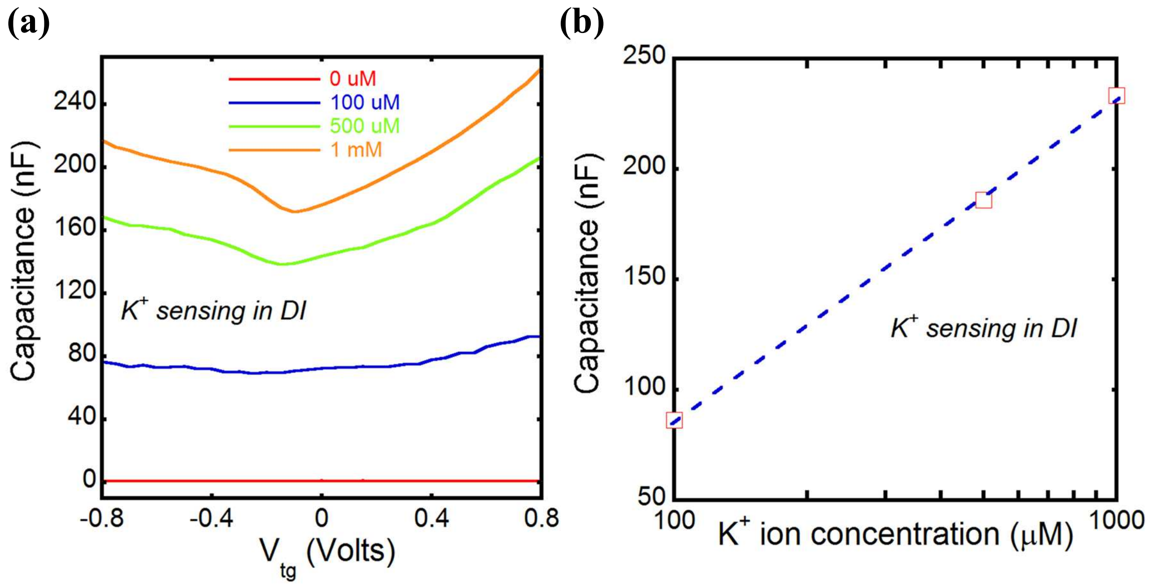

Figure 5.3: (a) Device C-V characteristics in DI water with different KCl concentration. (b) Measured capacitance as a function of K^+ ion concentration, at V_{tg} = 0.6 Volts.

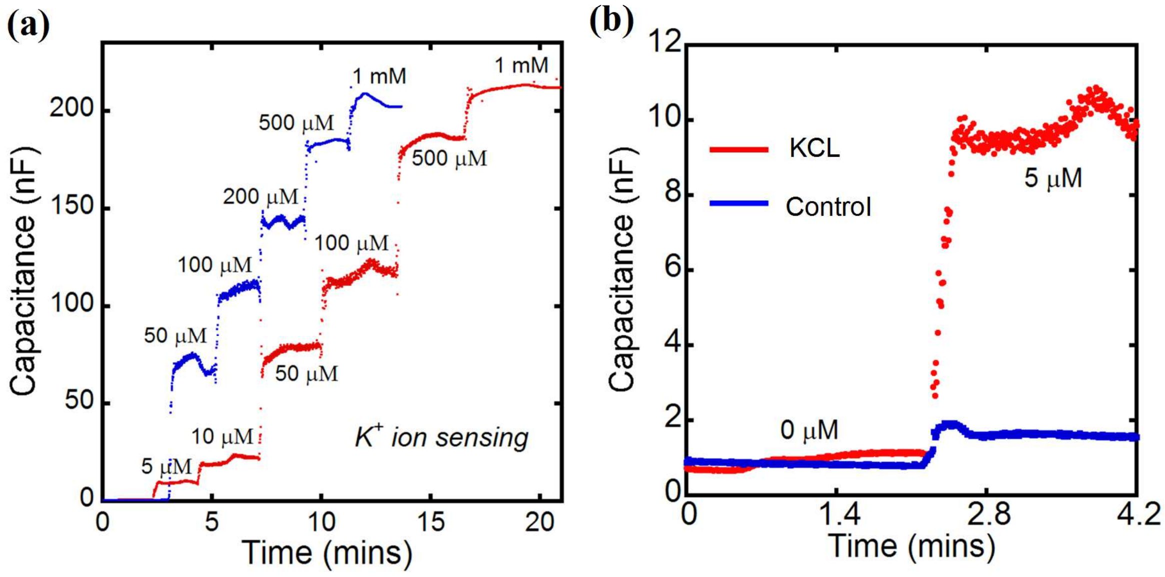

Figure 5.4: (a): Time dependent capacitance measurements with varying K^+ concentration from 0 μM to 1 mM in DI water. Two measurement cycles were performed with different steps in K+ concentration change. (b): Sensor response to 5 uM KCl (red curve) along with a control test without KCl (blue curve).

To demonstrate our graphene based ISFET has the capability of real-time detecting K+ concentration change in electrolyte solution, we operated the ISFET in its capacitive-mode at a fixed DC operating point, i.e. V_{ds} = 0.5 V and V_{tg} = 0.6 V. By sequentially introducing different volume of concentrated KCl solution into DI water, we were able to alter the K^+ ion concentration in the testing solution. Figure 5.4 (a) shows the time dependent sensor response to K^+ ion concentration change from 0 µM to 1 mM. As expected, the measured capacitance increased with higher K^+ concentration. Moreover, the ISFET sensor also shows very good sensing repeatability in multiple measurement cycles with different steps in K^+ concentration change. To determine the sensor resolution, we also did a control test by introducing K^+ free control solvent (DI water here) into the testing solution. The results (plotted in Figure 5.4 (b)) clearly indicate our ISFET sensor is able to detect K^+ ion concentration change down to 5 µM in DI water.

To further identify the measured capacitive components in the device C-V characterization discussed above, we analyzed the equivalent electrical circuit involved in the measurement. As illustrated in Figure 5.5, at a fixed electrolyte solution-gate voltage V_{tg}, two electrical double layers are formed at the interface between reference electrode/solution and graphene/solution, respectively. [120, 121] In addition to these two capacitive components, the quantum capacitance of graphene also exists in the circuit and is in series connection with the two double layer capacitances. Along with the capacitive components, there are also resistive components contributed by the bulk solution and graphene. Since LCR meter measures the out of phase components of detected current, the measured impedance only consists of the capacitive components of C_{EDL1}, C_{EDL2} and

$C_{Q,}$ respectively. The two series connected capacitance C_{EDL2} and C_Q constitutes the so called solution/graphene interfacial capacitance ($C_{interfacial}$), which acts as the gate capacitance of the graphene ISFET.

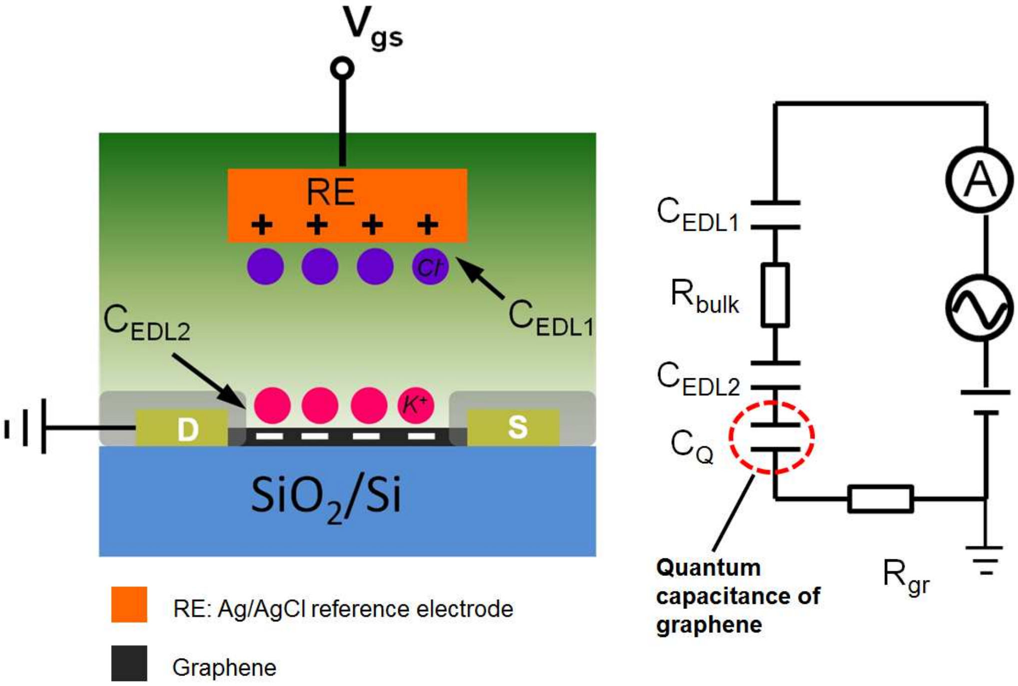

Figure 5.5: Schematic diagram of a graphene ISFET under C-V characterization in KCl electrolyte together with the equivalent electrical circuit describing its operation [120, 121]. In the circuit, C_{EDL1} and C_{EDL2} represent electrical double layer capacitance formed at reference electrode (RE)/electrolyte and graphene/electrolyte interfaces, respectively. R_{BULK} and R_{gr} correspond to the electrical resistance of bulk salt solution and graphene thin film, respectively.

To extract $C_{interfacial}$ from the capacitance measured by the LCR meter, we measured the electrical double layer capacitance at the reference electrode/solution interface (C_{EDL1}). In the measurement, we substituted the graphene ISFET with another identical Ag/AgCl reference electrode and repeated the C-V measurement with the same experiment condition as discussed earlier (1st paragraph, Section 4.1.2, page 3). The measured C_{EDL1} and the calculated $C_{interfacial}$ with different K^+ ion concentration are plotted in Figure 5.6 (a) and (b), respectively.

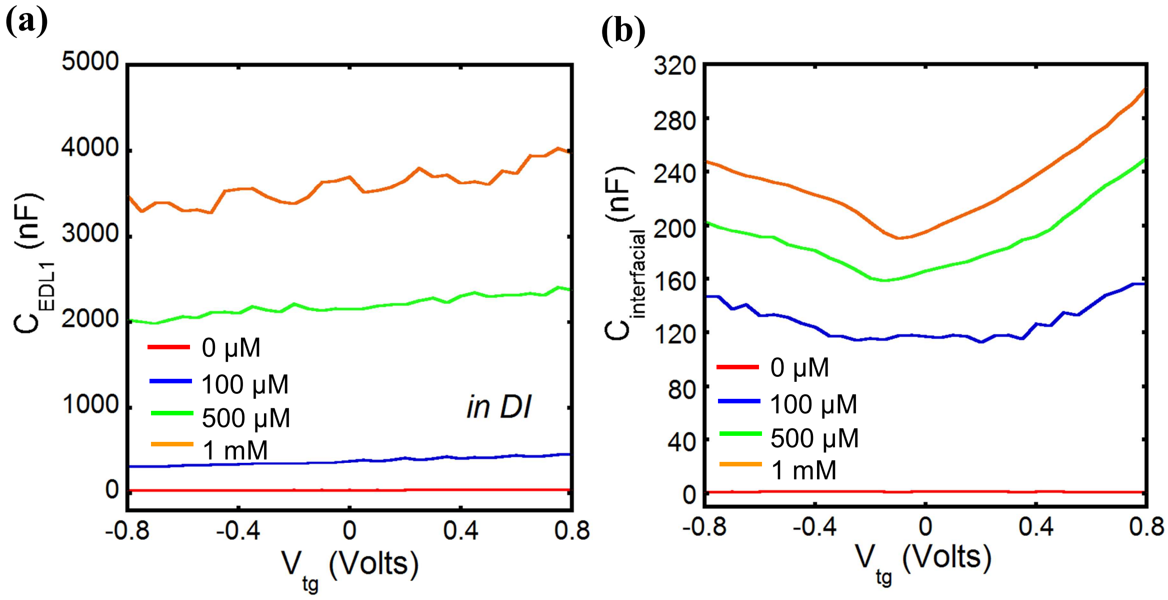

Figure 5.6: C-V characteristics at (a) reference electrode/solution interface (C_{EDL1}) and (b) graphene/solution interface ($C_{interfacial}$) in DI water with different KCL concentration.

5.1.3. Sensitivity saturation in physiological (buffer) solution

In addition to characterizing the graphene based ISFETs in DI (deionized) water, we also studied the sensor response to K^+ ions in physiological buffer solutions (e.g. saline and N-methyl D-glucamine (NMG)), which offer suitable environment for cell growth and living. Figure 5.7 shows the K^+ sensing response of the graphene ISFET in NMG solution. We observed slight left shift of the I-V curves and much smaller current change at fixed Vtg as opposed to the sensor behavior in DI water (Fig. 5.2 (a)). The K+ sensitivity seems to be saturated by other interference charges (e.g. Na^+, Ca^+, etc.) existing in the solutions. To achieve selective K^+ sensing in physiological buffer solution, we coated the graphene surface with a valinomycin/polymer membrane. The fabrication and characterization of the surface modified graphene ISFET are discussed in the following section.

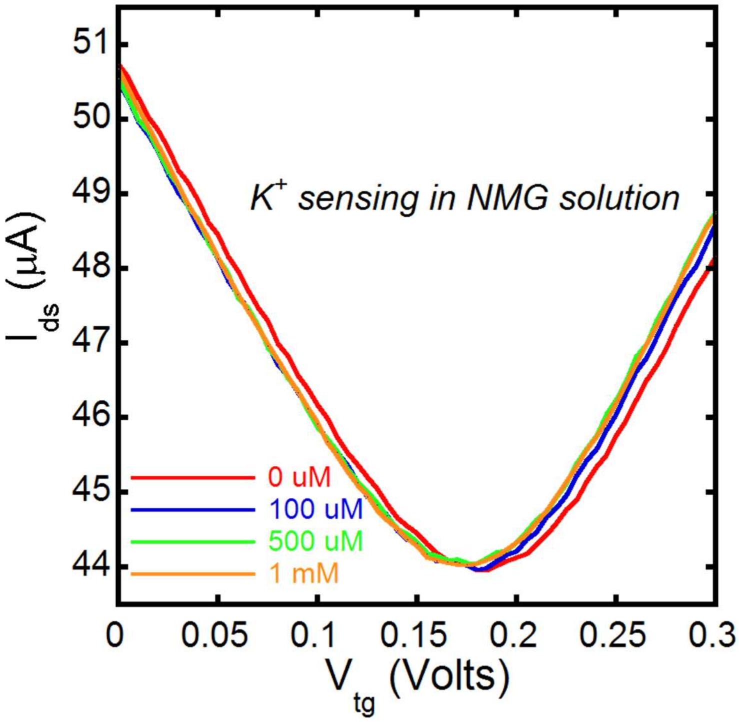

Figure 5.7: Sensor response to K^+ concentration change in physiological buffer solution (NMG + 1 mM $CaCl_2$ here).

5.2 Ionophore modified graphene ISFET

5.2.1 Sensing mechanism

Figure 5.8 (a) shows the device structure of surface modified graphene ISFET with a valinomycin/polymer based K^+ ion selective membrane (ISM) incorporated into the gate of the FET. Valinomycin ($C_{54}H_{90}N_6O_{18}$) is a K^+ ionophore with a doughnut-like structure [136, 137] (as illustrated in Fig. 5.8 (b)). Because of its unique shape and size, it has a high affinity for K^+ relative to other alkali metal ions like Ca^{2+} and Na^+. Similar to the case of valinomycin modified Si nanowire FET [138], when interfacing with electrolyte solution, ideally valinomycin only selectively traps K^+ ion from the solution and forms valinomycin-K^+ complex, which further diffuses to the vicinity of graphene surface (as illustrated in Figure 5.9). The electrical field exerted from the captured K^+ ions affects the conductivity of graphene channel and thus induces an electrical sensing signal.

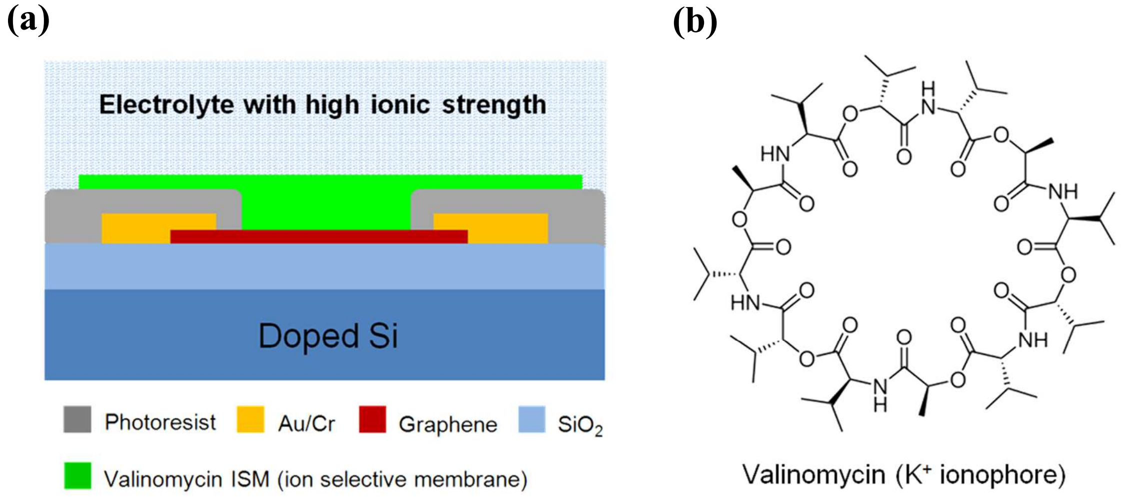

Figure 5.8 (a) Device structure of a valinomycin/polymer modified graphene ISFET (cross section view). (b) Molecule model of valinomycin.

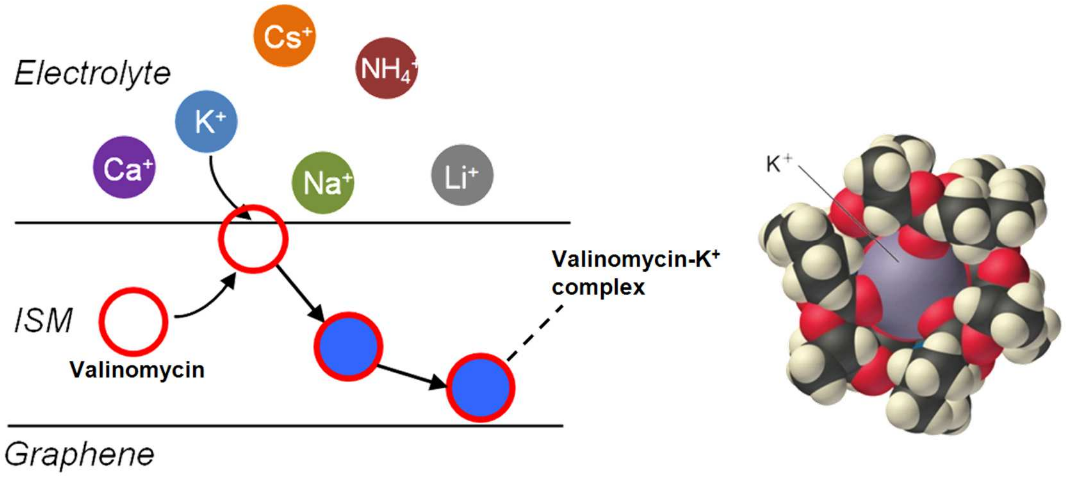

Figure 5.9 Schematic showing valinomycin ISM selectively passing K^+ ion to the vicinity of graphene surface.

5.2.2 Device fabrication

The K^+ ISM was prepared [139] by dissolving 4 mg valinomycin (VAL), 0.55 mg potassium tetrakis (4-cholorophenyl) borate, 195 mg acrylic matrix (made of methyl methacrylate (MMA) and n butlyacrylate (nBA) monomers in proportion of 1:10 [140]) in 2.0 ml of dichloromethane [141]. To coat the graphene FETs, VAL-polymer membrane was spin coated on top of the active sensing area of the devices (Fig. 5.8(a)) and air-dried. The optical image of Figure 5.10 shows a typical K^+ ISM coated graphene ISFET. A 60s spinning at 5000 rpm results in a membrane thickness of about ~ 4 μm measured with a profilometer. By controlling the spin coating parameters, we should be able to adjust the thickness and the composition of the membrane for optimized sensor performance. It is one part of the future investigation in our bio-FET development.

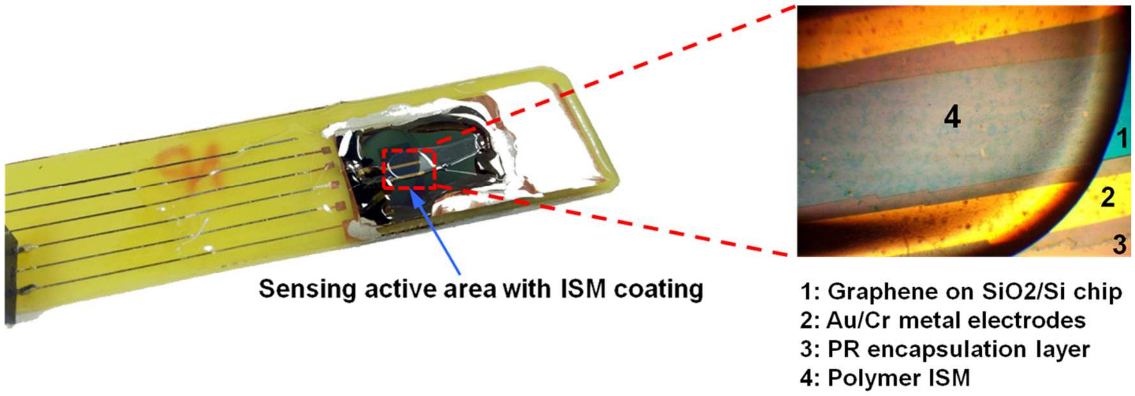

Figure 5.10: Optical image of a representative valinomycin/polymer modified graphene ISFET with a magnified zoom-in view on its active sensing area.

5.2.3 I-V characteristics in electrolyte solution

We studied the K^+ sensing response of the graphene ISFET before and after ISM coating in DI water (plotted in Figure 5.11 (a) and (b)) and compared its sensor performance in terms of relative Dirac point shift and current change (Fig. 5.11 (c) and (d)). From the results, we found that the ISM coating boosted the device sensitivity to K^+ ion concentration change in DI water.

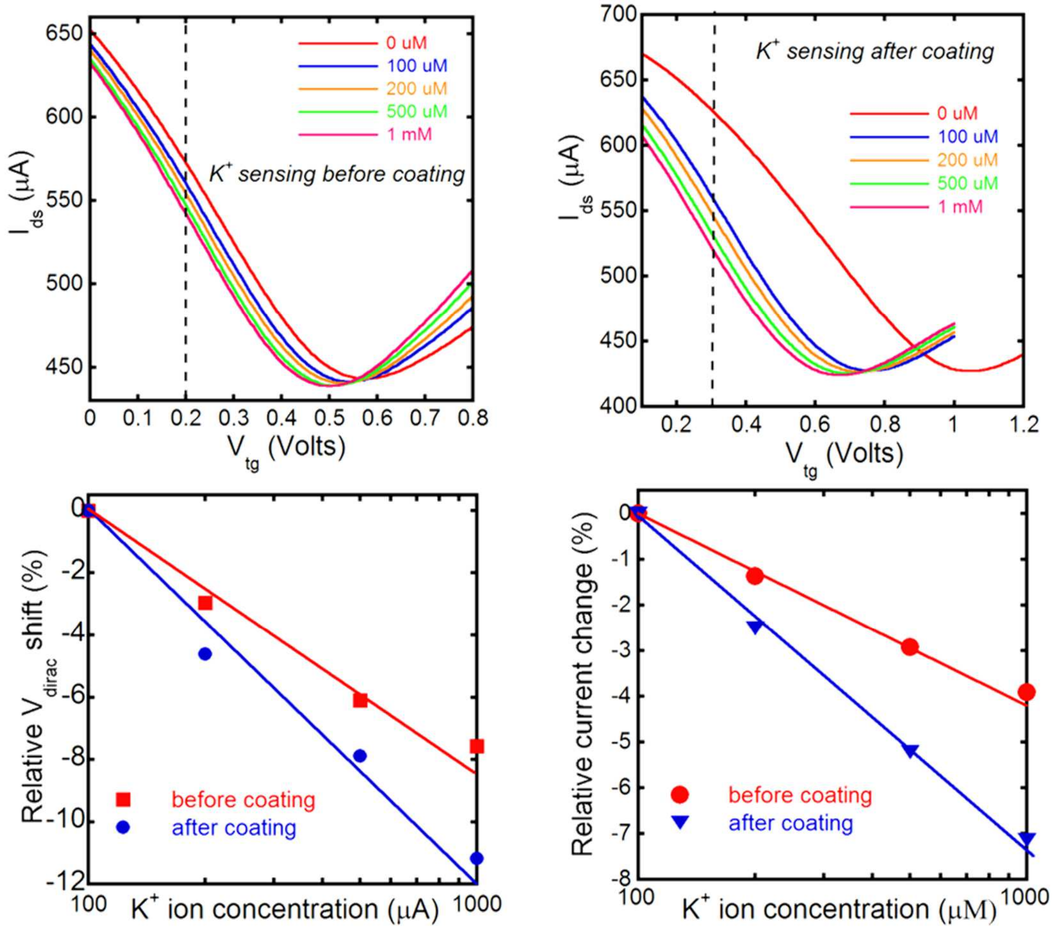

Figure 5.11: (a) and (b): Sensor response to K^+ ion concentration change in DI water before and after ISM coating. (c) and (d): Device sensitivity comparison before and after ISM coating in terms of relative Dirac voltage shift and current change.

In addition to sensitivity, the K^+ ion selectivity of the sensor device has also been studied in DI water in the presence of interference alkali ions of Na^+ and Ca^{2+}. From the results (plotted in Figure 5.12 (a) and (b)), we observed that the sensor did not show any noticeable response to Na^+ ions. It did show response to Ca^{2+} ions but with much less

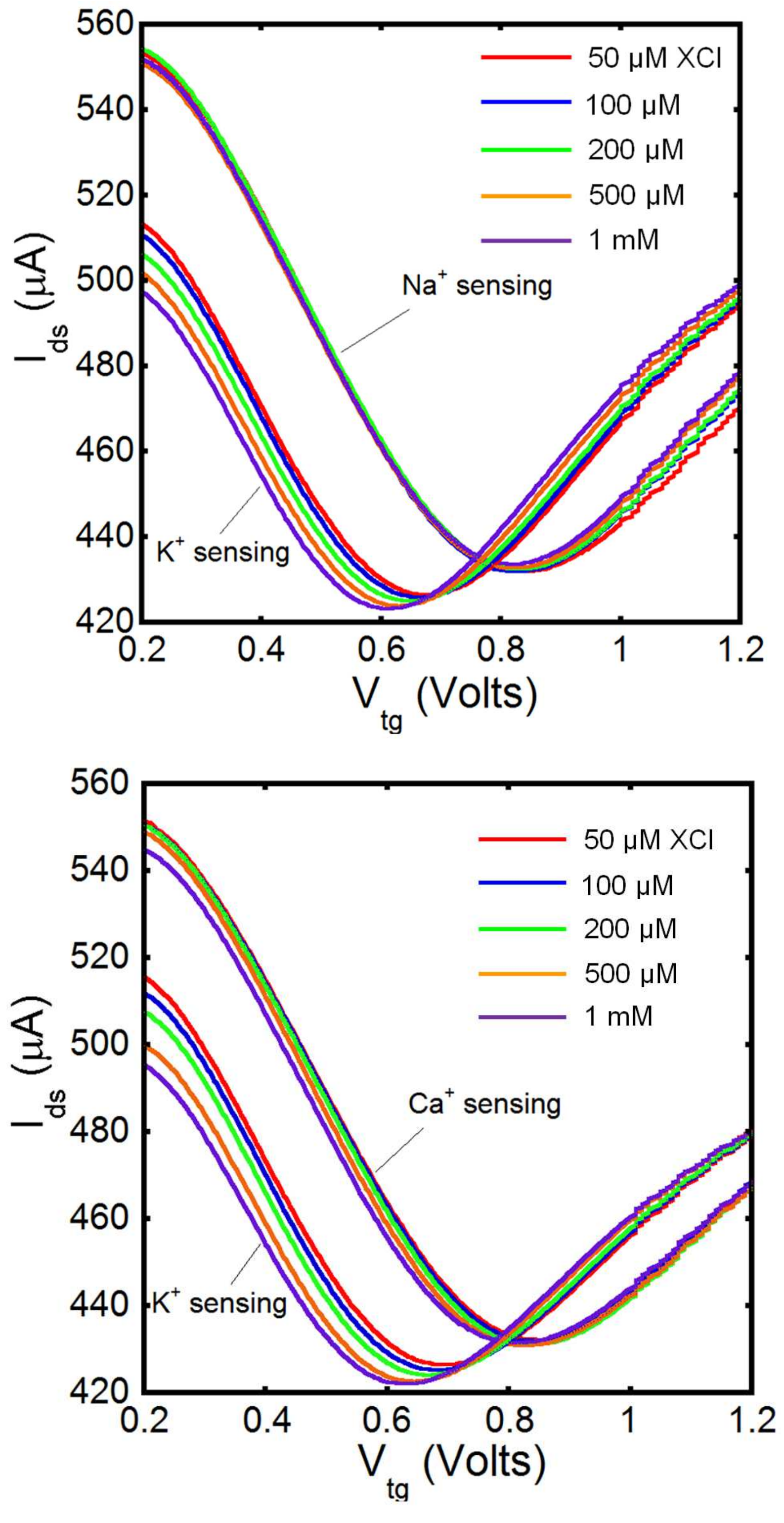

Figure 5.12 (a) and (b): Sensor response to K^+ ion concentration change in DI water in the presence of Na and Ca ions. Increasing concentration of NaCl/$CaCl_2$ was first added to the solution followed by KCl from 50 μM to 1 mM.

sensitivity as compared to K^+ ions. In the physiological buffer solution of N-methyl-d-glucamine (NMG), the sensor device showed noticeable K^+ response after ISM coating (Figure 5.13) as opposed to non-response before coating (the inset of Fig. 5.13). So far, we have demonstrated a prototype graphene based ion sensor, which shows promising K^+ selective sensing property in electrolyte solution.

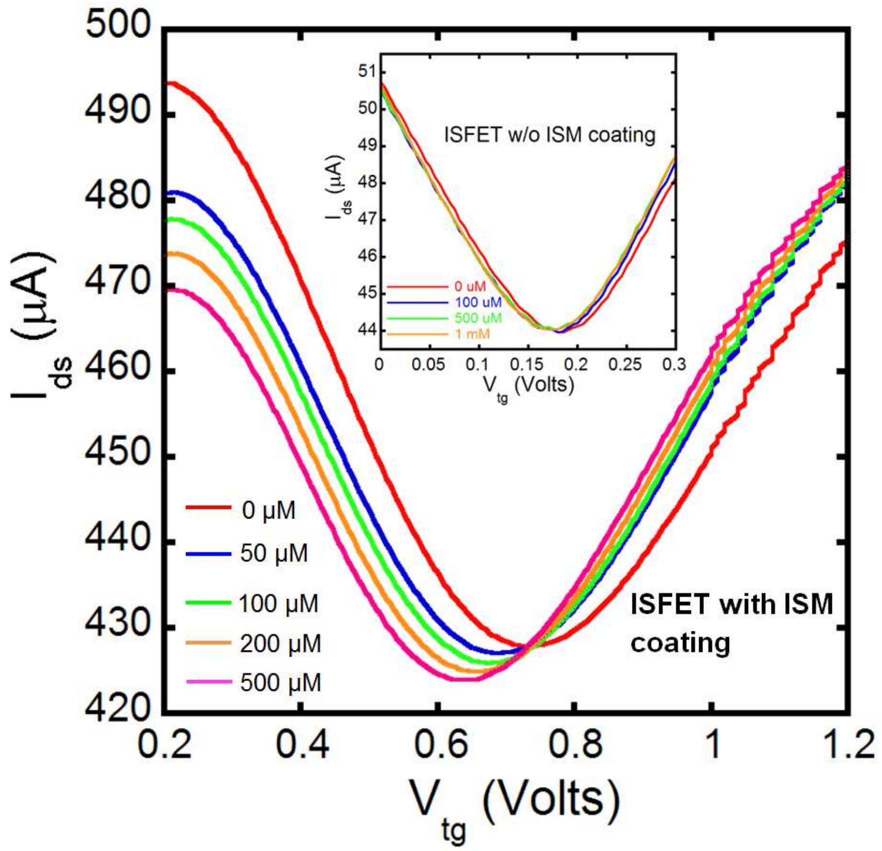

Figure 5.13: Sensor response to K^+ ion concentration change in NMG physiological buffer solution with and without ISM coating.

5.3 Time dependent K^+ ion detection

5.3.1 K^+ ion sensing using bulk Ag/AgCl reference electrode

To prove the feasibility of using our graphene based ISFET for cell based real-time K^+ efflux detection, we studied the time dependent K^+ sensing response of the ISM coated graphene ISFET in both DI water and physiological buffer solution saline.

To start with, we first performed K^+ ion sensing experiment in a glass beaker, filled up with ~23 ml of DI water, using the bulk, commercial Ag/AgCl reference electrode (Bioanalytical System, Inc.). Right before the time dependent measurement, the I-V characteristic of the sensor device was obtained (Figure 5.14 (a)), which serves as a reference for us to find the optimal DC operating point with highest transconductance (maximum K^+ ion sensitivity). From the measured transfer characteristic of the graphene ISFET, we determined the biasing point to be 0.5 V and 0.65 V for the drain to source voltage (V_{ds}) and solution-gated voltage (V_{tg}) respectively, which corresponds to the highest transconductance achievable with the FET device under test. To calibrate the graphene ISFET, we increased the K^+ ion concentration in the beaker by introducing different volume of concentrated KCl solution into the DI water, using a micropipette (Bio-Rad Laboratories). Figure 5.14 (b) gives the measured time-dependent current change with varying K^+ ion concentration. As expected, the current decreased with increasing K^+ ion concentration in the solution. In addition, we also found the measured current has a linear relationship with K^+ concentration (inset of Fig. 5.14 (b)). The slope of linear fit, which represents the ISFET sensviity, was estimated to be ~25 uA/decade, which is much larger than the value of 1 uA/decade achieved with bare graphene ISFET without valinomycin/polymer ISM coating.

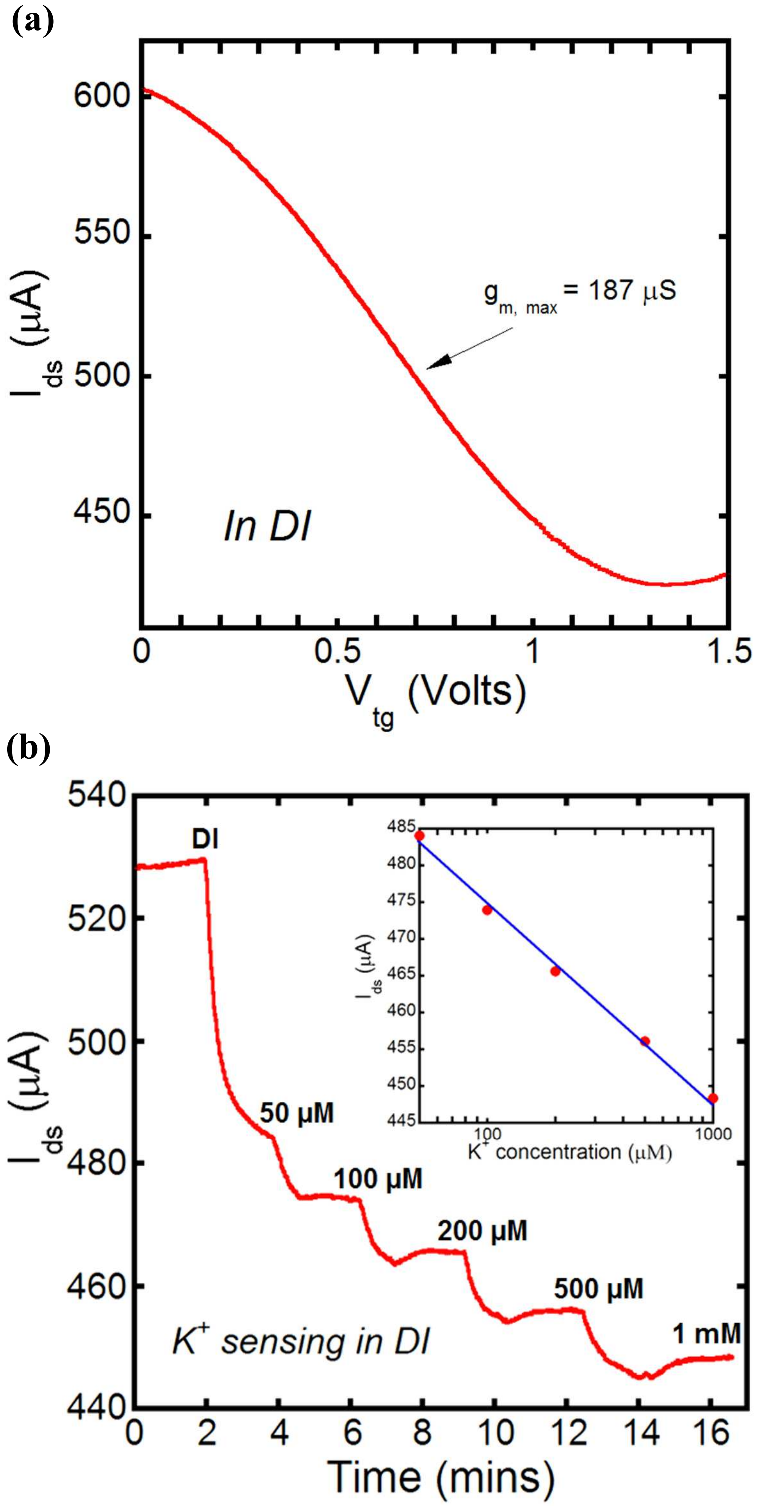

Figure 5.14: (a) Transfer characteristic of the ISM coated graphene ISFET measured in DI using bulk Ag/AgCl reference electrode. (b) Time dependent sensor response to K+ concentration change in DI water. Inset of the figure plots the measurement Ids as a function of K+ concentration.

Adopting the same experiment procedure above, we conducted the time dependent K^+ ion sensing experiment in the physiological solution, K^+-free saline (containing 140 mM NaCl) and plotted the results in Figure 5.15. Like in DI case, the measured current I_{ds} decreased with increasing K^+ ion concentration. The inset of the figure plotted I_{ds} as a function of K^+ ion concentration, which shows a linear sensor response to K^+ ions as expected. The sensitivity was determined to be ~ 23 µA/decade, which is close to the value measured in DI case (~ 25 µA/decade). The consistency of sensor performance (i.e. K^+ sensitivity here) in both DI and saline solution indicates that the valinomycin/polymer membrane serves well as a buffer layer, which efficiently blocked interference ionic charges other than K^+ ions in the testing solution.

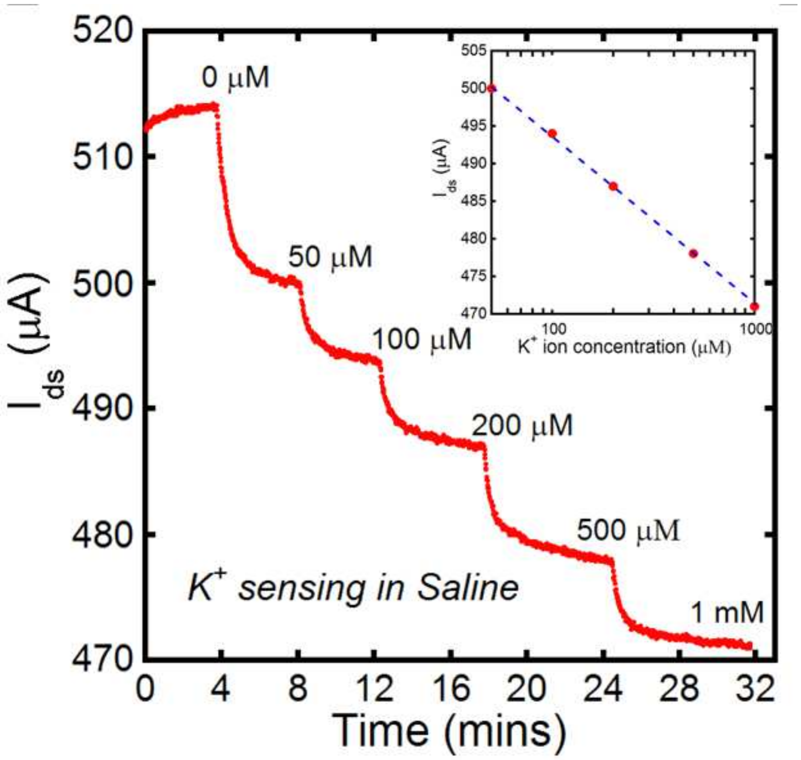

Figure 5.15: Time dependent sensor response to K^+ concentration change in K^+ free saline solution. Inset of the figure plots the measurement Ids as a function of K^+ concentration.

5.3.2 K$^+$ sensing using salt bridge configuration

In addition to characterize our graphene ISFET in bulk (~ 25 ml) testing solution, we also performed on-chip K$^+$ sensing experiment with small droplet of solution (100 ~ 200 µl) using a salt bridge configuration, which allows us to have a better sensing resolution later in the cell based K$^+$ efflux measurement described in Section 4.3.3.

Figure 5.16 shows the experiment setup. A small droplet of the testing solution (100 to 200 µL DI water/K$^+$-free saline) was placed on top of the ISFET active sensing area by micropipette. To accommodate the Ag/AgCl reference electrode in the solution droplet, we substituted the conventional bulk reference electrode (~6 mm in diameter) with a salt bridge configuration. As illustrated in the optical image, one end of the salt bridge (~ 1 mm in diameter) was immersed in the testing solution and the other end in a plastic chamber having a Ag/AgCl pellet mounted on its side wall. The chamber was filled up with the same testing solution as on top of the senor. By applying a DC bias on

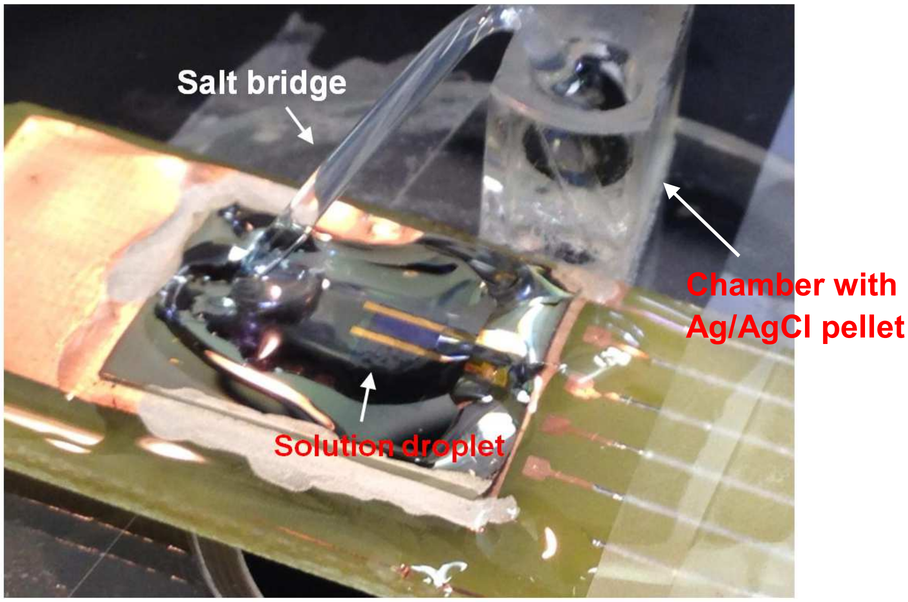

Figure 5.16: Optical image of the experiment setup for the ISFET sensor characterization using salt bridge configuration.

the Ag/AgCl pellet, we are able to control the potential of the testing solution via the salt bridge. Figure 5.17 (a) shows us the ISFET I-V characterization result measured in 200 μL DI water with 100 μM KCl using the salt bridge configuration, which is quite similar to the device I-V characteristics (Fig. 5.14 (a)) obtained using the bulk referent electrode. In addition, we also measured the time dependent sensor response to varying K^+ concentration in both DI and K^+ free saline solution and plotted the results in Fig. 5.17 (b) and (c), respectively.

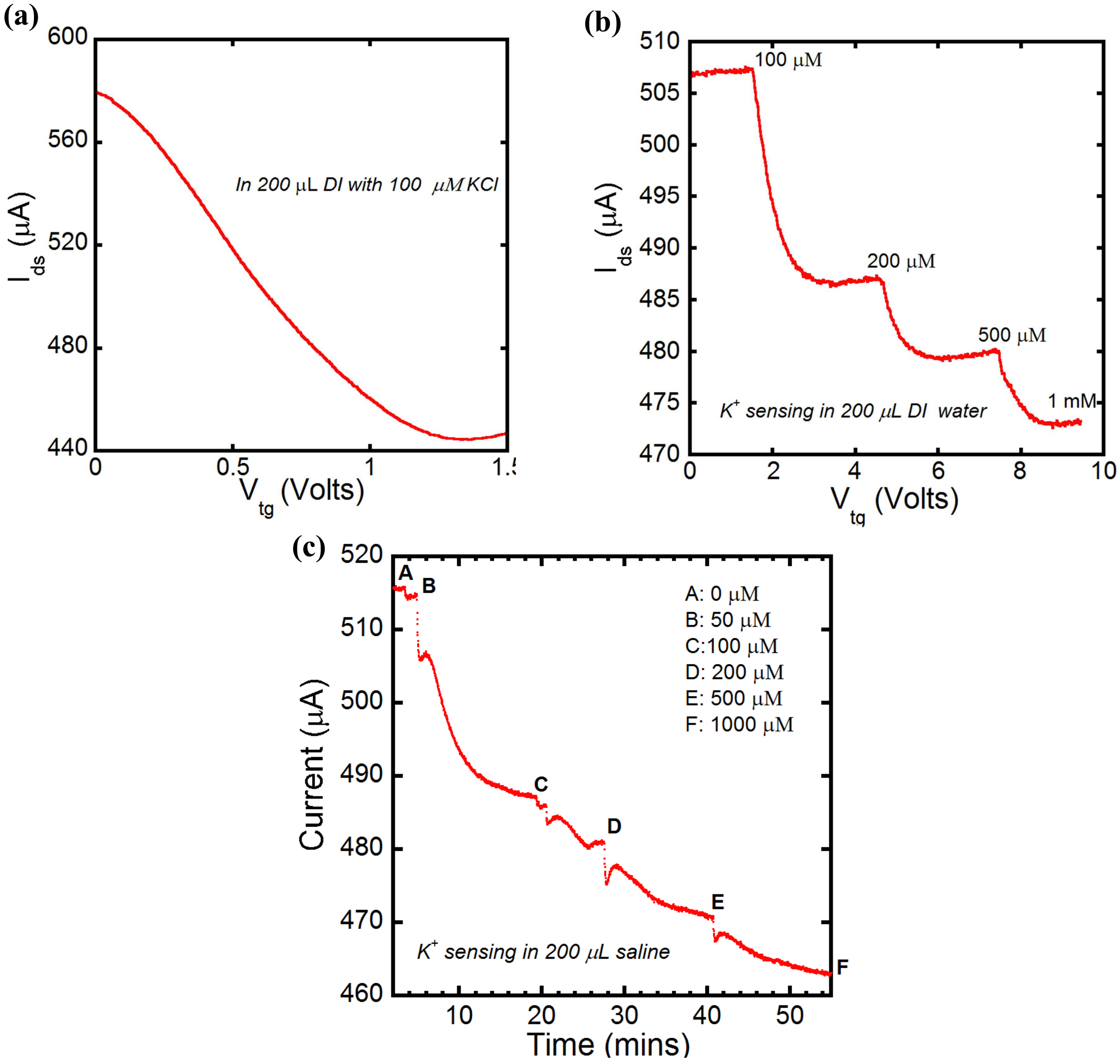

Figure 5.17: ISFET I-V characteristic measured in a 200 μl droplet of DI water with 100 uM KCl using the salt bridge configuration. (b) and (c) The time dependent sensor response to varying K concentration in 200 μl DI/K+ free saline solution

From the experiment results above, we concluded that the salt bridge configuration works well as a substitution to conventional bulk reference electrode probe The new experiment set up enables us to conduct the real-time K^+ sensing experiment in a testing solution of much smaller volume (µL scale) than in bulk solution (mL scale).

5.4 Cell based real-time K^+ efflux measurement

5.4.1 Measurement using Si based ISFET

Utilizing the state-of-art commercial Si ISFET probes, we conducted the real-time measurement of K^+ efflux from living cells cultured in single and multi-well plates and reported the experiment results in our recent publication [5], which is briefly discussed in the following sections.

A. Experimental methodology

The experiment set-up is shown in Figure 5.18 (a). An array of K^+-sensitive silicon-based ISFET probes were inserted in multi-well culturing plates with living cells (Human colonic T84 epithelial cells). The ISFET sensors (Fig. 5.18 (b)) were obtained from D+T Microelectronica (Spain). The gate of the ISFETs was coated with a polymeric membrane containing the K^+ ionophore valinomycin giving the probes K+-sensitivity. T 84 cells were obtained from ATCC. Details regarding cell culture and plating can be found in our recent report.[5] To obtain electrical sensing signal from the probes, each sensor was connected to an interface circuit (as shown in Fig. 5.18 (c)) consisting of a voltage follower, a current source and a low-pass filter. It was determined during initial testing that the ISFETs have a 1.2 dB signal-to-noise ratio (SNR) near the end of their rated usable life. High frequency noise was removed using the low-pass 1 Hz 2nd order butterwort filter to achieve an SNR of 34 dB on the same sensors. This effectively increased the usable life of the ISFETs for the K^+ measurements. The interface was placed in an array on a PCB board to reduce noise and simplify measurements. Data was logged using a data acquisition unit (DAQ) (Agilent 34972 A). During ISFET calibration and real-time K^+ efflux measurement, the interface supply voltage (Agilent E3649A) was adjusted while observing the DAQ. The voltage used in the experiments was the highest allowable that did not produce signal oscillations.

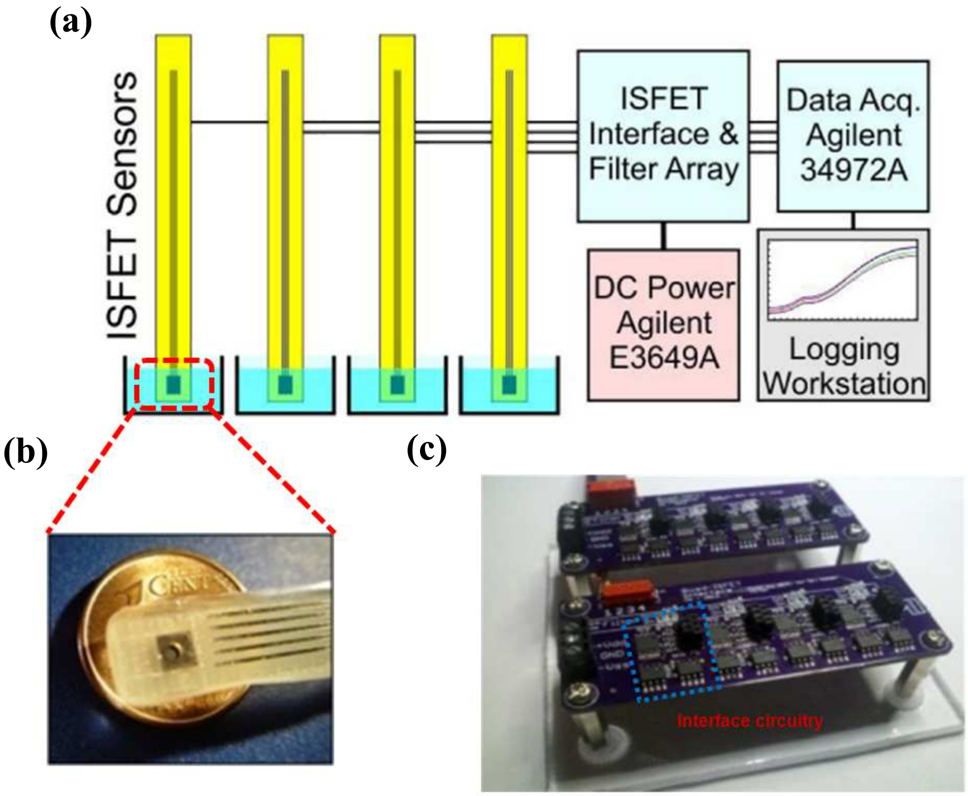

Figure 5.18 (a): Schematic of the measurement setup with multiple parallel ISFET probes along with the DAQ and recording equipment. (b): Optical image of a commercial silicon ISFET probe (D + T Microelectronica, Spain). (c) PCB boards contained an array of ISFET interface circuitries consisting of voltage follow, current source and low-pass filter.

As illustrated in Figure 5.19, when a certain drug compound served as ion channel modulator (e.g. A23187 here) is added to one of the culturing plates, it induces Ca^{2+}-activated non-selective cation (NSC) channel opening on the cell membranes, thus resulting in an increase in K^+ efflux from the living cells. By positioning the ISFET sensor close to the cells in physiological solution (K^+-free saline here), extracellular K^+ ion concentration change can be real time probed.

Different drug compounds served as ion channel modulators can be added to an array of culturing wells and drug induced K^+ efflux from living cells will be simultaneously measured and recorded from each well, thus achieving a prototype ISFET based ion channel screening assay for drug discovery.

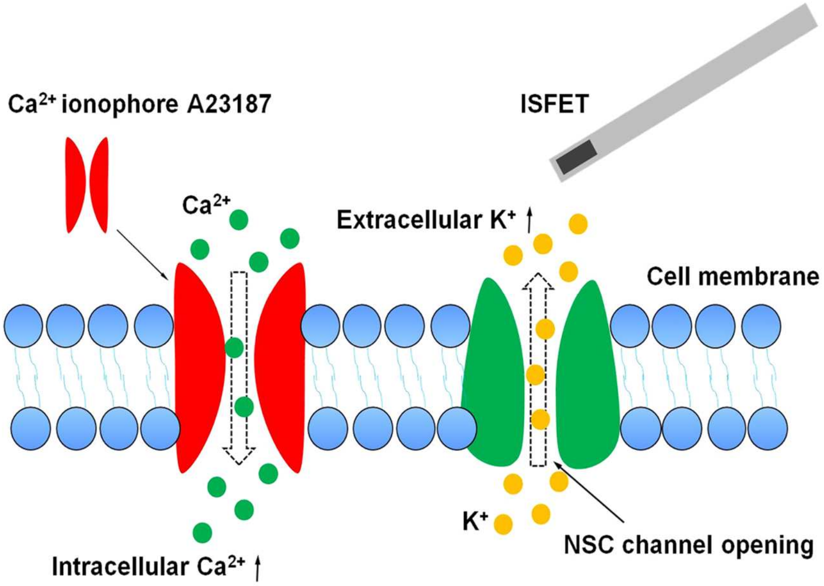

Figure 5.19: Illustration of real time K^+ efflux measurement using ISFET probe in a single well plate [5]. Addition of A23187, a cell ion channel modulator, induces the opening of the non-selective NSC channel, resulting K+ efflux from the cells. The in-situ extracellular K+ concentration change is real-time transduced by an ISFET probe to an electrical signal which is recorded by a computer.

B. Sensing results and discussion

The cell based sensing results are showed in Figure 5.20. Immediately prior to each K^+ efflux measurement experiment, a K^+ concentration (μM) versus ISFET (mV) calibration curve was obtained. This was measured by adding increasing concentrations of KCl to a chamber (without cells) containing K^+-free saline. Over the concentration range of 20 μM – 200 μM (the typical range of K^+ efflux measured from T84 cells used in this study[41]), the calibration curve displayed a linear relationship as showed in Figure 5.20 (a). The applicability of ISFET for real-time measuring K^+ efflux from ion channel (the Ca^{2+} - activated NSC channels in T84 cells here) was evaluated in Figure 5.20 (b) with single cell culture well format and (c) with multi-well format, respectively. Each figure plots the K^+ ion concentration, calculated from the calibration curve (Fig. 5.20 (a)), real time measured from single/multiple chambers containing T84 cells. By dosing the cells with the drug compound A23187 to open the NSC channels, we observed an time-dependent increase of extracellular K^+ ion concentration with the ISFET probe (blue curve in Fig. 5.20 (b)) as compared to quite stable efflux level measured from cells without the drug treatment in the control test (red curve in the figure). Figure 5.20 (c) shows us the time-dependent K^+ efflux measurement simultaneously taken from three culture wells. Upon dosing the drug, we observed an increase in extracellular K^+ ion concentration from all the three wells, as we observed in the case of single culture well, proving the concept of ISFET based ion channel screening assay.

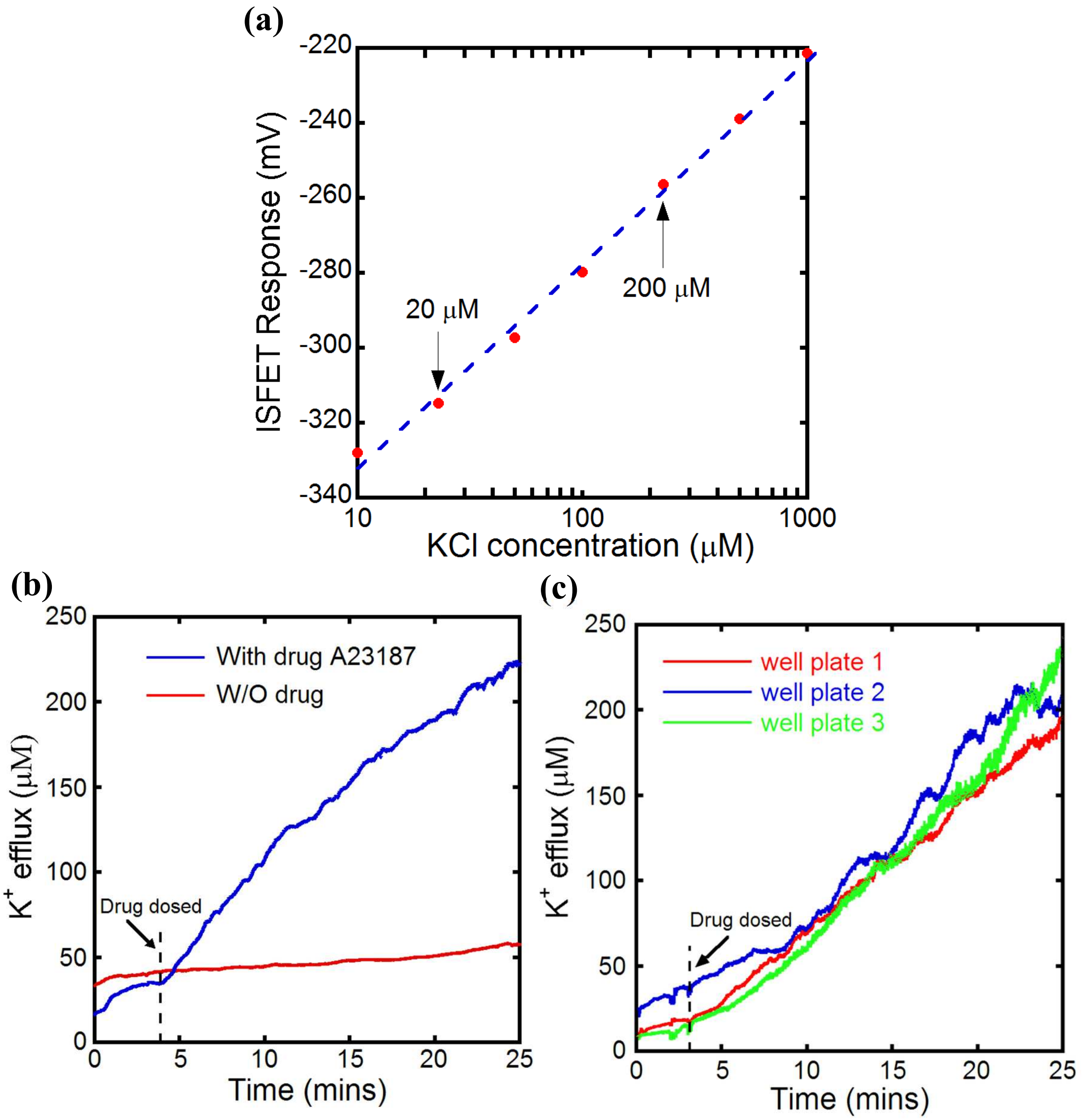

Figure 5.20: (a) K^+ sensing calibration curve of a representative Si ISFET probe measured in 140 mM NaCl saline solution. (b): K^+ efflux from T84 epithelial cells real time recorded with an ISFET in a single culture well. Blue curve represents the K^+ efflux from cells treated with the drug compound A23187. Drug was added following the basal efflux measurement (see arrow). Red curve shows K^+ efflux measured in control test without the drug treatment. (c): K^+ efflux measured in parallel from three recording chambers containing T84 cells with the drug treatment.

5.4.2 Measurement using valinomycin modified graphene ISFET

So far we have successfully demonstrated the feasibility of using commercial Si based ISFET for K^+ efflux measurement from living cells. We further evaluated our prototype graphene based ISFET for the same application propose.

A. Measurement setup

As to obtain a larger K^+ ion concentration change in the testing solution due to K^+ efflux released from the living cells (T84 cells here), we placed a small droplet of the testing solution (100 to 200 μL K^+-free saline) on top of the ISFET sensor instead of inserting the device in the mL bulk solution as we did with the commercial Si ISFET. To accommodate the Ag/AgCl reference electrode in the solution droplet, we substituted the bulk reference electrode probe with a salt bridge configuration as shown in Fig. 5.16, Section 4.3.2. One end of the salt bridge was immersed in the saline solution and the other end in a plastic chamber filled up with the same solution and having a Ag/AgCl pellet mounted on its side wall. By applying a DC bias on the Ag/AgCl pellet, we are able to control the potential of the testing solution via the salt bridge. Prior to the K^+ efflux measurement, we calibrated the graphene ISFET in both DI water and K^+-free solution using the salt bridge configuration described above. Concentrated KCl solution with different volume was sequentially added to the solution droplet of 200 μL using a micropipette. K^+ ion concentration change in the solution was real-time probed by the ISFET sensor.

To measure the real time-K^+ efflux from living cells, we placed a piece of cover glass on top of the solution droplet (K^+-free saline) with its top surface facing to the solution, where T84 cells were growing on. Right before the K^+ efflux measurement, we first measured the I-V characteristics of the ISFET device in the testing solution without living cells (Figure 5.21 (a)). Afterwards, a fixed DC bias of 0.5 Volts was applied between the source and drain electrodes and solution-gated voltage (V_{tg}) was adjusted to modulate the graphene channel conductance so that desired operating point was set for maximum detection sensitivity.

B. Sensing results and discussion

Figure 5.21 (b) shows the measured time-dependent current change during the cell-based experiment. Upon the placement of cover glass with living cells (point A in the plot), current I_{ds} gradually decreased. At point B, drug compound A23187 was added to the testing solution. A plateau appeared followed by continuous current decrease with a slight steeper slope. Using the calibration results obtained in K^+ free saline (Figure 5.17 (c)), we calculated the corresponding K^+ concentration (K^+ efflux) real-time probed by the graphene ISFET and plotted it as a function of time. As shown in Figure 5.21 (c), before dosing the drug at point B, a small increase (~ 1 μM) in extracellular K^+ ion concentration was detected, this might result from K^+ efflux spontaneously leaked via the cell ion channels. However, after dosing the drug, we observed a much larger K^+ ion concentration increase (~ 13 μM) and the slope of the measurement curve gradually increased, which are consistent with the sensing results obtained using the commercial Si based ISFETs (Fig. 5.20) The observed increase in K^+ ion concentration could be attributed to the effect of the drug, A23187, which opened the non-selective NSC channel of T84 cells and resulted in enhanced K^+ efflux from the cells.

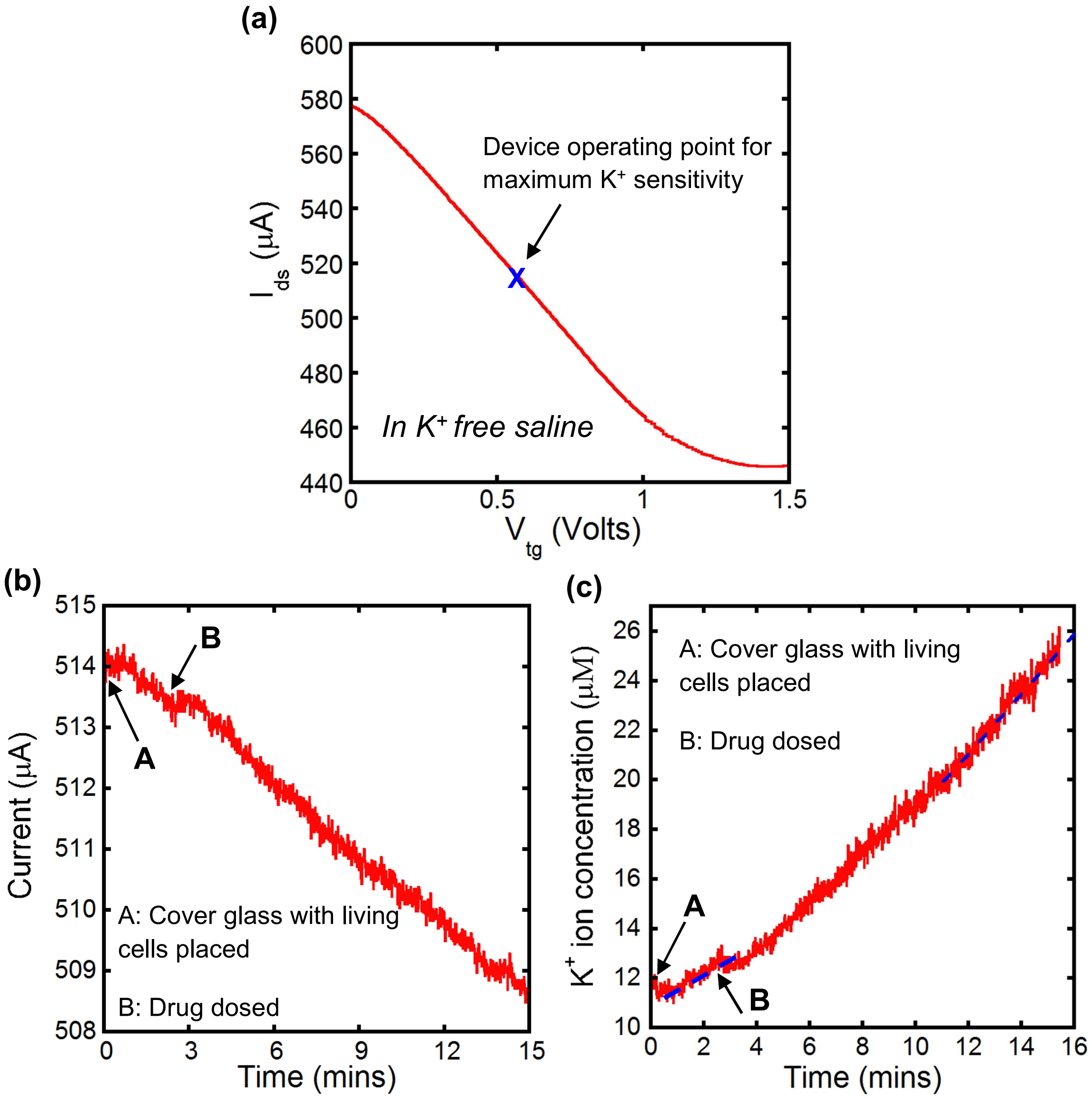

Figure 5.21 (a): I-V characteristic of the ISFET in K^+ free saline measured right before the cell-based K^+ efflux measurement. DC operating point for maximum sensor sensitivity was noted by the blue cross mark on the I-V curve. (b) Time dependent current change measured during the cell based experiment. Point A: Cover glass with T84 cells growing on was physically placed on top of solution surface. Point B: Drug compound, A23187 was dosed into the testing solution. (c) Extracellular K^+ ion concentration change real time recorded with the graphene ISFET. The blue dotted lines indicate the slope change in K^+ concentration increase before and after dosing the drug compound, A23187.

CHAPTER 6

CONCLUSION AND FUTURE DIRECTIONS

In this dissertation, we studied three types of sensing technologies for applications in human physiological monitoring, which includes pressure, oxygen and ion detection. Three general types of thin film based sensors have been designed, fabricated and characterized. The following section summaries the major contributions in each sensor development.

6.1 Major contributions of this work

6.1.1 Thin film based biocompatible pressure sensor

In the pressure sensor development, a simple yet highly sensitive pressure sensor based on Au film resistor patterned on the PDMS thin membrane has been designed, fabricated and characterized. The sensor was extensively modeled through COMSOL-based finite element simulations for design and performance prediction. Three prototype sensors fabricated with different membrane thickness of 50, 100 and 200 μm were studied. Very high constant sensitivities of 0.1 /Kpa, 0.056 /Kpa and 0.012 /Kpa, respectively, were observed over their effective measurement ranges. The high sensitivities are attributed to the formation of microcracks in Au film resistor when the sensors are subjected to pressure. Interestingly, the formation of microcracks seemed to be quite reversible within certain pressure range. In addition, the correlation of sensitivity and effective sensing range with membrane thickness was studied for the three sensors. It was found that the device sensitivity increased with the decrease in membrane thickness but at the expense of its effective sensing range. This observation corresponds well to the simulation results. Response times of all the three sensors were found to be in millisecond range, and the best rms noise limited resolution was 0.07 mmHg (9 Pa).

The very high sensitivity coupled with simple device construction, ease of fabrication, biocompatibility and fast response time make the pressure sensor highly promising for a wide range of biomedical applications. The small footprint (3 x 3 mm^2) of the sensor device, which can be further miniaturized as necessary, also allows for high pixel density over large area for artificial skin applications.

6.1.2 Oxygen detection using In_2O_3 thin films

In this study, an In_2O_3 thin film based oxygen sensor was designed and fabricated. We have investigated the influence of moisture as well as applied dc bias on the O_2 sensing characteristics of In_2O_3 thin films. The O_2 sensitivity was found to increase significantly in presence of moisture, which can be attributed to enhanced electron density in the In_2O_3 thin film, which is caused by electron donation by the chemisorbed water molecules. Higher dc bias was found to dramatically improve the sensitivity by more than two orders of magnitude. The bias related enhancement in sensitivity can be explained by the chemical gating effect of the O^{2-} ions, formed on the In_2O_3 surface through O_2 chemisorption, which under larger dc bias produces an exponentially higher change in the sensor current.

6.1.3 Graphene based ion sensitive field effect transistor

In the development of biocompatible ion sensor, we designed, fabricated and characterized a novel graphene based ion sensitive field effect transistor (ISFET) for real-time K^+ efflux measurement from living cells. I-V and C-V characteristics of the ISFET sensor have been extensively studied in both electrolyte and physiological buffer solutions. From the C-V measurement, we identified and calculated the interfacial capacitance at the graphene/solution interface, which consists of the electrical double layer capacitance (C_{EDL}) at the interface and the quantum capacitance of graphene (C_Q) Valinomycin coating of the graphene ISFETs has been utilized to enhance ionic detection sensitivity and impart selectivity. With the ionophore modified graphene ISFET, we have successfully demonstrated real-time detection of K^+ concentration change in both electrolyte and physiological buffer solutions. Utilizing a salt bridge configuration, we were able to perform real-time K^+ detection in μl volume of testing solution, which in term increases the sensing resolution for cell-based K^+ efflux measurement.

Moreover, we have conducted cell based real-time K^+ efflux measurement utilizing commercial Si based ISFETs and experimentally prove the concept of ISFET based ion channel screening assay for drug discovery. On the other hand, the prototype graphene based ISFET has also been evaluated for K^+ efflux detection using a salt bridge configuration, showing promising sensing results for future study.

In the fabrication of graphene ISFET, we found the epoxy glue used for the sensor encapsulation had significant effect on the electric transport properties of graphene including conductivity, carrier concentration and field effect mobility. N-type doping effect of the epoxy on graphene has been carefully identified and confirmed by systematic experiments, which is promising for new alternative approach to dope graphene.

6.2 Future outlook

6.2.1 PDMS based pressure sensor

In Chapter 2, we have proposed a simple physical model to explain the sensing mechanism of our PDMS based pressure sensor. The strain induced micro-crack formation in Au thin film resistor is mainly responsible for the high sensitivity achieved by the pressure sensor. Interestingly, the formation of strain induced micro-cracks in the Au thin film seems to be quite reversible within certain pressure range, i.e. the effective sensing range of the pressure sensor. However, the possible formation mechanism of these microcracks has not been understood clearly yet. Moreover, we initially chose 200 nm as the thickness of the Au thin film resistor, which is based on past studies [46-48, 51-53] where the Au thickness varied from 5 to 500 nm. In the future work, we would like to investigate the pressure sensor with varying design parameters including the thickness of Au thin film and PDMS membrane, the pattern of the thin film resistor and the dimensions of the active sensing area. We believe these design parameters largely determine the sensor performance (i.e. sensitivity, effective sensing range, response time, reproducibility etc.). The investigation will also help us to better understand the formalism of these microcracks.

6.2.2 Graphene based ISFET

From the C-V characterization of our graphene ISFET in electrolyte solution, we identified and calculated the interfacial capacitance at the graphene/solution interface, which consists of the electrical double layer capacitance (C_{EDL}) at the interface and the quantum capacitance of graphene (C_Q). In the future, we would like to further separate the two capacitive components and study C_{EDL} and C_Q with ionic concentration individually.

In the development of valinomycin modified graphene ISFET, we will conduct research to understand the sensing performance enhancement with valinomycin/polymer coating, in specific, the effect of membrane thickness and composition.

So far, we have successfully demonstrated direct cell culture on the prototype graphene ISFET devices, showing excellent biocompatibility of graphene. With the fundamental understanding acquired in the future investigation mentioned above, we would like to further optimize the ISFET sensor performance and eventually achieve on-chip real time K^+ efflux measurement from living cells.

6.2.3 Chemical doping of graphene using epoxy

In the investigation of the effect of sensor packaging on the electrical properties of graphene, we have experimentally confirmed that the epoxy used for the ISFET encapsulation has a strong n-type doping effect on graphene. In the future work, we will study the extent of doping possible and the stability of the doping using various characterization tools e.g. Raman spectroscopy, angular-resolved photoemission spectroscopy (ARPES), etc. .

REFERENCES

[1] Noh, S., Yoon, C., Hyun, E., Yoon, H.N., Chung, T.J., Park, K.S. *et al.*, “Ferroelectret film-based patch-type sensor for continuous blood pressure monitoring,” *Electronics Letter*, vol. **50**, pp. 143-144, 2014.

[2] Goutam Koley, Jie Liu, Md. W Nomani, Moonbin Yim, Xuejun Wen and T-Y Hsia, “Miniaturized implantable pressure and oxygen sensors based on polydimethylsiloxane thin films,” *Mater Sci Eng C.*, vol. **29**, pp. 685-690, 2009.

[3] Guangwei Liu, Luhong Mao, Liying Chen and Sheng Xie, Locatable-body temperature monitoring based on semi-active UHF RFID tags,” *Sensors*, vol. **14**, pp. 5952-5966, 2014.

[4] B. Schazmann, D. Morris, C. Slater, S. Beirne, C. Fay, R. Reuveny *et al.*, A wearable electrochemical sensor for the real-time measurement of sweet sodium concentration,” Analytical Methods, vol. **2** , pp. 342-348, 2010.

[5] Kenneth B. Walsh, Nicholas DeRoller, Yihao Zhu, Goutam Koley, “Application of ion-sensitive field effect transistors for ion channel screening,” *Biosensors and Bioelectronics*, vol. **54**, pp. 448-454, 2014.

[6] M. Rothmaier, M. P. Luong and F. Clemens, “Textile pressure sensor made of flexible plastic optical fibers,” *Sensors*, vol. **8**, pp. 4318-4329, 2008.

[7] A. B. Joshi, A. E. Kalange, D. Bodas and S. A. Gangal, “Simulations of piezoelectric pressure sensor for radial artery pulse measurement,” *Mater Sci Eng B.*, vol. **168**, pp. 250-253, 2010.

[8] D. J. Lipomi, M. Vosguertchian, B. C-K. Tee, S. L. Hellstrom, J. A. Lee, C. H. Fox *et al.*, “Skin-like pressure and strain sensors based on transparent elastic films of carbon nanotubes,” *Nature Nanotechnology*, vol. **6**, pp. 788-792, 2011.

[9] Leineweber M, Pelz G, Schmidit M, Kappert H and Zimmer G, “New tactile sensor chip with silicone rubber cover,” Sensors Actuators A, vol. **84**, pp. 236-245, 2000.

[10] Rainee N. Simons, David G. Hall and Félix A. Miranda, “RF telemetry system for an implantable bio-MEMS sensor,” *Proc. IEEE MTT-S Int. Microwave Symp. Digest*, vol **3**, pp. 1433-1436, 2004.

[11] Zhou M, Huang Q, Qin M and Zhou W, “A novel capacitive pressure sensor based on sandwich structures,” vol. **14**, pp. 1272-1282, 2005.

[12] Cheng M Y, Huang X H, Ma C W and Yang Y J, “A flexible capacitive tactile sensing array with floating electrodes,” *J. Micromech. Microeng.*, vol **19**, pp. 115001-115001-10, 2009.

[13] Stefan C. B. Mannsfeld, Benjamin C-K. Tee, Randall M. Stoltenberg, Christopher V. H-H. Chen, Soumendra Barman *et al.*, “Highly sensitive flexible pressure sensors with microstructured rubber dielectric layers,” *Nature Materials*, vol. **9**, pp. 859-864, 2010.

[14] M. Shimojo, A. Namiki, M. Ishikwa, R. Makino and K. Mabuchi, “A tactile sensor sheet using pressure conductive rubber with electrical-wires stitched method,” *IEEE Szensors J.*, vol. **4**, pp. 589-596, 2004.

[15] C. Metzger, E. Fleisch, J. Meyer, M. Dansachmüller, I. Graz, M. Kaltenbrunner *et al.*, “Flexible-foam-based capacitive sensor arrays for object detection at low cost,” *Appl. Phys. Lett.*, vol **92**, pp. 013506-013506-3, 2008.

[16] I. Graz, M. Kaltenbrunner, C. Keplinger, R. Schwödiauer, S. Bauer, S. P. Lacour *et al.*, “Flexible ferroelectret field-effect transistor for large-area sensor skins and microphones,”, *Appl. Phys. Lett.*, vol. **89**, pp. 073501, 2006.

[17] G. Darlinski, U. Böttger, R. Waser, H. Klauk, M. Halik, U. Zschieschang *et al.*, “Mechanical force sensors using organic thin-film transistors,” *J. Appl. Phys.*, vol **97**, pp. 093708-093708-4, 2005.

[18] Dong-Weon Lee and Young-Soo Choi, “A novel pressure sensor with a PDMS diaphragm,” *Microelectronic Engineering*, vol. **85**, pp. 1054-1058, 2008.

[19] H.C. Lim, B. Schulkin, M.J. Pulickal, S. Liu, R. Petrova, G. Thomas *et al.*, “Flexible membrane pressure sensor,” *Sensors and Actuators A*, vol. **119**, pp. 332-335, 2005

[20] Youngbin Lee, Sukang Bae, Houk Jang, Sukjae Jang, Shou-En Zhu, Sung Hyun Sim *et al.*, “Wafer-scale synthesis and transfer of graphene films”, *Nano Lett.*, vol. **10**, pp. 490-493, 2010.

[21] Parker R L and Krinsky A, “Electrical resistance-strain characteristics of thin evaporated metal films”, *J. Appl. Phys.*, vol. **34**, pp. 2700-2708, 1963.

[22] Yan Wang, Li Wang, Tingting Yang, Xiao Li, Xiaobei Zang, Miao Zhu *et al.*, “Wearable and highly sensitive graphene strain sensors for human motion monitoring,” *Advanced Functional Material*, vol. **24**, pp, 4666-4670, 2014.

[23] Po-jui Chen, Damien C. Rodger, Saloomeh Saati, Mark S. Humayun and Yu-chong Tai, "Microfabricated implantable parylene-based wireless passive intraocular pressure sensors," *Journal of Microelectromechanical Systems*, vol. **17**, pp. 1342-1351, 2008.

[24] Yongli Mi, Yannie Chan, Dieter Trau, Pingbo Huang and Erqiang Chen, "Micromolding of PDMS scaffolds and microwells for tissue culture and cell patterning: A new method of microfabrication by the self-assembled micropatterns of diblock copolymer micelles," *Polymer*, vol **47**, pp. 5214-5130, 2006.

[25] Bo Huang, Hongkai Wu, Samuel Kim, Brian K. Kobilka and Richard N. Zare, "Phospholipid biotinylation of polydimethylsiloxane (PDMS) for protein immobilization," *Lab on a Chip*, vol. **6**, pp. 369-373, 2006.

[26] Xinchuan Liu and Cheng Luo, "Fabrication of super-hydrophobic channels," *J. Micromech. Microeng.*, vol. **20**, pp. 025029-025030, 2010.

[27] Xinchuan Liu and Cheng Luo, "Fabrication of Au sidewall micropatterns using Si-reinforced PDMS molds", *Sensors and Actuators A*, vol. **152**, pp. 96-103, 2009.

[28] Sepulveda A T, Pontes A J, Viana J C, Guzman de Villoria R, Fachin F, Wardle B L *et al.*, "Flexible sensor for blood pressure measurement," *Proc. 33rd Ann. Int. Conf. IEEE/EMBS (Boston, MA)*, pp. 512-515, 2011.

[29] Takao Someya, Tsuyoshi Sekitani, Shingo Iba, Yusaku Kato, Hiroshi Kawaguchi, and Takayasu Sakurai, "A large-area, flexible pressure sensor matrix with organic field-effect transistors for artificial skin application," *Proc. Natl Acad. Sci.*, vol. **101**, pp. 9966-9970, 2004.

[30] Changhyun Pang, Gil-Yong Lee, Tae-il Kim, Sang Moon Kim, Hong Nam Kim, Sung-Hoon Ahn, "A flexible and highly sensitive strain-gauge sensor using reversible interlocking of nanofibres," *Nature Materials*, vol. **11**, pp. 795-801, 2012.

[31] Kin Fong Lei, Kun-Fei Lee and Ming-Yih Lee, "Development of a flexible PDMS capacitive pressure sensor for plantar pressure measurement," *Microelectronic Engineering*, vol. **99**, pp. 1-5, 2012.

[32] Le Cai, Li Song, Pingshan Luan, Qiang Zhang, Nan Zhang et al. "Super-stretchable, transparent carbon nanotube-based capacitive strain sensors for human motion detection," vol. **3**, article number. 3048, 2013.

[33] Jongchan Kim, Hoyoung Lee, Soondo Cha and Bumkyoo Choi, "Fabrication and evaluation of implantable pressure sensor using strain gauge," *In Biomedical*

Engineering International Conference (BMEiCON) 2012, Ubon Ratchathani Thailand, 2012.

[34] J. Lohmiller, N.C. Woo and R. Spolenak, “Microstructure-property relationship in highly ductile Au-Cu thin films for flexible electronics”, *Materials Science and Engineering A*, vol. **527**, pp. 7731-7740, 2010.

[35] R. L. Parker and A. Krinsky, “Electrical resistance-strain characteristics of thin evaporated metal films,” *Journal of Applied Physics*, vol. **34**, pp. 2700-2708, 1963.

[36] Moony M, “A theory of large elastic deformation”, *J. Appl. Phys.*, vol **11**, pp. 582-597, 1940.

[37] Rivlin R S, “Large elastic deformations of isotropic materials VI: further results in the theory of torsion, shear and flexure,” *Phil. Trans. R. Soc. Lond. A*, vol **242** pp. 173-195, 1949.

[38] I D Johnston, D K McCluskey, C K L Tan and M C Tracey, “Mechanical characterization of bulk Sylgard 184 for microfluidics and microengineering,” *J. Micromech. Microeng.*, vol. **24**, pp. 035017-035017-7, 2014.

[39] Zhixin Wang, Alex A. Volinsky and Nathan D. Gallant, “Crosslinking effect on polydimethylsiloxane elastic modulus measured by custom-built compression instrument,” *Journal of Applied Polymer Science*, vol. **131**, pp. 41050-41050-4, 2014.

[40] Xinchuan Liu, Yihao Zhu, Khan Nomani, Xuejun Wen, Tain-Yen Hsia and Goutam Koley, “Highly sensitive pressure sensor using Au patterned polydimethylsiloxane membrane for biosensing applications,” *J. Micromech. Microeng.*, vol. **23**, pp. 025022-025022-10, 2013.

[41] H.K. Lee, S.I. Chang and E. Yoon, “A flexible polymer tactile sensor: Fabrication and modular expandability for large area deployment, *J. Microelectromech. Syst.*, vol **15**, pp. 1681-1686, 2006.

[42] I. Graz, M. Krause, S.B. Gogonea, S. Bauer, S.P. Lacour and B. Ploss *et al.*, “Flexible active-matrix cells with selectively poled bifunctional polymerceramic nanocomposite for pressure and temperature sensing skin,” *J. Appl. Phys.*, vol **106**, pp. 034503, 2009.

[43] A.V. Shirinov and W.K. Schomburg, “Pressure sensor from a PVDF film,” *Sens. Actuat. A*, vol **142**, pp. 48-55, 2008.

[44] Wen Y H, Yang G Y, Bailey V J, Lin G, Tang W C and Keyak J H, “Mechanically robust micro-fabricated strain gauges for use on bones,” *Proc. 3rd*

Annu. Int. IEEE/EMBS Special Topic Conf. on Micro technologies in Medicine and Biology (Kahuku, HI), pp. 302-304, 2005.

[45] Yang G Y, Bailey V J, Wen Y H, Lin G, Tang W C and Keyak J , "Fabrication and characterization of microscale sensors for bone surface strain measurement", *Proc. IEEE Sensors*, vol. **3**, pp. 1355-1358, 2004.

[46] Lacour S P, Wagner S, Huang Z and Suo Z, "Stretchable gold conductors on elastomeric substrates," *Appl. Phys. Lett.*, vol. **82**, pp. 2404-2406, 2003.

[47] Lacour S P, Chan D, Wagner S, Li T and Suo Z, "Mechanisms of reversible strechability of thin metal films on elastomeric substrates," *Appl. Phys. Lett.*, vol. **88**, pp. 204103-204103-3, 2006.

[48] Wagner S, Lacour S P, Jones J, Hsu P I, Sturm J C, Li T and Suo Z, "Electronic skin: architecture and components,", *Physica E*, vol. **25**, pp. 326-334, 2004.

[49] Cairns D R, Witte II R P, Sparacin D K, Sachsman S M, Paine D C, Crawford G P and Newton R R, "Strain-Dependent Electrical Resistance of Tin-Doped Indium Oxide on Polymer Substrates," *Appl. Phys. Lett.*, vol.**76**, pp. 1425-1427, 2000.

[50] Chung D D L, "Strain sensor based on the electrical resistance change accompanying the reversible pull-out of conducting short fibers in a less conducting matrix," *Smart Mater. Strum.*, vol. **4**, pp. 59-61, 1995.

[51] Akogwu O, Kwabi D, Munhutu A, Tong T and Soboyejo W O, "Adhesion and cyclic stretching of Au thin film on poly(dimethyl-siloxane) for stretchable electronics," *J. Appl. Phys.*, vol. **108**, pp.123509-123509-6, 2010.

[52] Akogwu O, Kwabi D, Midturi S, Eleruja M, Babatope B and Soboyejo W O, "Large strain deformation and cracking of nano-scale gold films on PDMS substrate," *Mater. Sci. Eng. B*, vol. **170**, pp. 32-40, 2010.

[53] Lacour S P, Huang Z, Suo Z and Wagner S, "Deformable interconnects for conformal integrated circuits," *Proc. Mat. Res. Soc. Symp.*, vol. **736**, D4.8.1-4.8.6, 2003.

[54] Maunza I. Sulis A and Bonfiglio A, "Pressure sensing by flexible, organic, field effect transitors," *Appl. Phys. Lett.*, vol. **89**, pp. 143502-143502-3, 2006.

[55] Potkay J A, "Long term, implantable blood pressure monitoring systems," *Biomed. Microdevices*, vol. **10**, pp. 379-392, 2008.

[56] Yulong Xu, Xiaohua Zhou and O. Toft Sorensen, "Oxygen sensors based on semiconducting metal oxides: an overview," *Sens. Actuators B*, vol. **65**, pp. 2-4, 2000.

[57] Takashi Takeuchi, “Oxygen sensors,” *Sens. Actuators*, vol. **14**, pp. 109-124, 1988.

[58] A. D. Brailsford, M. Yussouff, E. M. Logothetis, T. Wang and R. E. Soltis, “Experimental and theoretical study of the response of ZrO_2 oxygen sensors to simple one-reducing-gas mixtures,” *Sens. Actuators B,* vol. **42**, pp. 15-26, 1997.

[59] Koley G, Liu J, Nomani MW, Yim M, Wen X and Hsia TY, “Miniaturized implantable pressure and oxygen sensors based on polydimethylsiloxane thin films”, *Mater Sci Eng R Rep.*, vol. **29**, pp. 685-690, 2010.

[60] Shigehito Iguchi, Kohji Mitsubayashi, Takayuki Uehara and Misuhiro Ogawa, “A wearable oxygen sensor for transcutaneous blood gas monitoring at the conjunctiva,” *Sens. Actuators B*, vol. **108**, pp. 733-737, 2005.

[61] Reichet S., Fiala J., Werber A., Forster K., Heilmann C. and Klemm R., “Development of an Implantable Pulse Oximeter,” *IEEE Transactions on Biomedical Engineering*, vol. **55**, pp. 581-588, 2008.

[62] Vasile E. Turcu, Scott B. Jones and Dani Or, “Continuous soil carbon dioxide and oxygen measurements and estimation of gradient-based gaseous flux,” *Vadose Zone Journal*, vol. **4**, pp. 1161-1169, 2005.

[63] M. J. Atkinson, F. I. M. Thomas, N. Larson, E. Terrill, K. Morita and C. C. Liu, “A micro-hole potentiostatic oxygen sensor for oceanic CTDs,” *Deep Sea Research* vol. **42**, pp. 761-771, 1995.

[64] Md. W.K. Nomani, D. Kersey, J. James, D. Diwan, T. Vogt, Richard A. Webb *et al.*, “Highly sensitive and multidimensional detection of NO_2 using In_2O_3 thin films,” *Sens. Actuators B*, vol. **160**, pp. 251-259, 2001.

[65] Nima Mohseni Kiasari and Peyman Servati, “Dielectrophoresis-assembled ZnO nanowire oxygen sensors,” *IEEE Electron Device Letters*, vol. **32**, pp. 982-984, 2011.

[66] K.D. Schierbaum, U.K. Kirner, J.F Geiger, W. Göpel, “Schottky-barrier and conductivity gas sensors based upon Pd/SnO_2 and Pt/TiO_2,” *Sens. Actuators B*, vol. **4**, pp. 87-94, 1991.

[67] Muhammad Qazi, Goutam Koley, Sangmoon Park and Thomas Vogt, “NO_2 detection by adsorption induced work function changes in In_2O_3 thin films,” *Appl. Phys. Lett.,* vol. **91**, pp. 043113-043113-3, 2007.

[68] V. Brinzari, G. Korotchenkov and S. Dmitriev, “Simulation of thin film gas sensors kinetics,” *Sens. Actuators B*, vol. **61**, pp. 143-53, 1999.

[69] G. Korotcenkov, V. Brinzari and S. Dmitriev, “Kinetic characteristics of SnO_2 thin-film gas sensors for environmental monitoring,” *Proceedings of SPIE*, vol. **3539**, pp. 196, 1998.

[70] J. Xu, Y. Shun, Q. Pan and J. Qin, “Sensing characteristics of double layer film of ZnO,” *Sens. Actuators B*, vol. **66**, pp. 161-163, 2000.

[71] J.R. Bellingham, A.P. Mackenzie and W.A. Philips, “Precise measurements of oxygen content: Oxygen vacancies in transparent conducting indium oxide films,” *Appl. Phys. Lett.*, vol. **58**, pp. 2506-2508, 1991.

[72] S.J. Ippolito, N. Kandasamy, K. Kalantar-zadeh, W. Woldar-ski, K. Galatsis, G. Kiriakidis *et al.*, “Highly sensitive layered ZnO/$LiNbO_3$ SAW device with InO_x selective layer for NO_2 and H_2 gas sensing,” *Sens. Actuators B*, vol. **111**, pp. 207-212, 2005.

[73] Daniel Laser, “Conductivity modulation in indium oxide films by oxygen pressure variations,” *J. Appl. Phys.*, vol. **52**, pp. 5179-5181, 1981.

[74] A. Gurlo, M. Ivanovskaya, N. Bârsan, M. Schweizer-Berberich, U. Weimar, W. Gőpel *et al.*, “Grain size control in nanocrystalline In_2O_3 semiconductor gas sensors,” *Sens. Actuators B*, vol. **44**, pp. 327-333, 1997.

[75] F. Chaabouni, M. Abaab, B. Rezig, “Metrological characteristics of ZnO oxygen sensor at room temperature,” *Sens. Actuators B.*, vol. **100**, pp. 200-204, 2004.

[76] Giovanni Neri, Anna Bonavita, Giuseppe Micali, Giuseppe Rizzo, Signorino Galvagno, Markus Niederberger *et al.*, “A highly sensitive oxygen sensor operating at room temperature based on platinum-doped In_2O_3 nanocrystals,” *Chem. Commun.*, vol. **48**, pp. 6032-6034, 2005.

[77] John Atkinson, Andy Cranny and Cinzia Simonis de Cloke, “A low-cost oxygen sensor fabricated as a screen-printed semiconductor device suitable for unheated operation at ambient temperatures,” *Sensors and Actuators B*, vol. **47**, pp. 171-180, 1998.

[78] M. Abaab, A. S. Bouazzi and B. Rezig, “Competitive $CuAlS_2$ oxygen gas sensor,” *Microelectron. Eng.*, vol. **51**, pp. 343-348, 2000.

[79] K. Kishiro, S. Takemoto, H. Kuriyaki and K. Hirakawa, “Resistivity response to oxygen of transition metal dichalcogenide TiS_2,” *J. Appl. Phys.*, vol. **33**, pp. 1069-1073, 1994.

[80] K. Kishiro, H. Kuriyaki and K. Hirakawa, “Grain size effect of $CuFeTe_2$ response to oxygen,” *Jpn. J. Appl. Phys.*, vol. **32**, L674-675, 1993.

[81] Stuart A. Hoenig and John R. Lane, “Chemisorption of oxygen on zinc oxide, effect of a dc electric field,” *Surf. Sci.* vol. **11**, pp.163-174, 1986.

[82] Y. Zhang, A. Kolmakov, S. Chretien, H. Metiu and M. Moskovits, “Control of catalytic reactions at the surface of a metal oxide nanowire by manipulating electron density inside it,” *Nano Lett.*, vol. **4**, pp. 403-07, 2004.

[83] Zhiyong Fan, Dawei Wang, Pai-Chun Chang, Wei-Yu Tseng, and Jia G. Lu, “ZnO nanowire field-effect transistor and oxygen sensing property,” *Appl. Phys. Lett.*, vol. **85**, pp. 5923-5925, 2004.

[84] Yoshiaki Sato, Kazuyuki Takai, and Toshiaki Enoki, “Electrically controlled adsorption of oxygen in bilayer graphene devices,” *Nano Lett.* vol. **11**, pp. 3468-3475, 2011.

[85] F. Volkenshtein, “The electronic theory of catalysis on semiconductors” (Macmillan and Co., New York, 1963), Cited on p. 126.

[86] Xiangwei Liu, Rui Wang, Tong Zhang, Yuan He, Jinchun Tu and Xiaotian Li, “Synthesis and characterization of mesoporous indium oxide for humidity-sensing applications,” *Sens. Actuators B*, vol. **150**, pp. 442-448, 2010.

[87] Radhouane Bel Hadj Tahar, Takayuki Ban, Yutaka Ohya, and Yasutaka Takahashi, “Humidity-sensing characteristics of divalent-metal-doped indium oxide thin films,” *J. Am. Ceram. Soc.* vol. **81**, pp. 321-327, 1998.

[88] Nicolae Barsan and Udo Weimar, “Conduction model of metal oxide gas sensors,” *Journal of Electroceramics*, vol. **7**, pp. 143-167, 2001.

[89] G. Neri, A. Bonavita, G. Micali, G. Rizzo, N. Pinna and M. Niederberger, “In_2O_3 and Pt-In_2O_3 nanopowders for low temperature oxygen sensors,” *Sens. Actuators B*, vol. **127**, pp. 455-462, 2007.

[90] W.Göpel and K.D. Schierbaum, “SnO_2 sensors: current status and future prospects,” *Sens. Actuators B*, vol. **26/27**, pp.1-12, 1995.

[91] Enrico Traversa, “Ceramic sensors for humidity detection: the state-of-the-art and future developments,” *Sens. and Actuators B*, vol. **23**, pp. 135-156, 1995.

[92] Wan-Fang Chung, Ting-Chang Chang, Hung-Wei Li, Shih Ching Chen, Yu-Chun Chen, Tseung-Yuen Tseng *et al.*, “H_2O-assisted O_2 adsorption in sol-gel derived amorphous indium gallium zinc oxide thin film transistors,” *Electrochemical and Solid-State Letters*, vol. **14**, pp. 235-237, 2011.

[93] K.H. Zhang, Y.C. Zhao, K. Deng, Z. Liu, L. F. Sun, Z. X. Zhang *et al.*, "Effectively enhanced oxygen sensitivity of individual ZnO tetrapod sensor by water preadsorption," *Appl. Phys. Lett.*, vol. **92**, pp. 213116-213116-3, 2008.

[94] T Seiyama, N Yamazoe and H Arai, "Ceramic humidity sensors," *Sens. Actuators*, vol. **4**, pp. 85-96, 1983.

[95] B. M. Kulwicki, "Ceramic sensors and transducers," *J. Phys. Chem. Solids.*, vol. **45**, pp.1015-1031, 1984.

[96] M. Neuburger, I. Daumiller, T. Zimmermann, M. Kunze, G. Koley, M.G. Spencer *et al*, "Surface stability of InGaN-channel based HFETs," *Electronics Letters*, vol. **39**, pp. 1614-1615, 2003.

[97] Ho-Young Cha, C. I. Thomas, G.Koley, Lester. F. Eastman, and M. G. Spencer, "Reduced trapping effects and improved electrical performance in buried-gate 4H-SiC MESFETs," IEEE Transactions on Electron Devices, vol. **50**, pp. 1569-1574, 2003.

[98] John Dunlop, "Turning up the pace of ion channel screening in drug discovery," *Neropsychopharmacollogy Reviews*, vol. **34**, p. 253, 2009.

[99] Jeffrey J Clare, "Targeting ion channels for drug discovery," *Discov Med.*, vol. **9**, pp. 253-260, 2010.

[100] Cecilia Jienez, Andrey Bratov, Natalia Abramova and Antoni Baldi, "ISFET based sensors: Fundamentals and Applications," Encyclopedia of Sensors, vol. **5**, pp. 151-196, 2006.

[101] P. Bergveld, "Development of an ion-sensitive solid-state device for Neurophysiological measurements," *IEEE Transaction on Biomedical Engineering*, vol. **BME-17**, pp. 70-71, 1970.

[102] P. Bergveld, "Development, operation, and application of the ion-sensitive field effect transistor as a tool for electrophysiology," *IEEE Transactions on Biomedical Engineering*, vol. **BME-19**, pp. 342-351, 1972.

[103] W.H. Baumann, M. Lehmann, A. Schwinde, R. Ehret, M. Brischwein and B. Wolf, "Microelectronic sensor system for microphysiological application on living cells," *Sensors and Actuators B,* vol. **55**, pp. 77-89, 1999.

[104] Wen H. Ko, Jacques Mugica and Alain Ripart, *Implantable sensors for closed-loop prosthetic systems* pp. 89-114: Futura Publishing Company, 1985.

[105] Steve D. Cara, Danuta Petelenz and Jiří Janata, “pH-based enzyme potentiometric sensors. Part 2. Glucose-sensitive field effect transistor,” *Analytical Chemistry*, vol. **57**, pp. 1920-1923, 1985.

[106] P. Arquint, M. Koudelka-Hep, B.H. Van der Schoot, P. Van der Wal and N.F. de Rooij, “Micromachined analyzers on a silicon chip,” *Clin. Chem.*, vol. **40**, pp. 1805-1809, 1994.

[107] C. Colapicchioni, A. Barbaro, F. Porcelli and I. Giannini, “Immunoenzymatic assay using CHEMFET devices,” *Sensors and Actuators B*, vol. **4**, pp. 245-250, 1991.

[108] Nikos Chaniotakis and Nikoletta Sofikiti, “Novel semiconductor materials for the development of chemical sensors and biosensors: A review,” *Anayltica Chimica Acta*, vol. **615**, pp. 1-9, 2008.

[109] A. Bratov, N. Abramova and A. Ipatov, “Recent trends in potentiometric sensor arrays: A review,” *Anayltica Chimica Acta*, vol. **678**, pp. 149-159, 2010.

[110] L Bousse, N. F. de Rooij, and P. Bergveld, “The influence of counter-ion adsorption on the ψ_0/pH characteristics of insulator surfaces,” *Surface Sci.*, vol. **135**, pp. 479-496, 1983.

[111] M. Esashi and T. Matsuo, “Integrated micro multi ion sensor using field effect of semiconductor,” *IEEE Trans Biomed Eng.*, vol. **BME-25**, pp. 184-191, 1978.

[112] S. D. Moss, J. Janata and C. C. Johnson, “Potassium ion-sensitive field effect transistor,” Analytical Chemistry, vol. 47, pp. 2238-2243, 1975.

[113] A. Bratov, N. Abramova, J. Munoz, C. Domínguez, S Alegret and J Bartrolí, “Ion sensor with photocurable polyurethane polymer membrane,” J. Electrochem. Soc., vol. 141, L111-112, 1994.

[114] Feng Yan, Pedro Estrela, Yang Mo, Piero Migliorato and Hiroshi Maeda, “Polycrystalline silicon ISFETs on glass substrate,” *Sensors*, vol. **5**, pp. 293-301, 2005.

[115] A.K. Geim and K. S. Novoselov, “The rise of graphene,” *Nature Materials*, vol. **6**, pp. 183-191, 2007.

[116] K. S. Novoselov, A. K. Geim, S. V. Morozov, D. Jiang, Y. Zhang, S. V. Dubonos et al., “Electric field effect in atomically thin carbon films,” *Science*, vol. **306**, pp. 666-669, 2004.

[117] Christoph Sprossler, Morgan Denyer, Steve Britland, Wolfgang Knoll and Andreas Offenhausser, “Electrical recordings from rat cardiac muscle cells using field effect transistors,” *Physical Review E*, vol. **60**, pp. 2171-2176, 1999.

[118] C. Schmidt, “Bioelectronics: The bionic material,” *Nature*, vol. **483**, p. S43, 2012.

[119] Lucas H. Hess, Michael Jansen, Vanessa Maybeck, Moritz V. Hauf, Max Seifert and Martin Stutzmann *et al.*, “Graphene transistors arrays for recording action potentials from electrogenic cells,” *Advanced Materials*, vol. **23**, pp. 5045-5049, 2011.

[120] Jianting Ye, Monica F. Craciun, Mikito Koshino, Saverio Russo, Seiji Inoue, Hongtao Yuan *et al.*, “Accessing the transport properties of graphene and its multilayers at high carrier density”, *PNAS.*, vol. **108**, pp. 13002-13006, 2010.

[121] Eri Uesugi, Hidenori Goto, Ritsuko Eguchi, Akihiko Fujiwara and Yoshihiro Kubozono *et al.*, “Electric double-layer capacitance between and ionic liquid and few-layer graphene,” *Nature Scientific Report*, vol. **3**, pp. 1595-1595-5, 2013.

[122] A.K. Singh, M. A. Uddin, J. T. Tolson, H. Maire-Afeli, N. Sbrockey, G. S. Tompa et al., “Electrically tenable molecular doping of graphene,” *Appl. Phys. Lett.*, vol. **102**, pp. 043101-043101-5, 2013.

[123] http://www.epotek.com/site/files/brochures/pdfs/medical_brochure.pdf

[124] A.K.M. Newaz, Yevgeniy S. Puzyrev, Bin Wang, Sokrates T. Pantelides and Kirill I. Bolotin, Probing charge scattering mechanisms in suspended graphene by varying its dielectric environment,” *Nature Communication*, vol. 3, 2011.

[125] Si Chen, Zhi-Bin Zhang, Laipeng Ma, Patrik Ahlberg, Xindong Gao and Zhijun Qiu, “A graphene field-effect capacitor sensor in electrolyte,” *Appl. Phys. Lett.*, vol. **101**, pp. 154106-154106-5, 2012.

[126] Xiaochen Dong, Yumeng Shi, Wei Huang, Peng Chen and Lain-Jong Li, “Electrical detection of DNA hybridization with single-base specificity using transistors based on CVD-grown graphene sheets,” *Advance Materials*, vol. **12**, pp. 1-5, 2012.

[127] Yasuhide Ohno, Kenzo Maehashi, Yusuke Yamashiro and Kazuhiko Matsumoto, “Electrolyte-gated graphene field –effect transistors for detecting pH and protein adsorption,” *Nano Letter*, vol. **9**, pp. 3318-3322, 2009.

[128] Xiaochen Dong, Dongliang Fu, Wenjing Fang, Yumeng Shi, Peng Chen and Lain-Jong Li, “Doping single-layer graphene with aromatic molecules,” *Small*, vol. **5**, pp. 1422-1426, 2009.

[129] Xiaomu Wang, Jian-Bin Xu, Weiguang Xie and Jun Du, “Quantitative analysis of graphene doping by organic molecular charge transfer,” *Journal of Physical Chemistry C*, vol. **115**, pp. 7596-7602, 2011.

[130] http://oldwww.epotek.com/SSCDocs/MSDS/301_msds.PDF

[131] Justin C. Koepke, Joshua D. Wood, David Estrada, Zhun-Yong Ong, Kevin T. He, Eric Pop et al., “ Atomic-scale evidence for potential barriers and strong carrier scattering at graphene grain boundaries: a scanning tunneling microscopy study,” *ACS Nano*, vol. **7**, pp. 75-86, 2013.

[132] P.A. Hammond and D.R.S. Cumming, “Encapsulation of a liquid-sensing microchip using SU-8 photoresist,” *Microelectronic Engineering*, vol. **73-74**, pp. 893-897, 2004.

[133] Ewan H Conradie and David F Moore, “SU-8 thick photoresist processing as a functional material for MEMS applications,” *J. Micromech. Microeng.*, vol. **12**, pp. 368-374, 2002.

[134] Priscilla Kailian Ang, Wei Chen, Andrew Thye Shen Wee, and Kian Ping Loh, “Solution-gated epitaxial graphene as pH sensor,” JACS., vol. **130**, pp. 14392-14393, 2008.

[135] L.H Hess, M. V. Hauf, M. Seifert, F. Speck, T. Seyller, M. Stutzmann *et al.*, “High-transconductance graphene solution-gated field effect transistors,” *Applied Physics Letters*, vol. **99**, 033503-033503-3, 2011.

[136] Ehud Eyal and G.A. Rechnitz, “Mechanistic studies on the valinomycin-based potassium electrode,” vol. **43**, pp. 1090-1093, 1971.

[137] Mary Callaghan Rose and Robert W. Henkens, “Stability of sodium and potassium complexes of valinomycin,” *Biochimica et Biophysica Acta*, vol. **372**, pp. 426-435, 1974.

[138] Chang KS, Sun CJ, Chiang PL, Chou AC, Lin MC, Liang C *et al.*, “Monitoring extracellular K^+ flux with a valinomycin-coated silicon nanowire field-effect transistor,”, *Biosens. Bioelectron.*, vol. **31**, pp. 137-143, 2012.

[139] Cristina C. Cid, Jordi Riu, Alicia Maroto and F. Xavier Rius, “Ion-sensitive field effect transistors using carbon nanotubes as the transducing layer,” *Analyst*, vol. **133**, pp. 1001-1004, 2008.

[140] Lee Yook Heng and Elizbeth A.H. Hall, “Methacrylic–acrylic polymers in ion-selective membranes: achieving the right polymer recipe,” Analytica Chimica Acta, vol. **403**, pp. 77-89, 2000.

[141] Chun-Ze Lai, Marti M. Joyer, Melissa A. Fierke, Nicholas D. Petkovich, Andreas Stein and Philippe Buhlmann, “Subnanomolar detection limit application of ion-selective electrodes with three-dimensionally ordered macroporous (3DOM) carbon solid contacts,” *J. Solid State Electrochem.*, vol. **12**, pp. 123-128, 2009.

[142] A.D. Smith, S. Vaziri, S. Rodriguez, M. Östling and M.C. Lemme, “Wafer scale graphene transfer for back end of the line device integration,” *In Ultimate Integration on Silicon (ULIS), 15th International Conference*, Stockholm, Sweden, 2014.

[143] Xuesong Li, Yanwu Zhu, Weiwei Cai, Mark Borysiak, Boyang Han, David Chen *et al.*, “Transfer of large-area graphene films for high-performance transparent conductive electrodes,” *Nano Letters*, vol. **9**, pp. 4359-4363, 2009.

APPENDIX A

LIST OF PHYSIOLOGICAL BUFFER SOLUTIONS

Table A.1: Composition of normal saline solution
(pH 7.4 with 280 mOsm NaOH)

Organic/inorganic reagent	Concentration (mM/L)
NaCl	140
KCl	5
$CaCl_2$	1
$MgCl_2$	1
Dextrose	5
HEPES	5

Table A.2: Composition of NMG (N-methyl glucamine) solution
(pH 7.4)

Organic/inorganic reagent	Concentration (mM/L)
N-methyl glucamine	140
Aspartic acid	140
$CaCl_2$	1

APPENDIX B

GRAPHENE BASED ION SENSITIVE FIELD EFFECT TRANSISTOR FABRICATION: COMPLETE PROCESS FLOW

Two types of graphene based ISFET sensors were fabricated using two different encapsulation materials, biocompatible epoxy (EPO-TEK 301, Epoxy Technology, Inc.) and positive photoresist (S1811, Shipley company). The fabrication process consists of three major steps: (i) graphene wet transfer; (ii) fabrication of graphene based ISFET (iii) ISFET sensor packaging. Here below list the details of each step.

i. Graphene wet transfer

CVD derived graphene on copper foil was transferred to a 300 nm SiO_2/Si wafer chip via Cu wet etching method. [122, 142, 143] The details of the wet transfer process is discussed in Section 4.2.2 B, Chapter 4.

ii. Fabrication of graphene based ISFET

The graphene based ISFET consists of three terminals of drain, source and gate, respectively. Conventional Ag/AgCl reference electrode (BASi, Inc.) was used to as the gate electrode to control the potential of the testing solution (DI water/physiological buffer solutions). Drain and source metal electrodes (50 nm Cr/70 nm Au) were defined by the standard photolithography process as listed in Table B.1.

Table B.1: Photolithography process for ISFET fabrication and encapsulation

Lithography	Substrate: 300 nm SiO_2/Si wafer chip with graphene film transferred on Photoresist: Microposit S1811 Spin coating: 4000 rpm for 30 secs (thickness: ~ 1 μm) Softbake: 110 ˚C for 1 mins on hotplate Exposure: $\lambda = 436$ nm, UV density = 150 mJ/cm^2 Develop: MF 351 for 20 secs Hard Bake: 110 ˚C for 1 min on hotplate
Metal deposition	Equipment: Denton DV-502 E-beam metal evaporator Deposition of following metal stack at pressure below 2×10^{-6} torr Chromium (Cr): 50 nm Gold (Au): 70 nm
Metal liftoff	Metal liftoff in warm acetone with stirring, and dipped acetone spray by syringe

iii. Sensor packaging

For operation in electrolyte solution, fabricated graphene ISFETs were encapsulated by two different types of encapsulation materials, the epoxy glue (EPO-TEK 301) and photoresist (PR) S1811. In the epoxy encapsulation process, the wafer chip with the graphene ISFET fabricated on was first mounted on a homemade PCB board and wire-bonded. Epoxy glue was prepared by mixing the epoxy base (EPO-TEK 301-A) with its curing agent (301-B) under the weight ratio of 4:1. After properly mixing the epoxy/curing agent mixture, under 60 °C in air, we encapsulated the ISFET sensor by sequentially applying the mixture to cover the drain/source electrodes, four edges of the graphene film, Al bonding wires and the rest area of the wafer chip. After the epoxy was completely cured within ~ 2 hours, an opening window (i.e. the active sensing area of the

ISFET) was defined in the graphene film. Inset of Fig. 4.7 shows a representative graphene ISFET encapsulated using the epoxy. Last, the epoxy coated ISFET sensor was brought back to room temperature and stored in a vacuum sample box for future study.

The fabrication process of PR encapsulated graphene ISFET is illustrated in Figure B.1. Adopting the same procedures discussed in sections i and ii above, CVD graphene was transferred on a 300 nm SiO_2/Si wafer chip (Step 1) and then drain/source metal contacts deposited (Step 2). Afterwards, a layer of PR S1811 (~ 1 μm in thickness) was spin-coated on the entire wafer chip covering both the graphene film and metal electrodes (Step 3). In Step 4, a 2^{nd} round photolithography was performed, opening a window on top of the graphene film in between the electrodes and exposing the metal contact pads for wire bonding. The PR encapsulated ISFET chip was then mounted on a PCB board and wire-bonded (Step 5). The epoxy glue was used to encapsulate the Al bonding wires and the peripheral edges of the wafer chip. The optical image at the end of the process flow shows a representative graphene ISFET sensor encapsulated using the photoresist.

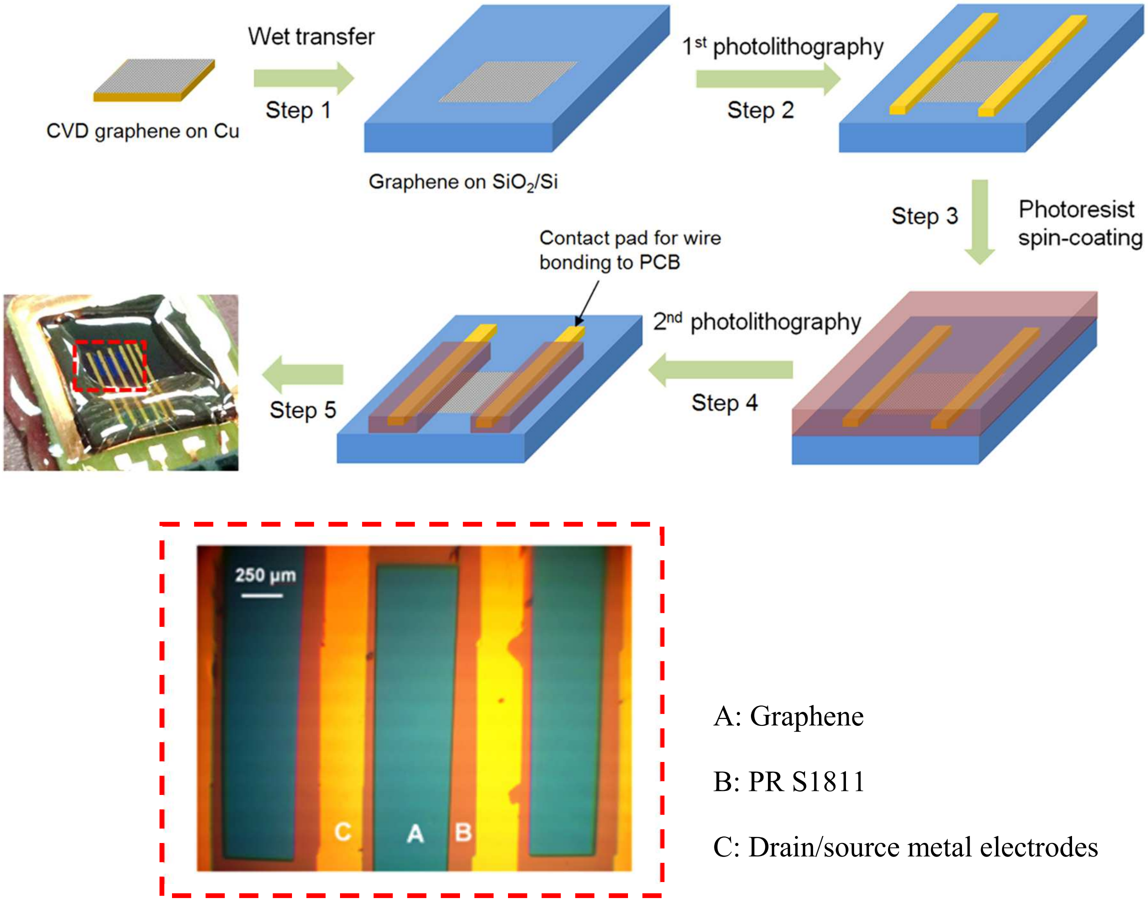

Figure B.1: Fabrication process flow chart of the PR encapsulated graphene ISFET. After 2nd photolithography (Step 4), the wafer chip is covered with a layer of PR S1811. Only the center area of the graphene thin film (the active sensing area of the ISFET) and the metal contact pads are exposed. For illustration simplicity, here only the photoresist encapsulating the metal electrodes are shown in the figure. Inset of the figure shows the optical image of an array of three ISFETs fabricated on a single graphene film.